Study of beauty hadrons using heavy flavour decay electrons with ALICE detectors at LHC

By

VIVEK KUMAR RAJESHWAR SINGH

Enrolment No.: PHYS04201704004

Variable Energy Cyclotron Centre, Kolkata

A thesis submitted to

The Board of Studies in Physical Sciences

In partial fulfillment of requirements

For the Degree of

DOCTOR OF PHILOSOPHY

of

HOMI BHABHA NATIONAL INSTITUTE

April, 2024

Homi Bhabha National Institute[1]

Recommendations of the Viva Voce Committee

As members of the Viva Voce Committee, we certify that we have read the dissertation prepared by **Vivek Kumar Singh** entitled "**Study of beauty hadrons using heavy flavour decay electrons with ALICE detectors at LHC**" and recommend that it may be accepted as fulfilling the thesis requirement for the award of Degree of Doctor of Philosophy.

Chairman	Dr. Subhasis Chattopadhyay		Date: 26/7/2024
Guide/Convener	Dr. Zubayer Ahammed		Date: 26/7/2024
Examiner	Prof. Vipin Bhatnagar		Date: 26/7/2024
Member 1	Dr. Partha Pratim Bhaduri	Partha Pratim Bhaduri	Date: 26/7/24
Member 2	Dr. Sourav Sarkar		Date: 26/7/2024
Member 3	Prof. Sanjay Kumar Ghosh		Date: 26/7/24

Final approval and acceptance of this thesis is contingent upon the candidate's submission of the final copies of the thesis to HBNI.

I hereby certify that I have read this thesis prepared under my direction and recommend that it may be accepted as fulfilling the thesis requirement.

Date: 26/7/2024

Place: KOLKATA

Signature

Guide

[1] This page is to be included only for final submission after successful completion of viva voce.

STATEMENT BY AUTHOR

This dissertation has been submitted in partial fulfilment of requirements for an advanced degree at Homi Bhabha National Institute (HBNI) and is deposited in the Library to be made available to borrowers under rules of the HBNI.

Brief quotations from this dissertation are allowable without special permission, provided that accurate acknowledgement of source is made. Requests for permission for extended quotation from or reproduction of this manuscript in whole or in part may be granted by the competent authority of HBNI when in his or her judgement the proposed use of the material is in the interest of scholarship. In all other instances, however, permission must be obtained from the author.

Vivek Kumar Singh

DECLARATION

I, hereby declare that the investigation presented in the thesis has been carried out by me. The work is original and has not been submitted earlier as a whole or in part for a degree / diploma at this or any other Institution / University.

Vivek Kumar Singh

List of Publications arising from the thesis

a. Publications in Referred Journals

1. "Fluctuations of identified particle yields using ν_{dyn} variable at energies available at the BNL Relativistic Heavy Ion Collider"
   Vivek Kumar Singh, Dipak Kumar Mishra and Zubayer Ahammed
   Phys. Rev. C 101, 014903 (2020)

2. "Study of diffusion coefficients of identified particles at energies available at BNL Relativistic Heavy Ion Collider"
   Vivek Kumar Singh, Dipak Kumar Mishra and Zubayer Ahammed
   Eur. Phys. J. A 56, 230 (2020)

b. Conference Proceedings

1. "Measurement of electrons from beauty-hadron decays in pp collisions at $\sqrt{s} = 2.76$ TeV to 13 TeV with ALICE"
   Vivek Kumar Singh for the ALICE Collaboration
   Oral presentation at 8^{th} International Conference on Physics and Astrophysics of Quark Gluon Plasma (ICPAQGP-2023), Puri, India

2. "Measurement of electrons from beauty-hadron decays in pp collisions at $\sqrt{s} = 2.76$ TeV to 13 TeV with ALICE"
   Vivek Kumar Singh for the ALICE Collaboration
   Poster presentation at XXV DAE-BRNS Symposium on High Energy Physics 2022, Mohali, India

3. "Charge fluctuations of identified particles at RHIC energies"
   Vivek Kumar Singh, Dipak Kumar Mishra and Zubayer Ahammed
   Proceedings of the DAE International Symp. on Nucl. Phys. 63 (2018) 960-962
   Poster presentation at DAE Symposium on Nuclear Physics 2018, Mumbai, India

c. ALICE Analysis Note

1. "Measurement of electrons from beauty-hadron decays in pp collisions at $\sqrt{s} = 13$ TeV with ALICE"
   Vivek Kumar Singh, Deepa Thomas, Martin Völkl and Zubayer Ahammed
   https://alice-notes.web.cern.ch/node/1230.

d. Contributions to other conferences

1. "Measurement of electrons from beauty-hadron decays in pp collisions at $\sqrt{s} = 13$ TeV with ALICE"
   Jonghan Park and **Vivek Kumar Singh** for the ALICE Collaboration
   Poster presentation at Quark Matter 2022 conference, Krakow, Poland

Vivek Kumar Singh

Dedicated to my beloved family members

My Father – Rajeshwar Singh

My Mother – Hemwanti Devi

My Sister – Archana Singh

– माँ, आप हमेशा मेरे जीवन का आशीर्वाद रहेंगी।

ACKNOWLEDGEMENTS

I want to express my sincere gratitude to the following individuals and organizations for their invaluable guidance, support and assistance throughout my PhD journey:

First and foremost, I am deeply grateful to my supervisor, Dr. Zubayer Ahammed for his guidance, mentorship, and unwavering support throughout this research endeavour. I would like to extend my appreciation to the team leader Dr. Subhasis Chattopadhya, for their continuous guidance, constructive feedback, and valuable insights throughout the course of my research. Their leadership and expertise have been crucial in shaping the direction of my work. Their expertise and encouragement have been instrumental in shaping my research and academic growth.

I am deeply thankful to the esteemed members of my Doctoral Committee: Dr. Partha Pratim Bhaduri and Dr. Sourav Sarkar from VECC, Kolkata, and Prof. Sanjay Kumar Ghosh from Bose Institute, Kolkata. Their consistent evaluation through annual progress seminars and invaluable feedback has been instrumental in shaping my research trajectory.

I sincerely thank Dr. Dipak Mishra, my summer project mentor, during my Post MSc. tenure at BARC Mumbai. The summer project that I collaborated on with him, along with the guidance from my PhD supervisor, resulted in the publication of two phenomenology papers in peer-reviewed journals. These publications played a crucial role in meeting the UGC criteria for my PhD journey. Working with Dr. Mishra was professionally enriching and personally gratifying, as he treated me as a friend. He played an integral role in helping me understand the ROOT-based data analysis framework and guided me through the transitional phase of becoming a research practitioner during the initial stages of my PhD. His support has been immeasurable, and I am sincerely thankful for his mentorship and friendship.

I am sincerely thankful to the convenors of PAG-HFE/HFL (Physics Analysis Group - Heavy Flavor Electrons/Heavy Flavor Leptons) and the PWG-HF (Physics Working Group - Heavy Flavor) – Dr. Andrea Dubla, Dr. Cristina Terrevoli, Dr. Deepa Thomas, Dr. Martin Andreas Völkl, and Dr. Nicole Bastid, for their invaluable guidance and diligent review of my analysis. Their willingness to address all my doubts, provide constructive feedback, and suggest various checks to ensure the correctness of my work has been immensely helpful. Their support, assessment, and constructive criticism have been immensely valuable. I have learned a great deal from their expertise, and their guidance has helped refine my research. I am genuinely thankful for their support and mentorship throughout my scientific journey.

I want to convey my sincere appreciation to the ALICE Analysis Review Committee members, Dr. Shingo Sakai and Dr. Minjung Kim. Their diligent reviews of my analysis during the Quark Matter 2022 preliminary campaign and Dr. Shingo's consistent guidance and evaluation of my work in PAG-electrons and PAG-HFE/HFL from inception to the present have been of immense value.

I want to thank my senior friends in the PAG-HFL sincerely, Dr. Erin, Dr. Jonghan, Dr.

Preeti, Dr. Shreyasi, and Dr. Sudhir, for their invaluable assistance and support in various aspects of my work. Dr. Preeti for her guidance in initiating the EMCal framework, and Dr. Jonghan Park and Dr. Shreyasi for their assistance in comparing and aligning the results with their findings. Their support and expertise have been invaluable in advancing my research. They consistently provided suggestions, recommended checks, and offered valuable insights on the next steps, enabling me to progress effectively.

I also want to thank Prasun-da, Abhishek-da, Ashik-da, and the entire grid lab team at VECC for their exceptional technical assistance with hardware and software throughout my journey.

I want to express my heartfelt appreciation to the Dean of Physical Sciences, Dr. Jane Alam and Dr. Parnika Das, for their exceptional teaching skills, guidance, encouragement and unwavering commitment to our academic development. Their expertise and leadership have been instrumental in creating a conducive educational environment within the department.

Furthermore, I would like to acknowledge the efforts of the Physics Group in organizing a series of informative seminars by eminent speakers. These seminars have covered a wide range of topics, from classical literature to recent developments in the field. Attending these seminars has enriched my knowledge and provided valuable insights into the latest advancements in our research area.

I am sincerely thankful to Dr. Tilak Ghosh, the Dean of Student Affairs, for his caring attitude and genuine concern for the welfare of the students. He consistently ensured that the students residing in the hostel were doing well and made himself available in case of any emergencies. His friendly and approachable nature fostered a sense of comfort and security among the students. Additionally, on special occasions and festivals he would take us out for dinner each year. These moments allowed us to bond as a community and create cherished memories.

I am extending my sincere appreciation to the members of the Junior Committee of ALICE India collaboration, namely Debjani, Meenakshi, Pritam, and Ravindra, during my tenure as the Junior Representative from 2020 to 2022.

I sincerely thank the caretaker of VECC Guest House and the dedicated canteen staff for their exceptional service in providing food and accommodation, especially during the challenging times of the COVID-19.

I sincerely thank Deepak Shirke, Dy.CSO VECC and the security team for their constant support in securing permissions that allowed me to work freely during Silent Hours and Holidays. Their assistance made a significant difference, and I'm grateful for their kindness and cooperation.

I am grateful to the ALICE India Collaboration Participating Institutes at IIT Bombay, IIT Indore, NISER Bhubaneswar and CERN, Geneva, for their hospitality and assistance during my PhD tenure.

I sincerely thank Prof. Anuradha Misra, my MSc. thesis supervisor, and Assistant Prof. Siddharth Kasturiranjan, my mentors during my masters at the University of Mumbai. Their

roles as exceptional educators extended beyond the classroom; they provided guidance that shaped pivotal decisions in my academic journey. Their insight and encouragement led me to choose the path of higher education and enrollment in a PhD program, focusing on experimental high-energy physics, instead of pursuing a conventional job after completing my master's. Their mentorship has been transformative, and I am genuinely thankful for their unwavering support.

I am immensely grateful to all my seniors, juniors, and colleagues, Ajit, Anandgopal, Apar, Arun, Ashik, Ashish, Debojit, Devesh, Imran, Jagbir, Joy, Kirti, Krishan Gopal, Mitali, Pawan, Rajkumar, Sanchari, Samrangy, Shabir, Sinjhini, Snigdha, Summit and Yoshini for their generous support and assistance in every aspect. Their guidance, knowledge-sharing and collaborative spirit have been invaluable throughout my journey. Whether offering advice, providing resources, or simply being there to lend a helping hand, their contributions have played a significant role in my personal and professional growth. I am truly thankful for their unwavering support and the camaraderie we share.

I am deeply grateful to my friends Ashish, Dayesh, Deepesh, HariGovind, Kamalnayan and Siddhesh for their unwavering support and inspiration during the challenging times of my PhD journey. Their encouragement, motivation, and belief in my abilities have been instrumental in helping me persevere and overcome obstacles. Their unwavering presence and positive influence have played a crucial role in keeping my spirits high and reminding me of the importance of not giving up. I am sincerely thankful for their friendship and their immeasurable impact on my academic pursuits.

Finally, I am forever indebted to my beloved parents and dearest sister, who have supported me throughout my academic journey. Their unwavering belief in education's value and constant encouragement has been invaluable. I owe their love, sacrifices, and steadfast faith in my abilities. Their presence in my life is truly a blessing.

I would like to extend my heartfelt gratitude to all those individuals who may not have been explicitly acknowledged in this space. Your contributions, whether in the form of guidance, encouragement, or even a simple conversation, have been significant in shaping my academic journey. I am sincerely thankful for your presence in my life. If I have unintentionally omitted your name, please accept my apologies. The support and influence of each person have been meaningful, and I deeply value the collective impact you've had on my growth.

Vivek Kumar Singh

Contents

SYNOPSIS

(Limited to 10 pages in double spacing)

The purpose of our scientific journey is to connect the fundamental principles of nuclear physics to the exploration of the early universe through experimental high-energy physics. For this purpose we focus on understanding the Quark-Gluon Plasma (QGP) and its significance in unraveling the mysteries of the Big Bang. Building upon the decades of research on baryonic matter at low energies performed at accelerator facilities such as AGS and SPS, we hunt through yet uncharted territories of QCD phase space through cutting-edge experiments like Relativistic Heavy Ion Collider (RHIC) at Brookhaven National Laboratory (BNL) and A Large Ion Collider Experiment (ALICE) at the Large Hadron Collider (LHC) at CERN. Conclusive evidence for a strongly coupled QGP formation has been provided by the data collected from these collider facilities. This thesis explores the low and high energy regimes of the QCD phase diagram from various angles. To explore the high-temperature regime of the QCD phase space, heavy-flavor quarks such as charm and beauty quarks provide unique insights which are missing for other probes. Besides the study of experimental data, phenomenological studies were also conducted by comparing experimental measurements with theoretical models. In order to investigate the low-temperature regime of the QCD phase space, analysis of net charge and identified particle fluctuations along with the estimation of diffusion coefficients in rapidity space is carried out using the HIJING and UrQMD models at various collision energies available at RHIC. These studies lead to a comprehensive understanding of the properties and dynamics of QCD matter across a range of collision energies.

One of the main objectives of heavy-ion experiments is to study the phase transition from hadronic matter to QGP. Event-by-event fluctuation of conserved quantities such as net-baryon number, net-electric charge and net-strangeness were proposed as possible signals of the QCD phase transition [1]. The Beam

Energy Scan (BES) program at RHIC was initiated to explore the QCD phase diagram and study the transport properties of nuclear matter at different collision energies and particle species (indirectly varying temperature(T) and net-baryon (μ_B) density). At RHIC, the baryon chemical potential is estimated to reach upto $\mu_B \sim 400$ MeV at lower collision energies. A strong gradient in the chemical potential of conserved charges are expected at such lower energies. Hence, low energy beam scan at RHIC can be useful to explore the properties of charge particle diffusion of nuclear matter which were out of reach in high energy collisions.

A study investigating event-by-event fluctuations of net-charge, net-pion, net-kaon, and net-proton using the variable $\nu_{(\pm,\mathrm{dyn})}$ in various models, such as the hadron resonance gas model (HRG), the heavy-ion jet interaction generator (HIJING), and the transport model ultrarelativistic quantum molecular dynamics (UrQMD), at different collision energies available at the BNL RHIC has been published in Ref. [2, 3]. In this study, a dataset comprising 0.2 million central (0–5%) Au+Au events at RHIC energies, generated using the HIJING and UrQMD models, was employed for the analysis. The transverse momentum (p_{T}) range considered for the particles is $0.2 \leq p_T$ (GeV/c) ≤ 5.0, with the lower p_{T} threshold was motivated by experimental measurements conducted at RHIC. The $\langle N_{\mathrm{ch}}\rangle\nu_{(\pm,\mathrm{dyn})}$ values were evaluated as a function of $\Delta\eta$ and $\sqrt{s_{_{NN}}}$, covering a broad rapidity window ($0 \leq \Delta\eta \leq 5$). A pronounced dependence of the $\langle N_{\mathrm{ch}}\rangle\nu_{(\pm,\mathrm{dyn})}$ values was observed on lower $\Delta\eta$. A decreasing trend persisted up to higher $\Delta\eta$, albeit with a lower slope in both models for all cases, except for the net protons in the UrQMD model. In the UrQMD model, the curvature of $\langle N_{\mathrm{ch}}\rangle\nu_{(\pm,\mathrm{dyn})}$ values as a function of $\Delta\eta$ exhibited distinct behavior compared to the HIJING model, specifically for net protons. The dynamical fluctuations of net-kaons and net-protons were found to be larger than those measured for net-pions and net-charged particles. Additionally, the dynamical fluctuations of net-protons were somewhat larger than those of net-kaons. The $\langle N_{\mathrm{ch}}\rangle\nu_{(\pm,\mathrm{dyn})}$ values obtained from different model calculations were observed to be independent of collision energies, while

demonstrating clear particle species dependence.

The measured fluctuations may get diluted in the expanding medium due to the diffusion of the charged hadrons in the rapidity space [4–6]. The dissipation of fluctuations occurs during the evolution of the system from hadronization to their kinetic freeze-out. Hence, one should measure not only the magnitudes of fluctuation quantities at a fixed $\Delta\eta$ but also their dependence on $\Delta\eta$ enabling us to explore various aspect of the time evolution of the hot medium and the hadronization mechanism. The QGP suppression of the charge fluctuations is not observed in the experimental data, while the suppression of charge fluctuations observed in experimental data is consistent with the diffusion estimates. Both the suppressions are crucially different from each other. While the QGP suppression is the history effect, the critical fluctuations are the equilibrium fluctuations pertaining to the freeze-out point, and the diffusion is necessary to establish them [7].

The study presented in reference [3] is exploited to estimate the diffusion rate of identified particle species in different rapidity intervals at RHIC energies. The simulated data points of $\langle N_{\rm ch}\rangle\nu_{(\pm,{\rm dyn})}$ as function of $\Delta\eta$ are fitted with the error function, ${\rm Erf}(\Delta\eta/\sqrt{8}\sigma)$ representing the diffusion in rapidity space [5, 6]. The fit parameter σ, characterizes the diffusion parameter at freeze-out that accounts for the broadening of the rapidity distributions due to interactions and particle production. The slope of the fit function decreases with increasing particle mass. In the case of UrQMD model, the $\langle N_{\rm ch}\rangle\nu_{(\pm,{\rm dyn})}$ values of net-proton flattened at higher $\Delta\eta$ with increasing $\sqrt{s_{_{NN}}}$. Hence, unlike pions and kaons, the $\langle N_{\rm ch}\rangle\nu_{(\pm,{\rm dyn})}$ as a function of $\Delta\eta$ for net-proton cannot be fitted with ${\rm Erf}(\Delta\eta/\sqrt{8}\sigma)$ function to extract the σ values. The extracted values of diffusion coefficient as a function of $\sqrt{s_{_{NN}}}$ shows the σ of net-proton and net-kaon are closer to each other and systematically higher than net-pion at all energies in both the models. The number density decreases for the more massive species. As a result, dilution of the dynamical fluctuations reduces which goes inversely proportional to the multiplicity. Therefore, the heavier particles are less diffused in comparison to the lighter

particles. The strangeness conservation and the baryon number conservation also influence the size of the dynamical fluctuations for the net-kaon and net-proton, respectively. The diffusion coefficients are constant as a function of studied collision energy range $\sqrt{s_{NN}}$ = 7.7 to 200 GeV. The results remain of interest so far, as they provide references for the behaviour of diffusion parameter according to the models considered [8]. The studies presented in Ref. [3, 8] set the baseline for the measurements at RHIC and the much awaited experimental data are needed in order to understand the particle production mechanisms.

In addition to heavy-ion programme, the LHC experiments also utilize proton beams for proton-proton (pp) collisions. These binary collisions provide reference data for a system without QGP as opposed to that observed in the heavy-ion collisions. Given the significantly smaller size of protons compared to Au or Pb ions, the formation of a QGP medium was not anticipated in these small systems. However, contrary to the expectations, results from the LHC have revealed soft signatures of QGP medium at high multiplicity in small system collisions, such as collective flow and strange baryon enhancement. As a result the study of particle production in high energy pp collisions with a focus on multiplicity dependence, has become crucial in comprehending the particle production mechanism in these systems.

Heavy quarks (charm and beauty), due to their large masses, are primarily produced during the hard scattering process at the early stage of hadronic collisions [9]. They witness the full evolution of the QGP in ultra-relativistic heavy-ion collisions. As they traverse through the QGP medium, they undergo elastic and inelastic collisions with its constituents, resulting in energy loss. Therefore, heavy quarks serve as excellent probes for investigating the properties of the QGP. The masses of charm and beauty quarks, denoted as $m_{c,b}$ (1.3, 4.2 GeV/c^2), also exceed the QCD scale parameter ($\Lambda_{\rm QCD} \approx 200$ MeV). As a result, the production cross section of heavy-flavour particles can be calculated down to zero $p_{\rm T}$ using perturbative QCD (pQCD). In pp collisions, the measurement of the beauty-hadron

production cross section is important to test the pQCD calculations. The measurement in pp collisions also serve as a baseline for studying nuclear modifications in proton-nucleus (p-A) and nucleus-nucleus (A-A) collisions. In p-A collisions, these studies offer insights into the effects of cold nuclear matter while in A-A collisions, they provide an opportunity to investigate the impact of the QGP on heavy quarks as they traverse through the medium. [10–13].

Heavy-flavor (HF) particles, due to their short lifetime, are studied solely from their decay products. In the ALICE experiment, the investigation of open heavy-flavor production employs two complementary approaches. 1) Full reconstruction of the decayed particles by using an invariant mass technique to determine the parent heavy-flavour particle from the hadronic decay channels [14]. 2) Measurement of leptons originating from the leptonic or semi-leptonic decay channels of heavy-flavour hadron [14]. In this thesis, we have focused on the semi-electronic decay mode, i.e. the decay of heavy-flavour particles into an electron, neutrino, and one or more hadrons through weak interactions. Due to the undetectable neutrino, it is not possible to fully reconstruct the four-momentum of the parent hadron therefore, to measure the yield of heavy-flavour decay electrons, a data-driven technique is employed [15].

The analysis utilizes the pp collisions data at a center-of-mass energy $\sqrt{s}$ = 13 TeV collected by the central-barrel detectors in the mid-rapidity region at ALICE during 2016 to 2018. The Inner Tracking System (ITS) is used for determining the reconstructed primary and secondary vertices, as well as for tracking. The Time Projection Chamber (TPC) is also used for tracking, particle identification (PID) and momentum measurement of charged particles. The Electromagnetic Calorimeter (EMCal) is employed for electron identification and triggering to select high p_{T} electron events. In this study, events triggered by the minimum bias (MB) selection are used for the lower p_{T} range ($3 \leq p_{\mathrm{T}}$ (GeV/c) ≤ 6). While two specific EMCal triggered events, EG2 and EG1, with two different energy thresholds, are used to provide the necessary statistics for extending the measurement

to higher p_{T} range. The trigger threshold for EG2 is $\sim$ 4.5 GeV, allowing for the measurement of the region $6 \leq p_{\mathrm{T}}$ (GeV/c) ≤ 12. Similarly, the EG1 trigger with a threshold $\sim$10.5 GeV is utilized to measure the region $12 \leq p_{\mathrm{T}}$ (GeV/c) ≤ 35 [16].

In TPC, particle identification is performed by measuring the specific energy loss (dE/dx) from the gas within the TPC as a function of the charged particle's momentum. Electrons are selected within the range of -1 $\leq$ $\mathrm{n}_{\sigma,\mathrm{e}}^{\mathrm{TPC}}$ $\leq$ 3, where $\mathrm{n}_{\sigma,\mathrm{e}}^{\mathrm{TPC}}$ represents the deviation of the measured signal in the detector from the expected value for electrons, expressed in terms of the detector resolution i.e. $\mathrm{n}_{\sigma,\mathrm{e}}^{\mathrm{TPC}} = [(\mathrm{d}E/\mathrm{d}x)_{\mathrm{measured}} - (\mathrm{d}E/\mathrm{d}x)_{\mathrm{expected}}] \div \sigma^{\mathrm{TPC}}$. The $\mathrm{n}_{\sigma,\mathrm{e}}^{\mathrm{TPC}}$ distribution shows that the bands corresponding to pion, kaon, and proton pass through the electron band in the lower momentum region. On the contrary, in the higher momentum region, these bands merge ($p > 6$ GeV/c). This limits the TPC's capability for particle identification at both lower and higher momentum regions. To achieve high purity electron identification, the selected electron candidate tracks within the TPC are projected onto the surface of the EMCal taking into account the ALICE magnetic field (0.5T). Thus, TPC along with the EMCal is used for electron identification(eID) in the low and high p_{T} regions.

When electrons pass through the EMCal detector they generate an electromagnetic shower and deposit all of their energy in the form of clusters. The total energy (E) deposited by the electrons in the EMCal is expected to be equal to their momentum (p) as measured by the TPC. Therefore, the ratio of the energy deposited in the EMCal to the momentum (E/p) is approximately 1. Unlike electrons, hadrons do not deposit their entire energy in the EMCal due to their interactions primarily occurring via the strong nuclear force. As a result, the ratio E/p for hadrons is expected to be less than 1. To ensure that the selected clusters are originated from electron showers and not from photons, a p_{T} dependent track-cluster matching cut is employed. EMCal clusters are matched to tracks from the TPC, where photons are eliminated, since they do not leave a signal in the TPC [16].

In order to further enhance the purity of the selected electron sample and minimize contamination from hadrons, a p_{T} -dependent cut is applied to the major axis (M02) of the shower shape ellipse [16] while ensuring that there is no major impact on the electron selection efficiency. To estimate the residual hadron contamination in each p_{T} bin of the electron sample, the E/p distribution of hadrons is obtained seperately by selecting particles with $\mathrm{n}_{\sigma,\mathrm{e}}^{\mathrm{TPC}}$ < -3.5 and M02 cut. The E/p distribution of hadrons is then scaled to match the E/p distribution of electron candidates within E/p < 0.7. The scaled hadron contribution is subtracted from the E/p distribution of electron candidates, resulting in the E/p distribution of inclusive electrons [15].

The smallest distance between the reconstructed track and the reconstructed primary vertex in (XY) plane perpendicular to the (Z) beam axis is called the impact parameter (d_0) or Distance of closest approach (DCA) [17]. For this analysis, electrons and positrons are treated identically, differing only in the charge factor multiplied to the . The d_0 distribution of particles, satisfying the conditions of 0.85 < E/p < 1.2 and passing the M02 cut, within the range of $-1 \leq \mathrm{n}_{\sigma,\mathrm{e}}^{\mathrm{TPC}} \leq 3$ provides the inclusive electron d_0 distribution in each p_{T} bin. Similarly, the d_0 distribution of particles passing the same E/p and M02 cut, but with $\mathrm{n}_{\sigma,\mathrm{e}}^{\mathrm{TPC}}$ < -3.5, provides the hadron d_0 distribution for each p_{T} bin. To account for contamination, the d_0 distribution of the hadrons is scaled to match the level of contamination observed in the scaled E/p distribution of hadrons within individual p_{T} bins.

The dominant background for non-heavy-flavour (non-HF) electrons in the detector arises from the Dalitz decay of light neutral mesons (π^0 and η) and the conversion of photons to electrons in the detector material. These electrons, collectively referred to as photonic electrons, are produced in electron-positron (e^-e^+) pairs, while electrons from heavy-flavour (HF) decays are always single particles. This distinction allows for the segregation of photonic electrons based on their invariant mass distribution, which unlike HF decays, exhibits a peak at low invariant mass. The inclusive electron sample contains both corre-

lated pairs (from photonic decays) and random uncorrelated pairs (combinatorial background) as seen in the invariant mass spectra of unlike sign (ULS) and like sign (LS) paired electrons. However, not all photonic electrons can be identified using the invariant mass method, as some pairs may have its partner electron outside the detector acceptance or fail the selection criteria. To correct for this effect, the tagging efficiency (ϵ_{tag}) is calculated using Monte Carlo simulations, and the d_0 distribution of photonic electrons is obtained by subtracting the d_0 distributions of LS from the ULS paired electrons within an invariant mass cut of $m_{e^+e^+} < 0.14$ GeV/c^2, scaled by the tagging efficiency.

$$\frac{\mathrm{d}N^{\mathrm{Photonic}}}{\mathrm{d}d_0} = \frac{1}{\epsilon_{\mathrm{tag}}}\left(\frac{\mathrm{d}N^{\mathrm{ULS}}}{\mathrm{d}d_0} - \frac{\mathrm{d}N^{\mathrm{LS}}}{\mathrm{d}d_0}\right) \tag{1}$$

However, it should be noted that electrons originating from the decays of $W^{\pm}$ and Z bosons also contribute to the background, particularly in the higher p_{T} range. The total contribution of W/Z decay electrons has been determined through PYTHIA+POWHEG simulations [15]. For $p_{\mathrm{T}} < 15$ GeV/c, the contribution of W/Z decay electrons is negligible, $\sim 12\%$ at p_{T} 25-30 GeV/c and $\sim 40\%$ at p_{T} 30-35 GeV/c. The subtraction of the contribution from W/Z decay electrons has not been performed in this analysis and will be addressed later.

Electrons originating from beauty quark decays are measured using the d_0 fit method. The d_0 templates of hadrons, photonic electrons from experimental data, and beauty and charm-decay electrons from Monte Carlo (MC) simulations are fitted to the d_0 distribution of inclusive electrons. This fitting is performed using the maximum likelihood approach [18], where the amplitudes for hadron and photonic electrons are fixed. The fit yields the free amplitudes p_0 and p_1, which represent the raw yield of electrons originating from beauty and charm quarks, respectively.

$$fit = p_0.(Beauty) + p_1.(Charm) + p_2.(Hadron) + p_3.(Photonic) \tag{2}$$

These amplitudes are obtained by taking into account the statistical fluctuations present in the data and templates. Triggered events provide a higher statistical yield of electrons required to reach the high p_{T} region, but they also introduce a bias at the cluster energy level. Consequently, the measured raw yield with EG2 and EG1 triggered events is significantly higher than that with MB events. To account for this mismatch, the yields measured with EG2 and EG1 events are normalized using trigger rejection factors to match the equivalent MB events. Additionally, the measured yields are corrected for reconstruction efficiency to account for detector effects and particle identification efficiencies. The reconstruction efficiency is calculated as the ratio of electrons passing all geometric, track quality and particle identification selection criteria to the total number of generated electrons within the same acceptance in the MC sample.

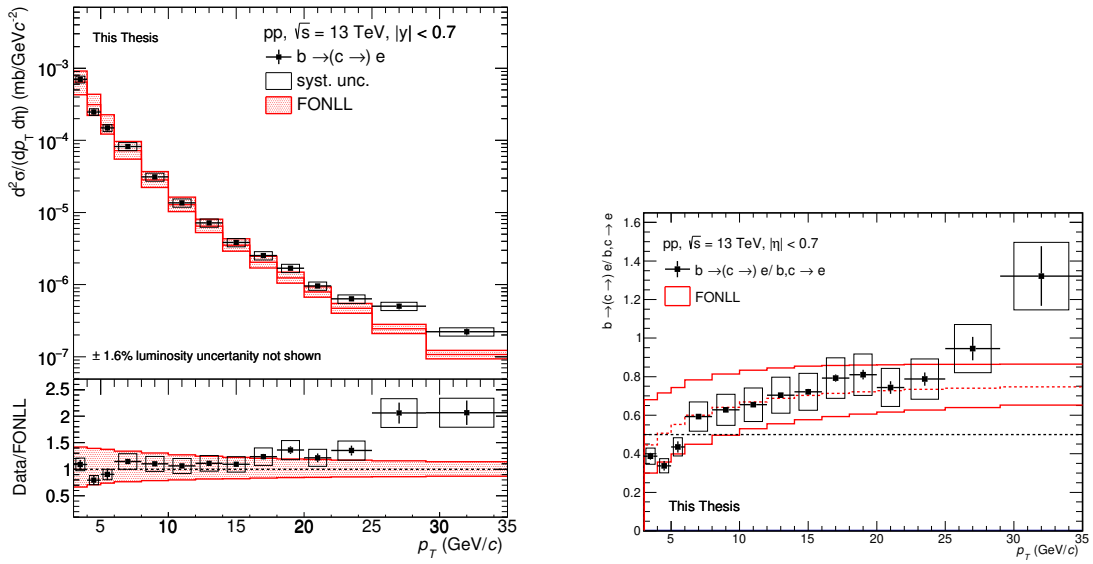

(a) (b)

Figure 1: (a) The p_{T} -differential cross section of electrons from beauty-hadron decays compared with FONLL. (b) The relative fraction of electrons from beauty hadron decays to electrons from heavy-flavour hadron decays.

Figure 1 (a) shows the comparison between the p_{T} -differential production cross section of electrons from beauty hadron decays and the corresponding pQCD predictions obtained using the FONLL (Fixed Order Next-to-Leading Logarithm) framework [19]. The measured cross section is found to be in agree-

ment with FONLL within the uncertainties of the data. However, in the range $4 < p_{\mathrm{T}}$ (GeV/c) < 6, the data underestimates the FONLL central value, while in the range $16 < p_{\mathrm{T}}$ (GeV/c) < 20, the results are found to lie on the upper edge of FONLL. For $p_{\mathrm{T}} > 20$ GeV/c, the data points are observed to be significantly higher than FONLL predictions, which can be attributed to the contribution of W/Z boson decay electrons that dominate this p_{T} range and were not corrected for in the measured data. The relative contribution of the electron from beauty quarks to the total heavy-flavour electron contribution has been investigated and presented in figure 1 (b). The production cross section of electrons from heavy-flavour hadron decays has been utilized to estimate the beauty hadron decay electron fraction. These ratios have been compared to FONLL predictions and demonstrate consistency within the uncertainties of the model. It is worth noting that the beauty contribution dominates the total heavy-flavour electron contribution for $p_{\mathrm{T}} > 6$ GeV/c. Overall, these results provide valuable insights into the production and relative contributions of electrons from beauty hadron decays, and their comparison with the pQCD predictions enhances our understanding of the heavy-flavour physics in the high-energy collisions. Further investigations, including the correction for W/Z boson decay electrons, will be crucial in refining these measurements and obtaining a comprehensive understanding of the heavy-flavour electron production.

References

[1] S. Jeon and V. Koch, Phys. Rev. Lett. **85**, 2076 (2000).

[2] D. K. Mishra, P. K. Netrakanti and P. Garg, Phys. Rev. C **95**, 054905 (2017).

[3] V. K. Singh, D. K. Mishra and Z. Ahammed, Phys. Rev. C **101**, 014903 (2020).

[4] E. V. Shuryak and M. A. Stephanov, Phys. Rev. C **63**, 064903 (2001).

[5] M. A. Aziz and S. Gavin, Phys. Rev. C **70**, 034905 (2004).

[6] B. Abelev *et al.* [ALICE Collaboration], Phys. Rev. Lett. **110**, 152301 (2013).

[7] Y. Hatta and M. A. Stephanov, Phys. Rev. Lett. **91**, 102003 (2003), Erratum: [Phys. Rev. Lett. **91**, 129901 (2003)].

[8] V. K. Singh, D. K. Mishra and Z. Ahammed, Eur. Phys. J. A **56**, 230 (2020).

[9] Andronic, A., Arleo, F., Arnaldi, R. *et al*. Eur. Phys. J. C **76**, 107 (2016).

[10] ALICE Collaboration. Phys. Lett. B **738**, 97-108 (2014).

[11] ALICE Collaboration. Phys. Lett. B **721**, 13-23 (2013).

[12] ALICE Collaboration. J. High Energ. Phys. 2017, **52** (2017).

[13] ALICE Collaboration. arXiv:2211.13985 [nucl-ex].

[14] P.A. Zyla *et al*. (Particle Data Group), Prog. Theor. Exp. Phys. **2020**, 083C01 (2020).

[15] ALICE Collaboration. arXiv:2303.13349 [nucl-ex].

[16] ALICE Collaboration. arXiv:2209.04216v1 [physics.ins-det].

[17] M. Volkl. Thesis, "Electrons from beauty-hadron decays in central PbPb collisions at $\sqrt{s_{NN}}$ = 2.76 TeV", University of Heidelberg (2016).

[18] R. Barlow and C. Beeston, Comp. Phys. Commun. **77** (1993) 219-228.

[19] Cacciari, M., Frixione, S., Houdeau, N. *et al*. J. High Energ. Phys. **2012**, 137 (2012).

List of Figures

List of Tables

Chapter 1

Introduction

Our scientific endeavour seeks to find a connection between the foundational principles of nuclear physics and the exploration of the nature of the early universe through experimental high-energy physics. At the heart of this endeavour lies the profound quest to understand the famous Quark-Gluon Plasma (QGP)[1] [1, 2] and its pivotal role in unravelling the mysterious events of the Big Bang. The QGP, a strongly interacting deconfined state of quarks and gluons, was anticipated to have existed shortly after the Big Bang [3], representing a critical phase in the growth of the early early universe. Quantum ChromoDynamics (QCD), a branch of quantum field theory, explains the mechanisms behind strong interactions, defining the the rules of intricate dance between quarks and gluons within this unique state. This distinctive domain, where quantum chromodynamics dictates the dynamics of strong forces, can be observed at the stage of heavy-ion collisions. Through these collisions, we seek to unravel the intricate relationship between the laws governing elementary particle physics and the emergence of collective phenomena. The quest to experimentally identify and understand this deconfined state began at the Super Proton Synchrotron[2] (SPS) at European Organization for Nuclear Research (CERN) and the Alternating Gradient Synchrotron[3] (AGS) at Brookhaven National Laboratory (BNL) in the 1980s [4]. Building on these pioneering efforts, Relativistic Heavy Ion Collide (RHIC) at BNL has also provided some compelling results, strongly indicating the formation of the elusive Quark-Gluon Plasma, marking a significant achievement in our exploration of the

[1] "Quark-Gluon Plasma" is a (locally) thermally equilibrated state of matter in which fundamental particles, quarks, and gluons, are no longer confined within hadrons but are free to move independently over a hadronic volume scale. This deconfined state is characterized by extremely high energy densities and temperatures, resembling a hot, dense soup of quarks and gluons.

[2] The SPS was a major upgrade from the Proton Synchrotron (PS was CERN's first large accelerator, started in 1959), started in 1976, and could accelerate protons and heavy ions to even higher energies. Now, it 9serves as an injector for the Large Hadron Collider (LHC).

[3] The AGS accelerated protons and other heavy ions to high energies before injecting them into the RHIC ring for further acceleration and collisions. It played a crucial role in the early stages of RHIC experiments, providing the necessary beams for the study of high-energy nuclear physics, including the exploration of the QGP.

early universe [5–9].

A pertinent objective of the research program in relativistic heavy-ion collisions is to explore the phase structure of strongly interacting matter at different temperatures (T) and baryonic chemical potential ($\mu_{\rm B}$). Depending on the collision energy, experiments can access different T and $\mu_{\rm B}$ regions. Consequently, systems with small $\mu_{\rm B}$ but high T are generated at top RHIC and LHC energies. Data from these collider facilities have also demonstrated the formation of strongly coupled QGP. In contrast, the QCD phase diagram is less explored in the high $\mu_{\rm B}$ region. Hence, initiatives like the ongoing Beam Energy Scan (BES) program at RHIC [10], upcoming heavy-ion collision experiments at the Nuclotron-based Ion Collider (NICA) [11, 12] and the Facility for Antiproton and Ion Research (FAIR) [13, 14] aim to investigate the moderate T and high $\mu_{\rm B}$ regime of the QCD phase diagram [15]. Apart from the heavy-ion programs, LHC experiments also utilize proton beams for proton-proton (pp) collisions. Unlike heavy-ion collisions, these binary collisions serve as a baseline measurement for systems without QGP. Although we expected that the smaller size of the protons compared to gold or lead ions would not lead to the formation of a QGP medium, the results from the LHC have defied these assumptions. Soft signatures of QGP medium, such as collective flow [16, 17] and strange baryon enhancement [18], have been revealed at high multiplicities in small system collisions. Therefore, studying particle production in high-energy pp collisions (mainly focusing on multiplicity dependence) is crucial to understanding the particle production mechanism in these systems [19].

This thesis aims to investigate the low and high energy regions of the QCD phase diagram from different angles. In order to explore the low-temperature domain of the QCD phase space, an analysis is conducted on the net-charge and identified particle fluctuations. Additionally, the estimation of diffusion coefficients in rapidity space is performed using the Heavy-Ion Jet Interaction Generator (HIJING) [20] and UltraRelativistic Quantum Molecular Dynamics (UrQMD) [21] models at various collision energies available at RHIC. The study aims to estimate the strength of these fluctuations and diffusion rates in the rapidity space, further clarifying their dependence on parameters such as particle mass, collision energies, strangeness conservation, and baryon number conservation for identified particle species [22, 23]. Investigating the high-temperature domain of the QCD phase space involves gaining unique insights through studying heavy-flavour quarks, such as charm and beauty, which are rare probes. The study utilizes data from the ALICE experiment at LHC, CERN, explicitly measuring the production cross-section of electrons from beauty-hadron decays in pp collisions at a centre-of-mass energy of $\sqrt{s}$ = 13 TeV. The primary objectives include exploring electrons from beauty-hadron decays in a higher transverse momentum ($p_{\rm T}$) range, extending up to $p_{\rm T}$ = 35

GeV/c, an unexplored domain within the ALICE experiment [24]. Additionally, the measurement tests perturbative QCD (pQCD) calculations and establishes a baseline for studying the nuclear modifications in proton-nucleus (p−A) and nucleus-nucleus (A−A) collisions. These studies offer insights into the effects of cold nuclear matter in p−A collisions [25, 26] and illuminate how the Quark-Gluon Plasma impacts the behaviour of heavy quarks as they traverse the medium in A−A collisions [27]. All these collective efforts lead to a comprehensive understanding of the properties and dynamics of QCD matter across a range of collision energies in both proton-proton and nucleus-nucleus collisions.

Chapter 1 delves into fundamental physics, providing an overview of contemporary measurements and the motivation behind our study. Moving on to Chapter 2, we explore the fluctuation strength of the charged particles, like net-charge, net-pion, net-kaon, and net-proton, utilizing models like the Hadron Resonance Gas (HRG), the HIJING and UrQMD. The results from these models serve as references for understanding the behaviour of fluctuations measured in experiments. Additionally, Chapter 2 covers the diffusion coefficient of identified charged particles, establishing a baseline for experimental measurements using the UrQMD and HIJING models. Chapter 3 describes the experimental apparatus, spanning from the LHC to the ALICE detector, in detail, with a particular focus on the ALICE electromagnetic calorimeter (EMCal), which plays a crucial role in the measurement of electrons from beauty-hadron decays in this thesis. Chapter 4 addresses the nuances of electron identification, outlining the selection and tagging process for electrons originating from semi-leptonic bottom decay. A comprehensive analysis strategy is presented, encompassing electron selection, background subtraction, and the estimation of p_{T} -differential cross-section. Systematic errors associated with the primary measurement components are thoroughly discussed and calculated, leading to the presentation of final results. Chapter 5 offers an overall summary of the thesis and the conclusions drawn from the measures conducted. Finally, in Chapter 6, we look at the future prospects, outlining potential measurements with Run3 data and the ALICE-O2 framework.

1.1 The Standard Model

The Standard Model is a theoretical framework that explains the composition and interactions of matter. It is built on the concept that all matter consists of particles, and these particles communicate through the exchange of propagators associated with the fundamental forces. The building blocks of day-to-day matter are fermions, characterized by half-integer spin values, while bosons, with integer spin values, act as force carriers. Fermions come in two varieties: leptons (which include the well-known electron) and quarks (found inside protons and neutrons).

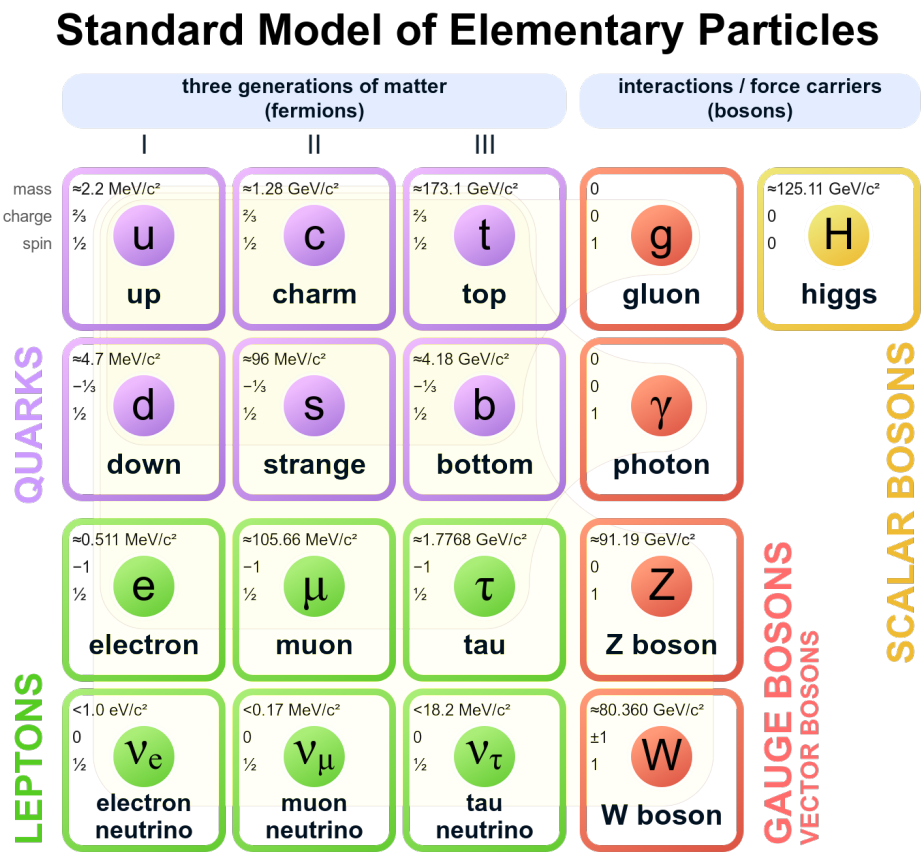

Figure 1.1: The representation of elementary particles within the Standard Model is organized into three generations, with masses increasing from left to right. Notably, gravity, a familiar force, is not included in the Standard Model, presenting a challenge in fitting it into this framework [28].

These particles interact through fundamental forces, each having specific force carriers [29].

Figure 1.1 illustrates the arrangement of elementary particles in the Standard Model, grouped into three generations with mass increasing from left to right. The six quarks and their respective anti-quarks, each with three colour charges[4] (red, green, and blue) [30, 31] and corresponding anti-colour charges, belong to these three generations. The first generation includes up and down quarks, electrons, and electron neutrinos. The second consists of strange and charm quarks, muons, and muon neutrinos, while the third involves top and bottom quarks, tau particles, and tau neutrinos. An entirely different particle category is called bosons, which include gauge bosons and scalar bosons. Gauge bosons act as force carriers for fundamental forces, with $W^{\pm}$ and Z^0 governing weak interactions, photons governing electromagnetic interactions and gluons serving as force carriers for strong forces. The Higgs boson, a recently discovered scalar boson, plays a crucial role by interacting with quarks, leptons, and itself to give masses to these particles [32–34].

[4]To avoid violating the Pauli exclusion principle, which forbids identical fermions from having the same quantum numbers, an additional quantum number called "colour" was introduced for quarks. This colour quantum number has three distinct values, allowing quarks with different colours to share identical quantum numbers.

Despite its success, the Standard Model has limitations. It lacks a description of gravity, one of the fundamental forces, and struggles to explain the vast difference in strength between gravity and other forces (the 'hierarchy' problem). The model must also catch up in accounting for the wide range of masses among the elementary particles. Additionally, it only addresses visible matter, while observational evidence suggests the existence of five times more populous dark matter, a mysterious form of matter with only gravitational effects and properties not matching any known particles of the Standard Model. Scientists had to devise remarkably mind-boggling advanced and complicated machines like the LHC and RHIC to explore particle properties and force behaviours more in-depth, aiming to answer fundamental questions about the universe [35–37].

1.2 Quantum Chromodynamics

Quantum Chromodynamics is a theoretical framework in physics that explains the strong force, one of the fundamental forces within the Standard Model. In QCD, quarks and gluons possess a unique property known as a colour charge. Unlike the electric charge in Quantum Electrodynamics (QED), which has a single value, the colour charge is more intricate; a proton, for example, comprises not only its three valence quarks (uud) but also gluons and quark-antiquark pairs arising from quantum fluctuations. While many quarks and gluons are within a proton, the colour confinement ensures that only colour-neutral combinations, or colour singlets, are observable particles. This implies that any bound state of quarks and antiquarks must show net colourlessness to the external environment. QCD introduces a running coupling constant, denoted as α_s, indicating that its strength varies with the scale or distance[5]. This dynamic nature results in two key features of QCD: (i) **Confinement**, where quarks are bound together in colour singlets at low energies (or long distances). (ii) **Asymptotic freedom**, which is dominant at high energies (or short distances), where quark and gluon interactions diminish, allowing them to behave like almost free particles [39, 40]. The potential between a quark and an anti-quark includes both Coulomb and linear terms, distinguishing it from the QED potential, which only has a Coulomb term[6]. The interaction strength between the quark-antiquark pair intensifies as their mutual separation increases. A new colourless hadron is generated if an amount of energy sufficient to create a quark-antiquark pair is provided to attempt to

[5]For QED, $\alpha = \frac{e^2}{4\pi\epsilon_0\hbar c} \sim 1/137$. However, for QCD, α_s is energy-scale-dependent, with its value commonly defined at the Z boson mass scale (m_{Z^2}). As of 2023, ATLAS measured $\alpha_s(m_{Z^2})$ to be 0.1183 ± 0.0009, the most precise measurement. Determinations of $\alpha_s(m_{Z^2})$ rely on various methods, including lattice QCD calculations, studies of tau-lepton decay, and reinterpretation of the Z boson's transverse momentum spectrum [38].

[6]QED: $V(r) \sim -\frac{e^2}{r}$ and QCD: $V(r) \sim -\frac{\alpha_s}{r} + \sigma r$, where σ is the colour string tension, refers to the linearly increasing potential energy between quarks and antiquarks at large distances, representing the confinement [41] of quarks within hadrons by a stretched colour flux 'string'.

separate them. At very short distances (smaller than the size of a nucleon), the effective coupling strength between quarks decreases logarithmically, approaching minimal values. In these conditions, quarks and gluons exhibit quasi-free behaviour.

$$\alpha_s(\mathrm{Q}^2) = \frac{g_s^2(\mathrm{Q}^2)}{4\pi} = \frac{12\pi}{(33 - 2n_f)\log\left(\mathrm{Q}^2/\Lambda_{QCD}^2\right)} \tag{1.1}$$

At high energies, the α_s can be expressed to the leading order, as given in Eqn. 1.1 [42], where Q^2 is the momentum transfer, n_f is the number of quark flavours, and Λ_{QCD}^2 is the non-perturbative momentum scale. A perturbative description applies when Q^2 is much larger than Λ_{QCD}^2, signifying weakly interacting quarks and gluons. At the same time, when Q^2 is around Λ_{QCD}^2, non-perturbative effects become significant, leading to the formation of strongly bound hadronic clusters, marking a transition from quasi-free partons (quark or gluon) to the world of hadrons like pions and protons. The value of Λ_{QCD}^2 is an experimentally determined parameter [42, 43], expected to be of the order of a typical hadronic mass[7]. While pQCD successfully describes physics at high energies, it becomes inadequate at lower energies, demanding alternative methods.

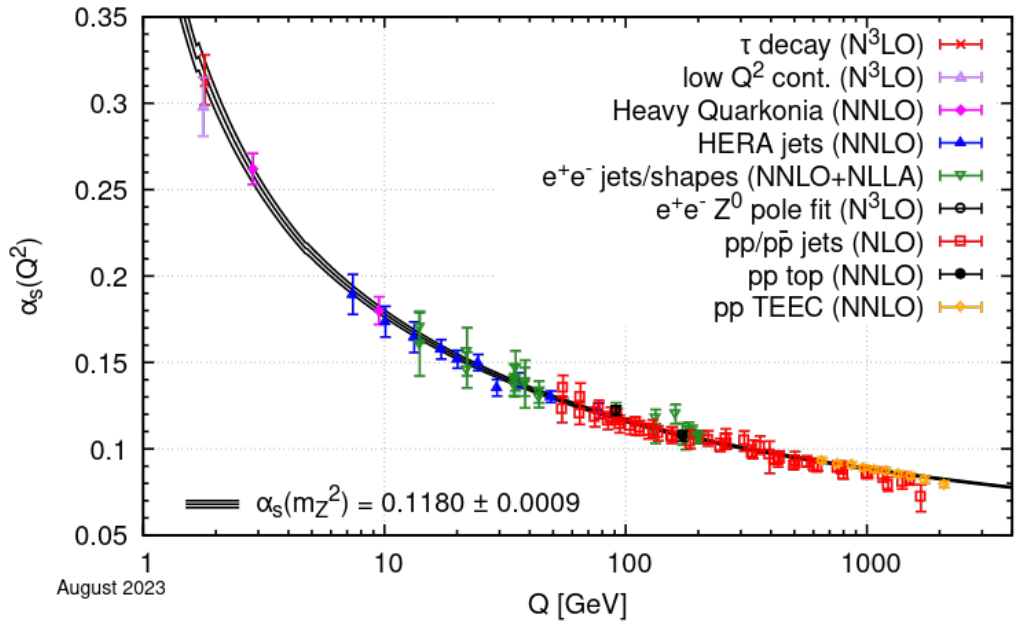

Figure 1.2: Comparison of determinations of the strong coupling constant α_s as a function of the energy scale Q, with the running of the coupling computed at five loops using the current PDG average $\alpha_s = 0.1180 \pm 0.0009$ as an input. The figure summarizes various measurements of α_s, highlighting their dependence on energy scale Q. The image is sourced from PDG [44], providing a pictorial representation of experimental determinations compared to the theoretical prediction based on QCD calculations.

[7]The value of Λ is 332 ± 17 MeV for processes involving up, down, and strange quarks (energies below 1.275 GeV) and decreases to $\Lambda = 210 \pm 14$ MeV for energies above the bottom quark mass of about 5 GeV.

QCD phase diagram

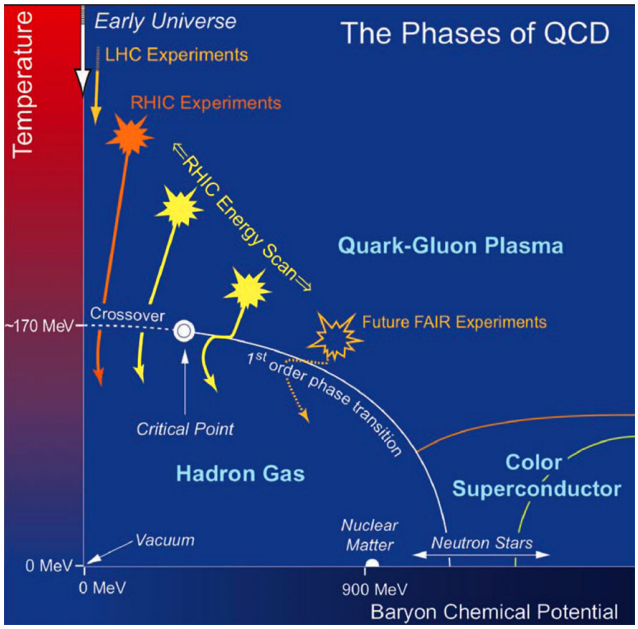

Figure 1.3: Schematic phase diagram of nuclear matter in terms of temperature (T) and baryonic chemical potential (μ_{B}) [45, 46].

Figure 1.3 shows a sketch of the QCD phase diagram, representing the transition from nuclear matter to hadronic gas to a phase where quarks and gluons are no longer confined. We describe matter with equal densities of quarks and antiquarks by setting μ_B to zero. This approximation holds good for heavy-ion collisions at mid-rapidity at RHIC, even better at the LHC, and exceptionally well in the early universe. A hadronic gas forms via a continuous crossover-type transition in these scenarios as the QGP expands and cools [15]. To study QGP with an excess of quarks over antiquarks, we examine the debris produced at very high rapidities in high-energy heavy-ion collisions. QGP forms from the compressed remnants of incident nuclei. Unfortunately, neither RHIC nor the LHC has detectors capable of these high rapidity measurements. Instead, scanning the QCD phase diagram in this region involves studying heavy-ion collisions with progressively lower energies, where the initial baryon number from incident nuclei contributes more to creating dense matter. Lower-energy nucleus-nucleus (A−A) collision studies have been conducted at the SPS and the RHIC BES, presenting intriguing early results. A second, higher-statistics phase of the BES program took place in 2019−2020, with extensions planned at the FAIR and the NICA facility for even lower collision energies, exploring higher μ_B (at medium to lower temperatures). Experimental programs aim to determine whether the continuous crossover between QGP and hadronic matter transforms into a first-order phase transition below a certain collision energy involving a nonzero critical value of μ_B. Several QCD models propose a critical point in the phase diagram [47]. Lattice techniques, in particular,

suggest a critical point at nonzero μ_B, but the "sign problem" limits its calculative power [48–51]. Increased non-gaussian fluctuations in RHIC collisions hint at critical fluctuations in the lower end of beam energy scan, though it is inconclusive due to limited statistics. The existence of a critical point at nonzero net-baryon chemical potential remains unknown, but upcoming data and analyses are expected to address this question soon. We anticipate waiting for the results from ongoing experimental programs to provide answers in the coming years.

1.3 Relativistic heavy-ion collisions

Heavy-ion collisions at ultra-relativistic energies offer a unique opportunity to recreate the QGP under laboratory conditions. These collisions produce high multiplicities of outgoing particles, resulting in event images of higher complexities than proton-proton collisions. At very high energies ($\sim$ TeV), the colliding nuclei are not stopped at the collision point. Instead, it results in a very low net-baryon density body, enabling the exploration of $\mu_B \approx 0$ region of the QCD phase diagram (also known as the Bjorken or transparency regime). In contrast, facilities like NICA use low energy collisions to focus on exploring the finite baryon-chemical potential region ($\mu_B \approx 200 - 500$ MeV) through fixed-target and collider experiments. The study of collision systems, particularly in heavy-ion collisions, involves understanding the number of nucleons involved. While direct measurements of quantities such as impact parameter (b), number of participating nucleons (N_{part}) and number of binary nucleon-nucleon collisions (N_{coll}) are challenging due to the small length scales involved, it is theoretically possible to estimate these quantities from experimental data. The most commonly applied technique is the "Glauber Model" technique, named after Roy Glauber (Nobel Prize in Physics, 2005). It utilizes quantum mechanical scattering theory to understand collision dynamics and accounts for multiple nucleon scatterings in the colliding matter. Glauber's pioneering work in this field established the groundwork to understand the non-trivial effects observed in proton-nucleus and nucleus-nucleus collisions at low energies [52].

1.3.1 The geometrical configuration

The Glauber Model offers a quantitative understanding of the geometrical arrangement of nuclei during collisions. It assumes that the baryon-baryon interaction cross-section remains constant as baryons pass through each other and that nuclei move in straight-line paths along the collision direction. This model helps simulate initial conditions in heavy-ion collisions by estimating the number of participating nucleons and binary collisions based on the impact parameter. The Glauber Model has two variants: the Optical approach and the Monte Carlo

approach; we focus here on the former. In the Optical approach, several assumptions are made, including the idea that at high energies, nucleons pass through each other undeflected, nucleons move independently within the nucleus, and the nucleus size greatly exceeds the range of the nucleon-nucleon force.

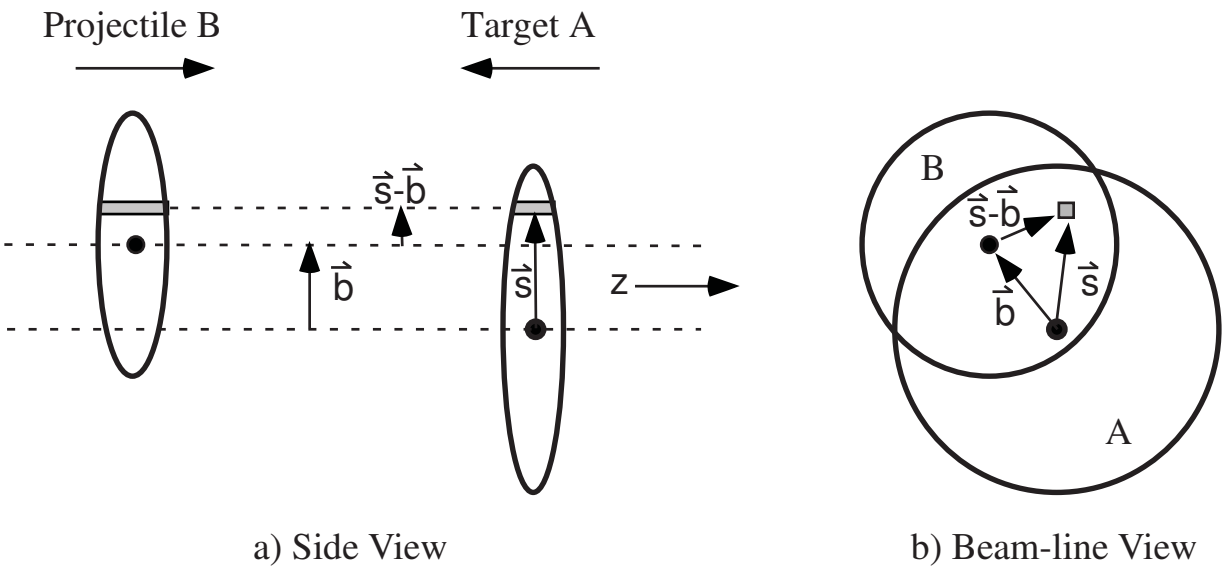

Figure 1.4: Schematic representation of the geometrical configuration of the target and projectile nuclei in the optical Glauber model, showing (a) transverse and (b) longitudinal views [52].

In the scenario depicted in Fig. 1.4, we are observing the interaction of two heavy-ions, referred to as "target" A (with A nucleons) and "projectile" B (with B nucleons), that are moving at relativistic speeds and collide at a specific impact parameter $\vec{b}$. Assume two flux tubes positioned at a displacement of $\vec{s}$ from the center of the target nucleus and a distance of $\vec{s}-\vec{b}$ from the center of the projectile. As a result of the collision, these tubes overlap. The probability per unit transverse area of a given nucleon being located in the target flux tube is

$$\hat{T}_A(\vec{s}) = \int \rho_A(\vec{s}, z_A) dz_A \quad , \tag{1.2}$$

where $\rho_A(\vec{s}, z_A)$ is the probability per unit volume, normalized to unity, for finding the nucleon at location $(\vec{s}, z_A)$. A similar expression follows for the projectile nucleon. Then the joint probability per unit area of nucleons being located in the respective overlapping target and projectile flux tubes of the differential area is $\hat{T}_A(\vec{s}) \cdot \hat{T}_B(\vec{s}-\vec{b})$. This product integrated over all values of $\vec{s}$ defines the "thickness function" $\hat{T}(\vec{b})$, with

$$\hat{T}_{AB} = \int \hat{T}_A(\vec{s}) \hat{T}_B(s \vec{-} b) d\vec{s} \tag{1.3}$$

Further the integral over all impact parameter for $\hat{T}_{AB}$ is given by

$$\int \hat{T}_{AB}(\vec{b})db = A \cdot B \quad , \tag{1.4}$$

since $\hat{T}_{AB}$ is purely a geometric factor, it is independent of the collision energy. The number of inelastic nucleon-nucleon collision as a function of the impact parameter is given as

$$N_{coll} = \hat{T}_{AB}(\vec{b})\sigma_{inel}^{NN} \quad , \tag{1.5}$$

where N_{coll} depends on the beam energy through σ_{inel}^{NN}. The probability of n inelastic nucleon-nucleon collisions between nucleus A and B at an impact parameter $\vec{b}$ is given by a binomial distribution,

$$P(n,\vec{b}) = \binom{AB}{n}\left[\frac{\hat{T}_{AB}(\vec{b})\sigma_{inel}^{NN}}{AB}\right]^n\left[1-\frac{\hat{T}_{AB}(\vec{b})\sigma_{inel}^{NN}}{AB}\right]^{AB-n} \quad , \tag{1.6}$$

where the first term is the number of combinations for finding n collisions out of total (AB) possible nucleon-nucleon interactions, and second term gives the probability for having exactly n collisions, and the last term is the probability of exactly $AB-n$ misses.
The number of participants in nucleus-nucleus collision can be obtained from a hadron-nucleon collision. So by setting $B=1$, the probability thus becomes

$$P(n,\vec{b}) = \binom{A}{n}\left[\frac{\hat{T}_{A}(\vec{b})\sigma_{inel}^{NN}}{A}\right]^n\left[1-\frac{\hat{T}_{A}(\vec{b})\sigma_{inel}^{NN}}{A}\right]^{A-n} \tag{1.7}$$

Summing over all probabilities, we obtain,

$$\sum_{n=1}^{A} P(n,\vec{b}) = 1-\left[1-\frac{\hat{T}_{A}(\vec{b})\sigma_{inel}^{NN}}{A}\right]^{A} \tag{1.8}$$

If $\hat{T}_A(\vec{b})\sigma_{inel}^{NN}/A \ll 1$ then the above sum can be approximated by exponential so that

$$\sum_{n=1}^{A} P(n,\vec{b}) = 1-exp[-\hat{T}_{A}(\vec{b})\sigma_{inel}^{NN}] \tag{1.9}$$

The number of participants in nucleus A is proportional to the nuclear profile function at transverse position $\vec{s}$, $\hat{T}_A(\vec{s})$, weighted by the sum over the probability for a nucleon-nucleus collision at transverse position $(\vec{b}-\vec{s})$ in nucleus B. Thus at a given $\vec{b}$, the N_{part} is given by

$$\begin{aligned} N_{part}(\vec{b}) = &\int \hat{T}_A(\vec{s})\Big(1-exp[-\hat{T}_B(b\vec{-}s)\sigma_{inel}^{NN}]\Big)d\vec{s} \\ &+\int \hat{T}_B(b\vec{-}s)\Big(1-exp[-\hat{T}_A(\vec{s})\sigma_{inel}^{NN}]\Big)d\vec{s} \end{aligned} \tag{1.10}$$

The model was employed to determine the N_{part} and N_{coll} as functions of the impact parameter for Au_{197} and Pb_{208} nuclei in Au−Au and Pb−Pb collisions, respectively, at RHIC ($\sqrt{s_{NN}}$ = 200 GeV) and LHC ($\sqrt{s_{NN}}$ = 2.76 TeV) energies. The values of σ_{inel}^{NN} used in the calculations are 42 mb for RHIC and 64 mb for LHC [52]. Fig. 1.5 illustrates that smaller impact parameters correspond to a larger overlap, indicative of central collisions, while larger impact parameters result in a smaller overlap, hinting at peripheral collisions. We draw An obvious conclusion that the number of participating nucleons and binary collisions decreases with increasing impact parameter values. Additionally, the number of binary nucleon-nucleon collisions increases with energy while the number of participating nucleons remains approximately the same.

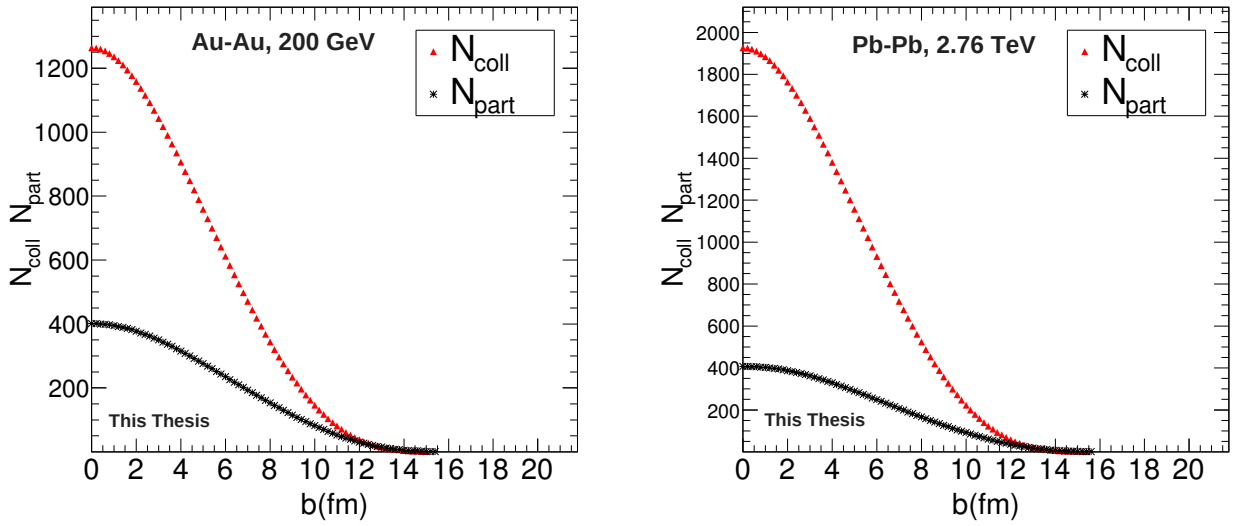

(a) (b)

Figure 1.5: N_{coll} (red) and N_{part} (black) as functions of impact parameter b calculated in the optical approximation for (a) Au−Au collisions at $\sqrt{s_{\rm NN}}$ = 200 GeV RHIC energy and for (b) Pb−Pb collisions at $\sqrt{s_{\rm NN}}$ = 2.76 TeV LHC energy.

1.3.2 The space-time evolution

Figure 1.6(a) presents a schematic representation of the space-time progression of a collision between two relativistic nuclei [53]. These nuclei, moving at speeds close to the light, collide and form a fireball; Fig. 1.6(b) depicts the hot matter in its various cooldown stages. This depiction of the space-time progression in relativistic heavy-ion collisions was first proposed by J. D. Bjorken in 1983, utilizing the concept in hydrodynamics [54]. The model simplifies the calculations by considering central collisions (zero impact parameter) between identical nuclei in their center-of-momentum frames. The chosen coordinates depict the nuclei moving towards each other along the z-direction (beam direction) and colliding at the origin at time $t = 0$.

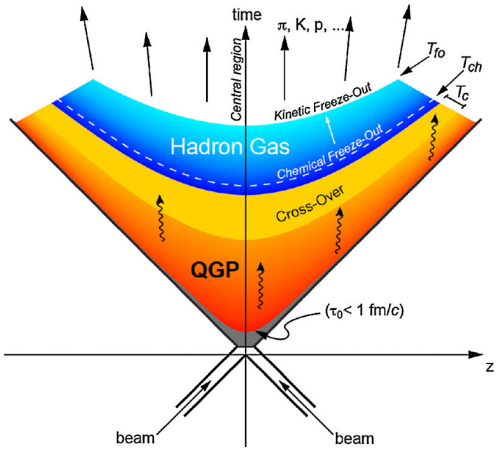

(a) Figure courtesy of Boris Hippolyte

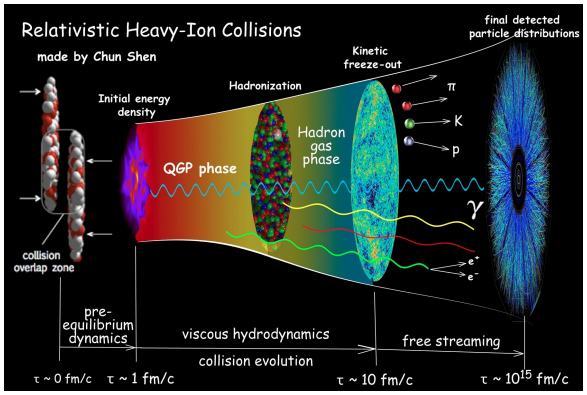

(b) Figure courtesy of Chun Sen

Figure 1.6: (a) Space-time diagram illustrating a heavy-ion collision between two nuclei at time $t = 0$ and longitudinal position $z = 0$ (transverse direction not shown). The fireball formed during the collision emits different particles (as indicated by the arrows). (b) Sketch depicting the time evolution of a relativistic heavy-ion collision as a function of proper time.

When the nuclei collide, they diverge, with the faster components (high-x partons[8]) moving forward, while the slower ones (low-x partons) lagging behind. This phenomenon leads to the generation of numerous virtual quanta in the mid-rapidity region. Over time, these quanta undergo decoherence, transitioning into fundamental particles. It is as if the nuclei pass through each other, creating a flat central area by freeing up colour strings. This central region initiates a longitudinal expansion once the interaction ends and the nuclei move apart. As the nuclei move at relativistic speeds, they undergo Lorentz contraction along the longitudinal direction by a factor of approximately $2R/\gamma$, where R is the nuclear radius and γ is the Lorentz factor. The curves in Fig. 1.6(a) represent hyperbolas of constant proper time ($\tau = t^2 - z^2$). Each hyperbola corresponds to a distinct stage in the space-time evolution of the system following the collision.

In the **pre-equilibrium phase** ($\tau \leq 1$ fm/c), the exact state of the colliding nuclei is unknown. However, any changes at this point significantly affect the production of final-state particles. The colliding nuclei here can be represented as a Glauber initial state [52], which is a collection of individual nucleons, or a colour glass condensate [55], which is a cohesive wall of gluons. Despite the chosen model, the impact parameter[9] of the nuclei and the fluctuations in the positions of the incoming partons result in an asymmetrical overlap region within the nuclei. When heavy ions collide, they create an intensely hot and dense medium composed of quasi-free quarks and gluons. This medium experiences temperature fluctuations in different

[8] x represents the Bjorken scaling variable, denoting the fraction of momentum carried by a parton within a hadron before the interaction. The value of x ranges from 0 to 1.

[9] The impact parameter in heavy-ion collisions represents the closest distance between the centers of the colliding nuclei. It determines the degree of overlap between the nuclei, affecting collision geometry and subsequent particle production.

regions until it reaches a state of local thermal equilibrium known as the quark-gluon plasma (**QGP phase**), after $\tau \sim 1$ fm/c[10]. It is generally described using a relativistic hydrodynamical formalism and is found to be an almost perfect fluid with a remarkably low shear viscosity to entropy density ratio. This QGP phase lasts for $\tau \sim 1 - 10$ fm/c, depending on the energy of collision [56].

As the medium undergoes expansion and cooling, it eventually reaches a density and temperature at which partonic interactions cease. This results in the formation of a hadron gas with fixed hadron fractions with the inelastic interactions between hadrons stopping completely, commonly referred to as **chemical freeze-out**. The temperature of the medium at this point in the collision's progression is denoted by T_{ch} [9, 57, 58]. As the medium further cools and expands, collisions between hadrons gradually halt, allowing them to achieve their final energies and momenta. This last phase is called **thermal or kinetic freeze-out**, which occurs at a lower temperature than chemical freeze-out and is denoted as T_{fo}. After this point, the hadrons freely stream towards the detectors. Understanding the properties of QCD matter at all of these phases can provide valuable insights into the fundamental nature of matter in the early universe.

1.4 Experimental signatures of QGP formation in heavy-ion collisions

To gain a thorough understanding of the properties of QGP, it is crucial to identify the signatures of its formation. While QGP is associated with several observables, relying on a single one does not provide a complete picture. Therefore, a combination of various measurements is necessary for comprehensive analysis. These signatures can be divided into two main categories: hard and soft, depending on the collision stage during which it is generated. Hard signatures result from the probes produced in the initial high-momentum partonic interactions. These signatures include heavy flavour (charmonium and bottomonium) states, jets, dileptons, and more. On the other hand, soft signatures encapsulate the bulk properties of the system pre- and post-hadronization, including parameters such as energy density, chemical and kinetic freeze-out temperatures, and manifestations of collective behaviour. Although this thesis does not explore all the signatures, the following subsection sheds light on some of the most common observables in brief.

[10] τ_0 denotes the QGP formation time.

1.4.1 Direct Photons

Direct photons are a collection of photons that are not produced from the decay of other particles in a heavy-ion collision. This makes them particularly valuable for studying the evolution of the QGP produced during these collisions. Because they only interact electromagnetically, direct photons have a much greater mean free path ($\sim 10^2 - 10^4$ fm) in strongly interacting media than the reaction volume ($\sim$ 1 fm). Additionally, they do not experience final state interactions like hadrons do [59]. This way, they serve as a direct probe of the initial stages of the collision. There are two types of direct photons: prompt photons, which result from initial hard parton scatterings, and thermal photons, which are produced during the QGP phase and the hadron gas phase. An increase in the emission of thermal photons is expected from a QGP, making them an important tool for investigating the properties of this fascinating state of matter. Studying direct photons can offer valuable insights into the temperature and thermal properties of the QGP. Specifically, thermal photons are highly sensitive to the QGP's temperature and their emission rate is directly linked to the system's temperature. This sensitivity dependence allows us to estimate the QGP's temperature during its various stages of evolution, thereby providing crucial details about its thermodynamic properties [60].

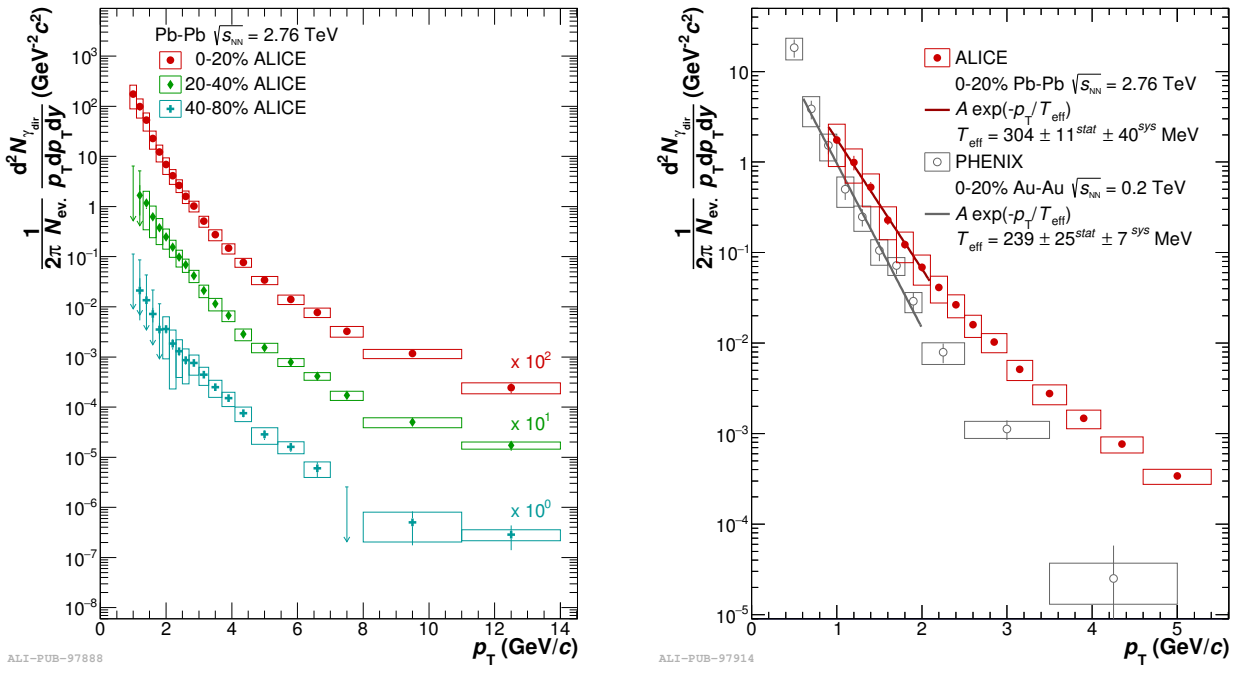

(a) (b)

Figure 1.7: (a): Direct photon spectra in Pb−Pb collisions at $\sqrt{s_{NN}}$ = 2.76 TeV for different centrality classes: 0−20% (scaled by a factor of 100), 20−40% (scaled by a factor of 10) and 40−80%. (b): Direct photon spectra in Pb−Pb collisions at $\sqrt{s_{NN}}$ = 2.76 TeV (ALICE at LHC) and Au−Au collisions at $\sqrt{s_{NN}}$ = 200 GeV (PHENIX at RHIC). The exponential function $Ae^{-p_T/T_{eff}}$ is employed for $p_T < 2.1$ GeV/c to estimate the average temperature of the produced medium.

Through analysis of data within a specific momentum range, an exponential fit function can determine the effective temperature (T_{eff}) for the medium's entire evolution[11]. In the 0−20% most central collisions of Pb−Pb collisions at $\sqrt{s_{NN}}$ = 2.76 TeV, the QGP generated has an effective temperature of $T_{\text{eff}} = (304 \pm 11^{\text{stat}} \pm 40^{\text{syst}})$ MeV. This value is derived from an exponential function fit to the direct photon spectrum, after subtracting the pQCD contribution, in the range $0.9 < p_{\text{T}}$ (GeV/c) < 2.1 [61]. Similarly, data from Au−Au collisions at $\sqrt{s_{NN}}$ = 200 GeV obtained by the PHENIX experiment at RHIC yield an effective temperature of $T_{\text{eff}} = (239 \pm 25^{\text{stat}} \pm 7^{\text{syst}})$ MeV [62]. Notably, the QGP produced in central Pb−Pb collisions at $\sqrt{s_{NN}}$ = 2.76 TeV at LHC has a temperature approximately 1.3 times higher than that of the QGP produced in Au−Au collisions at $\sqrt{s_{NN}}$ = 200 GeV at RHIC[12] in the same centrality class.

1.4.2 Elliptic flow

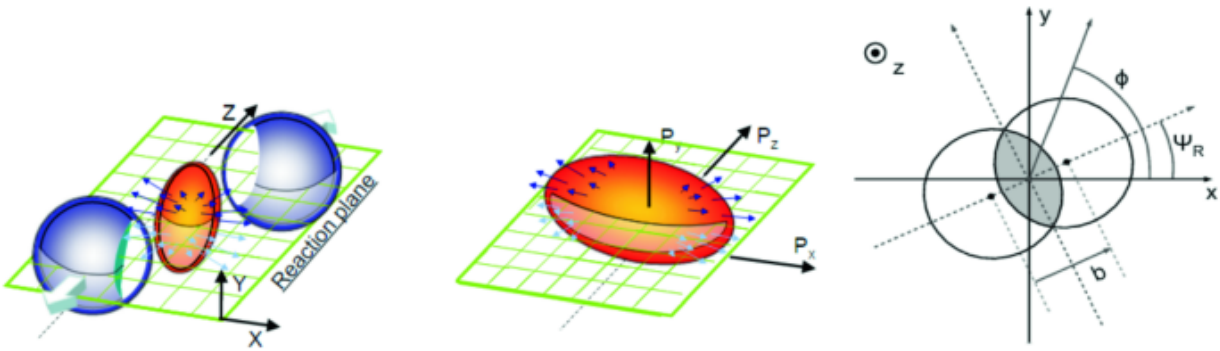

Figure 1.8: **Left:** A 3-D schematic representation depicting a non-central collision, highlighting the reaction plane, the almond-shaped interaction volume (yellow), and the spectator nucleons (blue) moving away in opposite directions. The coordinate system of the event is defined with the x-axis aligned with the impact parameter, the z-axis along the beam direction, and the y-axis completing the cartesian system. **Center:** Visualization of spatial anisotropy leading to momentum anisotropy within the collision system. **Right:** Diagram illustrating a non-central heavy-ion collision in the transverse plane (xy), with the beam axis (z-axis) perpendicular to the figure's plane. ϕ represents the azimuthal angle of one of the outgoing particles, Ψ_R denotes the angle of the reaction plane, and $\vec{b}$ signifies the impact parameter [63].

In non-central collisions where two identical spherical nuclei collide, the initial matter distribution is anisotropic, resembling an almond shape [63]. However, in experiments, the magnitude and orientation of the impact parameter vector vary from event to event and remain unknown. This initial geometry can impact the distribution of particles in the final state, particularly in the transverse plane. To effectively describe this geometry using a few parameters, the triple-differential invariant distribution of emitted particles in the final state is decomposed using

[11] The inverse slope parameter of the exponential trend in the data reflects the value of T_{eff}.

[12] The PHENIX experiment first reported a direct photon excess at $\sqrt{s_{NN}}$ = 200 GeV Au−Au collisions in 2010, which was later confirmed in 2015.

Fourier analysis to equation 1.11 [64]. This decomposition involves factors like particle transverse momentum (p_{T}), rapidity (y), azimuthal angle (ϕ) and the reaction plane angle (Ψ_R), with the reaction plane defined by the beam axis (z) and the impact parameter direction[13] (see Fig. 1.8).

$$E\frac{d^3N}{dp^3} = \frac{d^2N}{p_{\mathrm{T}}\ dp_{\mathrm{T}}\ dy}\frac{1}{2\pi} = \left(1 + \sum_{n=1}^{\infty} 2v_n(p_{\mathrm{T}}\ , y)cos[n(\phi - \Psi_R)]\right) \tag{1.11}$$

In general, the coefficients $v_n(p_{\mathrm{T}}\ , y) = \left\langle cos[n(\phi - \Psi_R)]\right\rangle$ vary with both p_{T} and y, hence called "differential flow". Integrated flow, on the other hand, is calculated by averaging differential flow using d^2N/dp_Tdy as a weight. The first coefficient, v_1, denotes directed flow, while the second coefficient, v_2, represents elliptic flow. Higher-order coefficients, such as v_3 and v_4, are known as triangular and quadrangular flow coefficients respectively.

$$v_n(p_{\mathrm{T}}\ , y) = \left\langle cos[n(\phi - \Psi_R)]\right\rangle = \frac{\int_0^{2\pi} d\phi cos[n(\phi - \Psi_R)]\frac{d^3N}{p_T dp_T dy d\phi}}{\int_0^{2\pi} d\phi \frac{d^3N}{p_T dp_T dy d\phi}} \tag{1.12}$$

In heavy-ion collisions, the area where two nuclei overlap creates a macroscopic medium that strongly interacts with its constituents, is in state of pressure anisotropy. This leads to spatial distortion in the particle distribution, with more particles originating from the shorter axis of the almond-shaped region due to higher pressure. As the system expands and evolves, the pressure gradients within the QGP result in an anisotropic flow pattern, with more particles emitted in the direction perpendicular to the impact plane. This phenomenon is called elliptic flow [65], which can be described by assuming a thermalized QGP that behaves like a viscous fluid following hydrodynamic equations. The magnitude of the ellipticity of the flow reflects the degree of thermalization and the viscosity of the QGP. Experimental observations of elliptic flow at RHIC [9] and the LHC [66] (Fig. 1.9(a)) provide a compelling evidence for the creation of the QGP and offer insights into its properties, such as viscosity and thermalization time. Thus, elliptic flow is a valuable probe for studying the properties and dynamics of the QGP formed in heavy-ion collisions.

In Fig. 1.9(b), the v_2 of electrons resulting from beauty hadron decays at midrapidity in Pb−Pb collisions at $\sqrt{s_{NN}}$ = 5.02 TeV in the 30-50% centrality class is shown. This measurement is important for understanding the thermalization of beauty quarks in the QGP. For the first time, a positive v_2 of electrons from beauty hadron decays is observed within the 1.3 $< p_{\mathrm{T}}$ (GeV/c) $<$ 6 range, with a significance of 3.75σ. It is noteworthy that no significant p_{T} dependence of the v_2 is observed. To understand the contribution of beauty quark thermal-

[13]The sine terms, $sin[n(\phi - \Psi_R)]$, are omitted from Eqn. 1.11 as they vanish due to the reflection symmetry relative to the reaction plane.

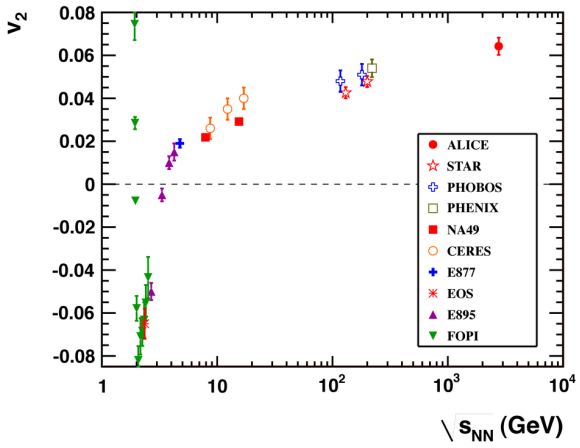

(a) Comparison of integrated elliptic flow at 2.76 TeV in Pb–Pb collisions within the 20–30% centrality class with results obtained at lower energies for similar centralities reveals an approximately 30% increase from $\sqrt{s_{NN}}$ = 200 GeV to 2.76 TeV.

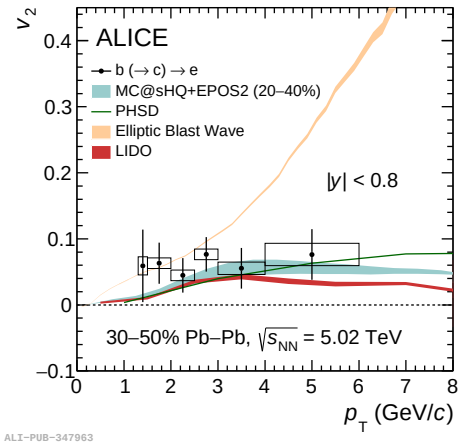

(b) Elliptic flow of electrons from beauty-hadron decays measured by ALICE in 30−50% centrality Pb−Pb collisions at $\sqrt{s_{NN}}$ = 5.02 TeV at midrapidity, compared with model calculations

Figure 1.9: Elliptic flow measured by ALICE in Pb−Pb collisions at $\sqrt{s_{\mathrm{NN}}}$ = 2.76 and 5.02 TeV, respectively [66, 67].

ization to the non-zero positive v_2, the measurement is compared against various models, such as MC@sHQ+EPOS2, PHSD, and LIDO, which employ different approaches to characterizing beauty quark interactions with a hydrodynamically expanding medium [67]. This measurement provides new insights and constraints on theoretical models regarding beauty quark dynamics within the QGP.

1.4.3 Nuclear modification factor

The nuclear modification factor (R_{AA}) is a key observable in studying heavy-ion collisions. It quantifies the suppression or enhancement of particle production in heavy-ion collisions relative to proton-proton collisions scaled by the average number of binary nucleon-nucleon collisions. The R_{AA} is calculated as the ratio of the p_{T} -differential particle yields in nucleus-nucleus (A−A) collisions ($\mathrm{d}N_{\mathrm{AA}}/\mathrm{d}p_{\mathrm{T}}$) to the corresponding production cross-section in pp collisions ($\mathrm{d}\sigma_{\mathrm{pp}}/\mathrm{d}p_{\mathrm{T}}$) at the same energy, normalized by the average nuclear overlap function $\langle T_{\mathrm{AA}} \rangle$ for the studied centrality range [68]. $\langle T_{AA} \rangle$ is obtained through Glauber model calculations, considering detector responses in centrality measurements [69, 70].

$$R_{\mathrm{AA}} = \frac{1}{\langle T_{\mathrm{AA}} \rangle} \frac{\mathrm{d}N_{\mathrm{AA}}/\mathrm{d}p_{\mathrm{T}}}{\mathrm{d}\sigma_{\mathrm{pp}}/\mathrm{d}p_{\mathrm{T}}} \tag{1.13}$$

In heavy-ion collisions, high-p_{T} particles mainly originate from the initial hard scattering. If heavy-ion collisions were simply a superposition of an equal number of nucleons colliding,

then the nuclear modification factor would be unity ($R_{AA} = 1$). This implies that the number of high-p_{T} particles produced would match the equivalent number obtained in proton-proton collisions, scaled by the number of binary collisions in the heavy-ion collision scenario. When high-energy partons pass through the QGP medium, they lose energy through jet quenching, suppressing high-p_{T} particles in heavy-ion collisions compared to proton-proton collisions. This manifests as an $R_{AA} < 1$ at high-p_{T} . The suppression in R_{AA} directly results from parton energy loss mechanisms like gluon radiation and elastic scattering, which occur in the dense QGP medium. The magnitude of suppression offers valuable insights into the density, temperature, and transport properties of the QGP[14]. The significant suppression of high-p_{T} particles observed in heavy-ion collisions at RHIC and the LHC, where $R_{AA} < 1$, agrees with theoretical predictions based on QGP formation. This agreement between theory and experimental observations strengthens the interpretation of the nuclear modification factor as a telling signature of QGP formation.

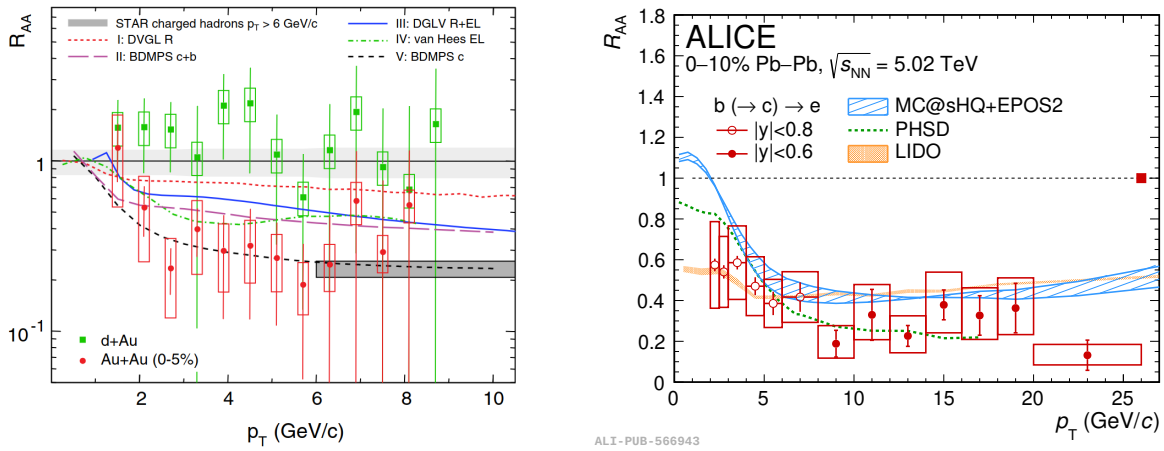

(a) d–Au and Au–Au at $\sqrt{s_{NN}} = 200$ GeV

(b) Pb–Pb at $\sqrt{s_{NN}} = 5.02$ TeV

Figure 1.10: The nuclear modification factor of electrons from (a) heavy-flavour and (b) beauty-hadron decays in the most central collisions compared with predictions from several theoretical calculations [27, 71].

1.4.4 Jet quenching

When partons undergo hard scattering with large momentum transfers, they generate high-momentum collimated showers of lighter hadronic particles, forming a jet. However, in the presence of a dense QGP, these energetic partons lose energy as they traverse the medium due to various QCD energy-loss mechanisms [72]. This phenomenon is called jet quenching, and it becomes particularly prominent when partons that would typically form back-to-back di-jets

[14] R_{AA} is smaller in central events compared to peripheral events because of the greater average suppression resulting from the larger QGP formed in central collisions.

traverse the QGP, especially in central collisions where the volume of QGP is high. If one parton escapes the QGP while the other travels through it, losing energy to the medium, the latter may lose so much energy that it no longer appears as a jet but rather as an increased number of softer hadrons. This asymmetry arises because one parton traverses more medium, experiencing greater energy loss through gluon radiation, resulting in the suppression or complete absorption of one jet. The discovery of jet quenching at RHIC [73], motivated by the measurement of the R_{AA} factor, has provided valuable insights into the behaviour of high-energy partons in a strongly interacting QGP. Experimental findings, such as the disappearance of the "away-side" peak in two-particle azimuthal correlations in central Au−Au collisions at RHIC [9, 73], support this phenomenon. Similar observations have been made at the LHC by ALICE, ATLAS, and CMS experiments, providing compelling evidence for jet quenching as a key signature of the QGP.

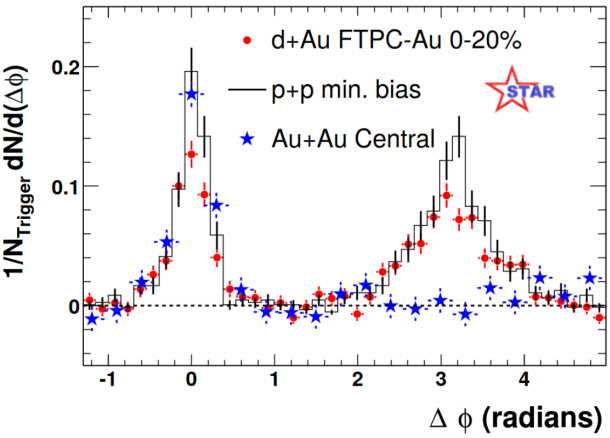

(a) Dihadron azimuthal correlations of hadrons with $p_{\mathrm{T}} > 2$ GeV/c relative to a trigger hadron with $p_{\mathrm{T}}^{\mathrm{trig}} > 4$ GeV/c for minimum bias pp (black line), central d−Au (red circle), and central Au−Au (blue star) collisions measured using STAR data.

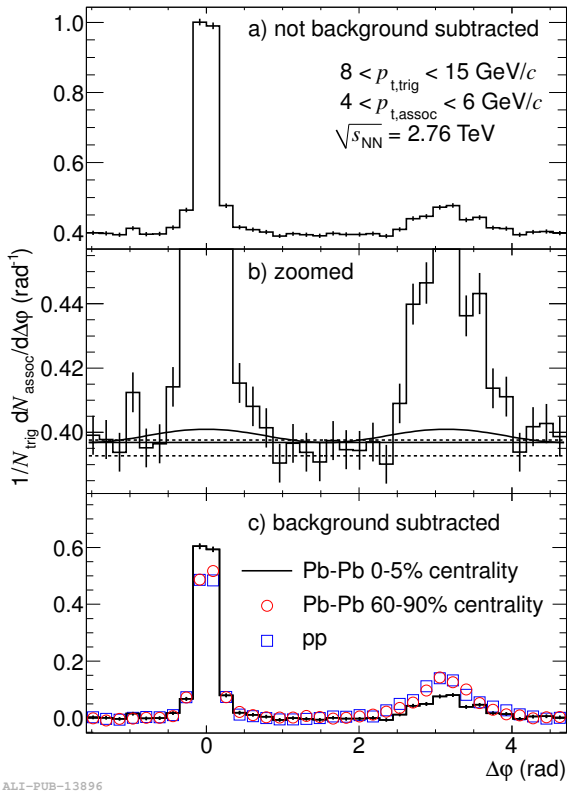

(b) Corrected per-trigger pair yield for central Pb−Pb events (black line), peripheral Pb−Pb events (red circle), and pp events (blue square). (a) Azimuthal correlation; (b) Zoom on the region where the pedestal values (horizontal lines) and the v_2 component are indicated. (c) Background-subtracted distributions.

Figure 1.11: Observations of jet quenching reported by the STAR experiment at RHIC (Left) and the ALICE experiment at the LHC (Right). Error bars represent statistical uncertainties only [9, 74].

1.4.5 Quarkonium suppression

Quarkonia, which are the bound states of $c\bar{c}$ (J/ψ) and $b\bar{b}$ (Υ), serve as a valuable probe for investigating the properties of the QGP. T. Matsui and H. Satz initially proposed that the suppression of J/ψ production in heavy-ion collisions is an important indicator of the deconfinement [75]. Debye screening effects in the QGP dissolve bound states with a large radius relative to the Debye radius (r_D)[15]. As $c\bar{c}$ states are predominantly formed during the early collision stages due to the substantial mass of the c quark compared to u, d, and s quarks. The presence of QGP, coupled with sufficiently high temperatures, leads to a noticeable suppression in the final state hadron spectra of $c\bar{c}$, while disassociated charm quarks enhance the open charm production (e.g., D^0, $D^{\pm}$). J/ψ suppression has been confirmed at the SPS [76] and at RHIC [77], with comparable suppression levels. Interestingly, measurements at the LHC [78] indicate less suppression; various models have been proposed to explain this apparent J/ψ yield enhancement, including considerations of the recombination of deconfined charm quarks during the hadronization process [79–81].

1.4.6 Strangeness enhancement

Enhanced production of s quarks compared to u and d quarks in heavy-ion collisions, compared to proton-proton collisions, is one of the oldest suggested signatures of QGP formation [82]. Since the colliding nuclei do not contain any strange quarks, all the detected strangeness must be created during the collision. The concept of strangeness enhancement relies on the distinct mechanisms and production rates of strange particles in a hadron gas and a QGP. In a hadron gas system without QGP formation, strange hadrons are produced through re-scattering within the expanding hadron gas system. Since strangeness is conserved, each strange particle produced must be balanced by an anti-strange particle. Consequently, the threshold for producing strange hadrons from inelastic collisions, which is above 1 GeV, is relatively high. However, in the QGP phase, quarks and gluons exist freely, lowering the quark-antiquark pair production threshold. The increased gluon density within the QGP system amplifies the cross-section for strange quark production through gluon fusion ($gg \rightarrow s\bar{s}$) in the QGP [83]. The Q value for creating the $s\bar{s}$ pair is reduced to $\sim$ 200 MeV, a value lesser than T_C. Thus, strangeness production is significantly enhanced within QGP where $T > T_C$. If strange quarks survive hadronization without re-annihilating, the abundance of strangeness in the pre-hadronic state should be reflected in the observed relative hadron yields. Owing to the increase in QGP vol-

[15]The presence of a dense and hot QGP medium screens the colour charges of charm and anticharm quarks within the J/ψ. The characteristic distance over which colour charges are screened is represented by r_D. As the temperature of the QGP rises, the r_D decreases, leading to stronger colour charge screening. Ultimately, the J/ψ dissociates into its constituent quarks due to the weakening of the colour force caused by screening.

ume. Consequently, the abundance of s quarks increases, which combines with other quarks to create hyperons, thereby increasing the number of strange hadrons (particularly multi-strange hyperons) detected compared to situations with no QGP formation. Strangeness production is also expected to increase as we move from pp collisions to heavy-ion collisions.

However, recent findings from the ALICE collaboration reveal that the production rates of strange hadrons in high-multiplicity pp collisions are on par with those observed in Pb-Pb collisions [18]. This similarity raises questions about whether the strangeness enhancement detected in high-multiplicity pp events arises from analogous underlying mechanisms governing the physics of diverse colliding systems, thereby becoming comparable once a specific multiplicity class of events is considered.

1.4.7 Event-by-event fluctuations

Phase transitions often involve significant possibilities of fluctuations. When transitioning from ordinary hadronic matter to the QGP phase (or vice versa), there may be non-statistical fluctuations in particle multiplicities, ratios, and transverse momenta that can potentially be detected through final state measurements analyzed on an event-by-event basis [84]. At RHIC and LHC energies, where there is a high number of produced particles, ample statistical data is available per event for such analyses. The idea of event-by-event net charge fluctuations as a signature of QGP is not directly tied to the phase transition itself but is more about the distribution of electric charge within the QGP. Quarks carry fractional charges $\left(\pm\frac{1}{3}\text{ or }\pm\frac{2}{3}\right)$ units, which contrast with the more concentrated charge distribution in the ordinary hadronic matter. It's suggested that this distinct charge distribution in the QGP could persist even after the phase transition back to hadronic matter [85, 86]. A detailed discussion on this signature will be provided in Chapter 2.

1.5 Theoretical framework and model calculation

While various theoretical models are available to predict outcomes in heavy-ion collisions, this thesis focuses solely on reporting results from proton-proton collisions. The predictions from the widely used model 'FONLL', based on pQCD calculations, is used to compare results from electrons from beauty-hadron decays observed in pp collisions [87, 88]. Other pQCD models, such as the General-Mass Variable-Flavor-Number Scheme (GM-VFNS) [89] and k_T-Factorization [90, 91], which utilise the factorisation approach, also exist. However, these models are beyond the scope of this thesis, and our discussions will focus mainly on FONLL. FONLL stands for "Fixed Order Next-to-Leading Logarithm", a theoretical framework that

plays a crucial role in analysing heavy-flavor spectrum measurements in high-energy collisions. It combines fixed-order perturbation theory calculations with the resummation of large logarithmic corrections at next-to-leading logarithmic accuracy to compute the production rates and energy distributions of heavy-flavour particles. These corrections, involving terms like $\alpha_s^n \log^n(p_{\mathrm{T}}\ /m)$ and $\alpha_s^n \log^{n-1}(p_{\mathrm{T}}\ /m)$, are critical in capturing the complex dynamics of heavy-flavour production, particularly at high energies where such logarithmic corrections are more pronounced [88]. To predict leptons originating from decays of heavy-flavour hadrons, the theoretical cross-section for heavy quarks derived from pQCD is convoluted with a fragmentation function ($D^{NP}_{Q\to H_Q}$) and decay function ($g^{weak}_{HQ\to\ell}$) as indicated by equation 1.14.

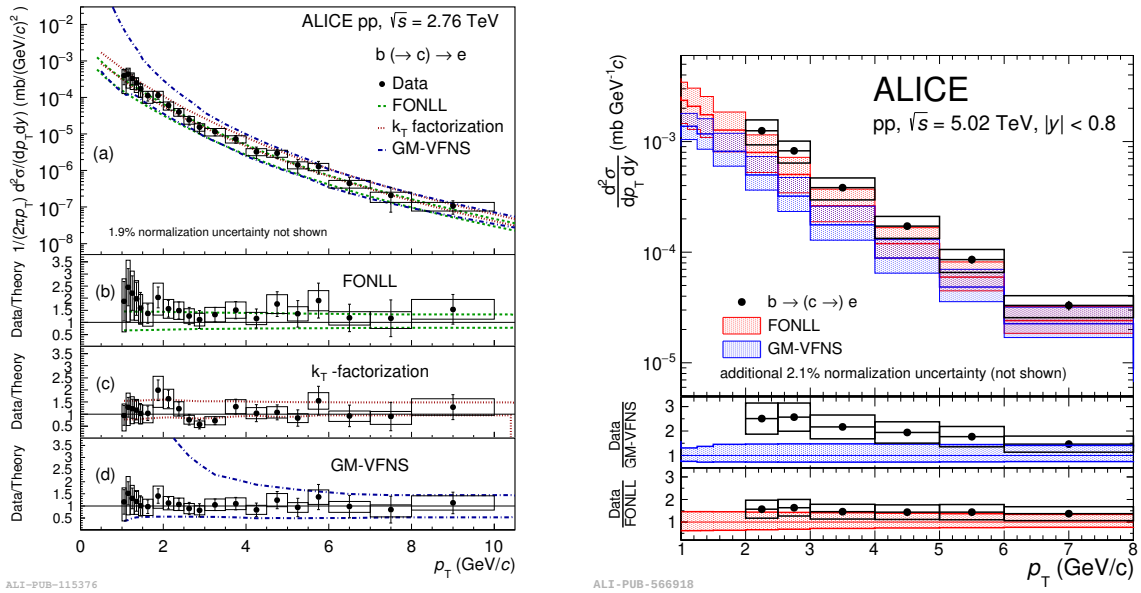

(a) (b)

Figure 1.12: p_{T} -differential cross-section of electrons from beauty-hadron decays in proton-proton collisions at $\sqrt{s}\ = 2.76$ TeV (a) and $\sqrt{s}\ = 5.02$ TeV (b) compared with model predictions. The bottom panels show the ratios of data to the models, respectively [27, 92].

$$d\sigma_\ell^{FONLL} = d\sigma_Q^{FONLL} \otimes D^{NP}_{Q\to H_Q} \otimes g^{weak}_{HQ\to\ell} \tag{1.14}$$

The fragmentation fraction $f(Q \to H_Q)$ is determined by integrating $D^{NP}_{Q\to H_Q}$ for a specific heavy-flavored hadron H_Q. These parameters are determined from e^+e^- collision data, while the decay functions are taken from the experimental data. In addition, the weak decay spectra $g^{weak}_{HQ\to\ell}$ and the branching ratios are also extracted from the experimental data. This comprehensive integration enables a more accurate description of the heavy-flavour production processes, especially at high energies where the logarithmic corrections become significant. The central FONLL prediction is calculated by setting the renormalization and factorization scales equal to the transverse mass, where $\mu_{R,F} = \mu_0 = \sqrt{p_{\mathrm{T}}{}^2 + m^2}$ (m_T), with m being the heavy

quark mass and p_{T} the transverse momentum. The theoretical uncertainty is determined by considering variations in factorization and renormalization scales, heavy quark mass, and uncertainties related to Parton Distribution Functions (PDFs), with these uncertainties combined using the quadrature approach.

In the past, FONLL calculations have successfully reproduced experimental data in the heavy-flavour sector across various experiments, including those conducted by ALICE. For example, they have accurately reproduced the p_{T} -differential cross-section of the non-prompt D meson spectrum measured by ALICE in both $\sqrt{s}$ = 5.02 and $\sqrt{s}$ = 13 TeV pp collisions [93, 94]. Furthermore, these predictions exhibit consistency with ALICE data in measurements of beauty-hadron decay electrons in pp collisions at different energies like 2.76, 5.02, 7, and 13 TeV [27, 92, 95, 96]. In this thesis, FONLL is also used to extend the pp reference measurement to higher momenta, which is important to note as no experimental data are available at these higher momenta. In short, the decision to use FONLL was based on its reliable agreement with pp results from data, as elaborated in detail in subsection 4.5.1(c).

Chapter 2

Diffusion coefficients of identified particles using ν_{dyn} variable at RHIC energies

2.1 Introduction

One of the major goals of heavy-ion experiments is to study the phase transition from hadronic matter to QGP. Event-by-event fluctuation of conserved quantities such as net-baryon number, net-electric charge, and net strangeness were proposed as possible signals of the QCD phase transition [85]. Measurements of fluctuations can also help in understanding the nature of such a phase transition. One of the observables, net-charge fluctuation, has been considered as a signal for such studies. The reason behind net-charge fluctuation study is similar to the original study of color charge in e^+e^- experiment. There the color charge ratio was measured and depending upon the difference in fundamental degrees of freedom between quark-gluon state and hadronic state, the origin of the color charge was determined [86, 97]. Several experiments have measured net-charge fluctuation at SPS, RHIC, and LHC energies [98–104].

Event-by-event fluctuations in high-energy heavy-ion collisions have been used to study the equilibrium of thermodynamical fluctuations at freeze-out. In the QGP phase, quarks are the charge carriers with a fractional charge of $\pm 1/3$ or $\pm 2/3$, while in the hadronic phase hadrons are the charge carriers each with an integer charge. Hence, net-charge fluctuations in the QGP phase are predicted to be a factor of 2 to 3 smaller as compared to that of the hadronic phase [85]. These differences may be considered as indicators of the formation of quark-gluon plasma in high energy heavy-ion collisions. Thus, the net-charge fluctuations are strongly dependent on the phase of their origin. Due to the rapid expansion of the fireball

created in the heavy ion collisions, the fluctuations created in the initial state may survive during the hadronization process [86]. If the relaxation time happens to be shorter than the lifetime of the hadronic stage of the collisions, then the values of such fluctuations should deviate from their equilibrium hadron gas values towards their earlier, primordial values, typical for QGP [85, 86]. The fluctuations of different lengths or ranges in rapidity space relax on different time scales. Since relaxation can only proceed via diffusion of the charge, the longer range of fluctuations relaxes gradually. The relaxation time is expected to grow as a square of the rapidity range [105]. It is evident that fluctuations of the total charge in a wider rapidity window relax slower. The minimal rapidity window that one can consider must be larger than the mean rapidity change of a charged particle in a collision, δy_{coll}. It is observed that the typical δy_{coll} for the baryon and the electric charge is around 0.2 and 0.8, respectively [105].

The BES program at RHIC has been initiated to explore the QCD phase diagram and study the transport properties of nuclear matter at finite temperature (T) and baryonic chemical potential (μ_B). At lower collision energy, e.g., $\sqrt{s_{NN}} = 7.7$ GeV, the baryon chemical potential can reach up to $\mu_B \sim 400$ MeV, which is significant compared to the temperature of the fireball. At such energies, strong gradients in the chemical potential of conserved charges are expected. Hence, the lower beam energy scan program at RHIC will be useful to explore the properties of net-charge diffusion in nuclear matter. However, it is important to mention that the role of baryon stopping and long range correlations need to be explored extensively before making any conclusion on diffusion coefficients.

The conservation laws limit the dissipation of the fluctuations after the hadronization has occurred. It is observed that, due to the diffusion of particles in rapidity space, these fluctuations may also get diluted in the expanding medium [105, 106]. The hadronic diffusion from the time of hadronization τ_0 to a freeze-out time τ_f can dissipate these fluctuations. It is argued that the reduction of the fluctuations in the QGP phase might be observed only if the fluctuations are measured over a large rapidity range [105]. The work also quantifies the reduction of fluctuations with the increase of accepted rapidity interval. The suppression of charge fluctuations observed in the experimental data is consistent with the diffusion estimates [107]. Earlier efforts were made to estimate the fluctuation strength using a transport model for all inclusive charged particles [108]. However, the contribution of different identified particles towards dilution of the measured fluctuation strength may be different.

In the present study, we have calculated the fluctuation strength of identified charged particles, mainly for net-pion, net-kaon and net-proton using hadron resonance gas model (HRG), the heavy-ion jet interaction generator (HIJING) model, and the transport model ultrarelativistic quantum molecular dynamics (UrQMD) which will provide the reference for the behavior

of fluctuations measured in the experiments. Additionally, we have computed the diffusion coefficient of identified charged particles, mainly for net-pion, net-kaon, and net-proton using a transport model UrQMD, and HIJING model which will serve as the baseline for experimental measurement.

This chapter is structured as follows. The subsequent section outlines the formalism employed for computing the fluctuation strength. In Sec. 2.3, we discuss the HRG model utilized in this study, along with the implementation of resonance decay. The HIJING and UrQMD models are also briefly covered within the same section. In Sec. 2.4, we present our derived outcomes concerning $\nu_{(\pm,\mathrm{dyn})}$ and diffusion coefficients for identified particles at varying $\Delta\eta$ and $\sqrt{s_{NN}}$. In Sect. 2.5, we finally summarize our findings.

2.2 Measures

The collisional volume can not be directly measured in heavy ion experiments, therefore the ratios of number of positive (N_+) and number of negative (N_-) charged particles normalized by total number of charged particles under consideration for a fixed centrality class of events is used to measure fluctuation strength. This quantity is usually known as D measure [109] and defined as

$$\begin{aligned} D = \langle N_{\mathrm{ch}}\rangle\langle\delta R^2\rangle &= \frac{4}{\langle N_{\mathrm{ch}}\rangle}\langle\delta N_+^2 + \delta N_-^2 - 2\delta N_+\delta N_-\rangle \\ &\approx \frac{4\langle\delta Q^2\rangle}{\langle N_{\mathrm{ch}}\rangle}, \end{aligned} \tag{2.1}$$

where $R(= N_+/N_-)$ is the ratio of number of positive particles to the number of negative particles, $Q = N_+ - N_-$ is the difference between the number of positive and negative particles (net-charge) and $\langle N_{\mathrm{ch}}\rangle = \langle N_+ + N_-\rangle$ is the average number of charged particles measured within the experimental acceptance. The $\langle\delta Q^2\rangle$ is the variance of the net-charge Q, which is proportional to the net-charge fluctuation in the system. The value of D is predicted to be approximately four times smaller in the QGP phase as compared to the hadron gas phase [109]. However, the D measure has been found to be dependent on detection efficiency [98].

Another variable, $\nu_{(\pm,\mathrm{dyn})}$, is used to measure the fluctuation strength, which is robust and independent of detection efficiency. It is defined as

$$\nu_{(\pm,\mathrm{dyn})} = \frac{\langle N_+(N_+-1)\rangle}{\langle N_+\rangle^2} + \frac{\langle N_-(N_--1)\rangle}{\langle N_-\rangle^2} - 2\frac{\langle N_-N_+\rangle}{\langle N_-\rangle\langle N_+\rangle}. \tag{2.2}$$

The value of $\nu_{(\pm,\mathrm{dyn})}$ gives the measure of the relative correlation strength of ("++," "−−,"

and "+−") charged particle pairs. The relation between D and $\nu_{(\pm,\mathrm{dyn})}$ is given as [109]

$$\langle N_{\mathrm{ch}}\rangle\nu_{(\pm,\mathrm{dyn})} \approx D - 4. \tag{2.3}$$

It is found that global charge conservation has a finite effect on the fluctuation variable $\nu_{(\pm,\mathrm{dyn})}$ [110, 111]. However, we have refrained from applying these corrections to our estimated values. One of the important aspects of this measured fluctuation strength is its survival probability. At high energy, i.e., in the limit $\langle N_+\rangle = \langle N_-\rangle$, the magnitude of $\nu_{(\pm,\mathrm{dyn})}$ is determined by the integral of the balance function in the acceptance of the measurement [110]. This integral depends on the relative width of the acceptance as well as the width of the balance function. The diffusion can further affect the value, but the magnitudes of $\nu_{(\pm,\mathrm{dyn})}$ are mainly determined by the $1/N_{\mathrm{ch}}$ effect and charge conservation. Thus it is suggested to measure the fluctuation strength over large rapidity space which allows us to see deeper back into the history of the collision [105].

2.3 Estimation of ν_{dyn} in different models

In this section, we briefly describe the models used in the calculation of ν_{dyn}, which captures the strength of the correlations. These models are extensively used to explain the experimental data from heavy-ion collisions.

2.3.1 Hadron resonance gas model

The partition function the in HRG model has all relevant degrees of freedom of the confined, strongly interacting matter and implicitly includes all the interactions that result in resonance formation [112, 113]. In the ambit of the grand canonical ensemble, the logarithm of the partition function is given as

$$\ln Z_i(T, V, \mu_i) = \pm\frac{V g_i}{(2\pi)^3}\int d^3p\, \ln\{1 \pm \exp[(\mu_i - E)/T]\}, \tag{2.4}$$

where i is the particle number index, V is the volume of the system, g_i is the degeneracy factor for the ith particle, $\pm ve$ signs correspond to the baryon or meson, respectively. We have used the total chemical potential of individual particle μ_i in our calculations as given in Ref. [112]. Using the partition function, one can calculate various thermodynamical quantities of the system in heavy-ion collisions. The susceptibilities of different orders are related to the $\langle N_{\mathrm{ch}}\rangle$ and $\langle \delta Q^2\rangle$ representing mean and variance of individual particle, respectively. These quantities can be calculated by taking the first and second derivative of Eq.(2.4) with respect

to μ:

$$\langle N_{\rm ch}\rangle = \pm\frac{g_i}{2\pi^2}\int \frac{d^3p}{\{1\pm\exp[(\mu_i - E)/T]\}}, \tag{2.5}$$

$$\langle \delta Q^2\rangle = -\frac{g_i}{2\pi^2}\int \frac{d^3p}{T}\frac{\pm\exp[(\mu_i - E)/T]}{\{1\pm\exp[(\mu_i - E)/T]\}}, \tag{2.6}$$

Equations (2.5) and (2.6) are used to calculate ν_{dyn} in HRG model.

Experimentally measured stable particles (pions, kaons and protons along with their anti-particles) have contributions from the production of both primordial as well as from resonance decay. Further, neutral resonances introduce positive correlations between N_+ and N_- and hence, their decay daughters can affect the fluctuation of the final measured particles. The ensemble averaged stable particle yield will have contributions from both primordial production and the resonance decays [97, 114],

$$\langle N_i\rangle = \langle N_i^*\rangle + \sum_R \langle N_R\rangle\langle n_i\rangle_R \tag{2.7}$$

where $\langle N_i^*\rangle$ and $\langle N_R\rangle$ correspond to the average primordial yield of particle species i and of the resonances R, respectively. The summation runs over all the resonances which decay to the final particle i with $\langle n_i\rangle_R = \sum_r b_r^R n_{i,r}^R$ being the average number of particle type i produced from the resonance R. Further, b_r^R is the branching ratio of the rth decay channel of the resonance R and $n_{i,r}^R$ is the number of particle i produced in that decay branch. The generalized nth order susceptibility for stable particle i can be written as [115]

$$\chi_i^{(n)} = \chi_i^{*(n)} + \sum_R \chi_R^{(n)}\langle n_i\rangle_R^n \tag{2.8}$$

The first term in Eq.(2.8) corresponds to the contribution from primordial yield and the second term corresponds to the contribution from the fluctuation of primordial resonances and the average number of produced particle of type i, assuming the number of decay daughters is fixed.

2.3.2 The HIJING and UrQMD models

We have used HIJING (V.1.37) and UrQMD (V.1.30) to study the fluctuation variable ν_{dyn}. Both HIJING and UrQMD models are Monte Carlo event generators used for nucleon-nucleon and nucleus-nucleus collisions in high energy physics simulations. These models provide a baseline to compare with the experimental data.

The HIJING model is based on pQCD considering that the multiple mini-jet partons produced in collisions are transformed into string fragments and later, fragments into hadrons. It uses the PYTHIA model to generate kinetic variables for each hard scattering and the JETSET model for jet fragmentation. In pQCD, the cross section for hard parton scattering is determined using the leading order to account for the higher-order corrections. The soft contributions are determined using the diquark-quark strings with gluon kinks induced by soft gluon radiation. The HIJING model considers the nucleus-nucleus collisions as a superposition of nucleon-nucleon collisions; it also takes into account other physics processes like multiple scattering, jet quenching, and nuclear shadowing to study the nuclear effects [20].

The UrQMD model considers the microscopic transport of quarks and diquarks with mesonic and baryonic degrees of freedom. The model preserves the conservation of baryon number, electric charge, and strangeness number. In this model, the space-time evolution of the fireball is studied in terms of excitation and fragmentation of color strings, and the formation and decay of hadronic resonances [111]. Interaction of the produced particles, which may influence the acceptance of certain windows, is included in the model. The formation of hadrons is explained by color string fragmentation, it also considers the resonance decays, multiple scattering between hadrons during the evolution including baryon stopping phenomena, which is one of the features of heavy-ion collisions especially at lower collision energies [21]. The UrQMD model has been applied successfully to study the thermalization [116], particle yields [117, 118], leptonic and photonic probes [119], and event-by-event fluctuations [120–125].

It is noteworthy to mention that the measured values of fluctuation strength (ν_{dyn}) shall depend on the width of the acceptance, on the primordial mechanisms leading to $+ve$ and $-ve$ particle production, radial transport (flow), diffusion, etc. HIJING and UrQMD models do not account for such effects explicitly.

2.4 Results and discussion

The measured fluctuations may get diluted in the expanding medium due to the diffusion of the charged hadrons in the rapidity space [106]. The dissipation of fluctuations occurs during the evolution of the system from hadronization to their kinetic freeze-out. Hence, the experimental measurements of not only the magnitudes of fluctuation quantities at a fixed $\Delta\eta$ but also their dependence on $\Delta\eta$ enable us to explore various aspect of the time evolution of the hot medium and the hadronization mechanism. It is proposed to study the fluctuations of identified particle species and estimate the rate of diffusion in different rapidity interval for the measured particles at various centre of mass energies ($\sqrt{s_{NN}}$) available at BNL (RHIC).

Measurements of the net-kaon and net-proton fluctuations are of particular interest as they address respectively fluctuations of net-strangeness and net-baryon number, which might be more sensitive to the details of the collision process. Figure 2.1 shows the estimated value

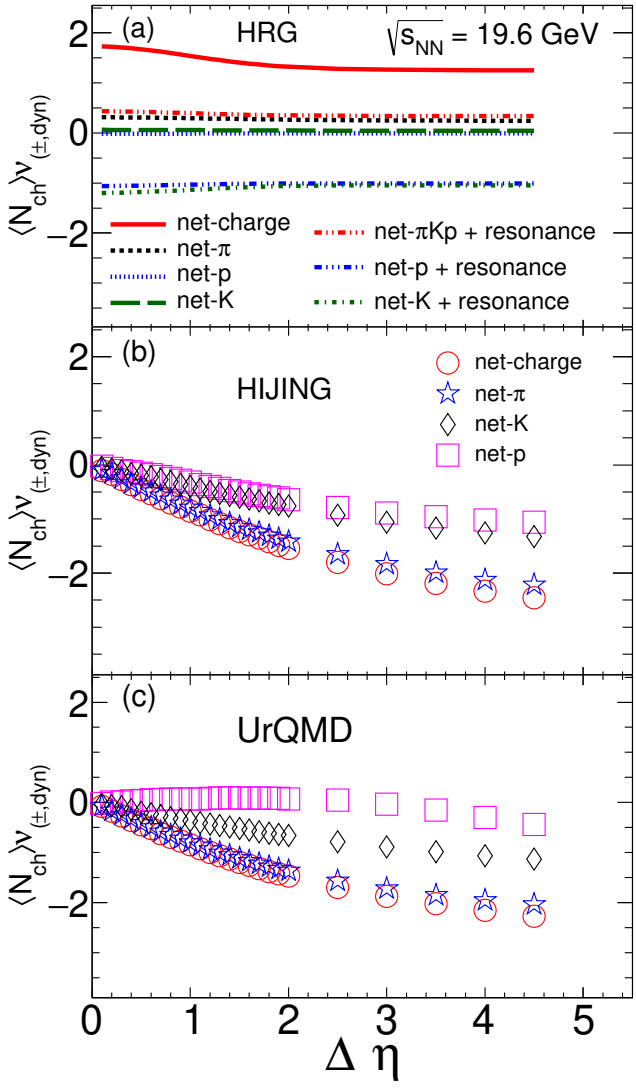

Figure 2.1: Fluctuation parameter $\langle N_{\rm ch}\rangle\nu_{(\pm,{\rm dyn})}$ as a function of $\Delta\eta$ for net-charge, net-pion, net-kaon and net-proton fluctuations for (0−5%) centrality in Au−Au collisions at $\sqrt{s_{NN}}$ = 19.6 GeV with HRG (upper panel), HIJING (middle panel) and UrQMD (lower panel) models. The $\langle N_{\rm ch}\rangle\nu_{(\pm,{\rm dyn})}$ from HRG model calculations for net-charge (solid line), net-π and net-p (dotted lines), net-K (dashed line) without and with resonance (dashed dotted lines) decay. The statistical errors are within symbol size.

of $\langle N_{\rm ch}\rangle\nu_{(\pm,{\rm dyn})}$ for net-charge, net-pion, net-kaon and net-proton as a function of $\Delta\eta$ interval with HRG, HIJING and UrQMD models at $\sqrt{s_{NN}}$ = 19.6 GeV. For the present study, we have used 0.2 million central (0–5%) Au−Au events at each energy in HIJING and UrQMD models. The particles having transverse momentum $0.2 \leq p_T$ (GeV/c) ≤ 5.0 are considered for the present study. The lower p_T selection threshold is motivated by the existence of the experimental measurements performed at RHIC. The $\langle N_{\rm ch}\rangle\nu_{(\pm,{\rm dyn})}$ values estimated from HRG (upper panel), HIJING (middle panel), and UrQMD (lower panel) models are shown as a

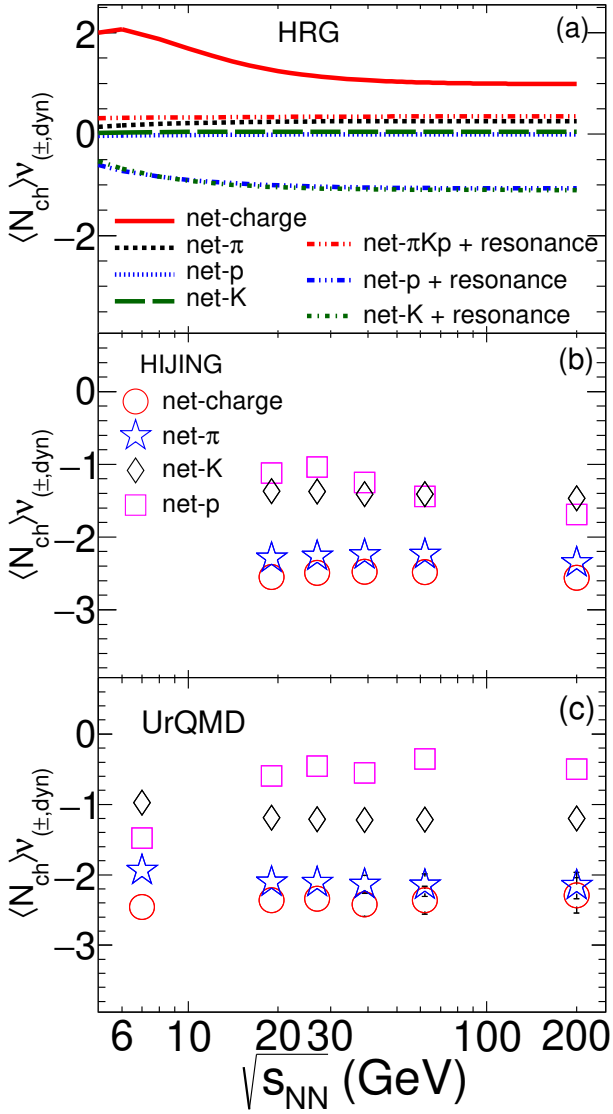

Figure 2.2: Collision energy dependence of $\langle N_{\rm ch}\rangle\nu_{(\pm,{\rm dyn})}$ for net-charge, net-pion, net-kaon and net-proton are calculated using HRG (upper panel), HIJING (middle panel) and UrQMD (lower panel) models for (0−5%) centrality in Au−Au collisions. The $\langle N_{\rm ch}\rangle\nu_{(\pm,{\rm dyn})}$ from HRG model calculations for net-charge (solid line), net-π and net-p (dotted lines), net-K (dashed line) without and with resonance (dashed dotted lines) decay. The statistical errors are within symbol size.

function of $\Delta\eta$. The HRG calculations for net-charge, net-pion, net-kaon, and net-proton fluctuations are performed within the same kinematic acceptance as those used with HIJING and UrQMD models. Charged hadrons of masses up to 2.5 GeV as listed in the particle data book are considered in the HRG model. The HRG model calculations are performed for different cases by considering all the charged hadrons, individual identified stable particles (π, K, p), and contribution of resonance decays to the stable particles. The estimated values of $\langle N_{\rm ch}\rangle\nu_{(\pm,{\rm dyn})}$ are found to be independent of $\Delta\eta$ in the case of the HRG model. However, there is a strong dependence of resonance decay effects observed for the identified particles. The calculation of $\langle N_{\rm ch}\rangle\nu_{(\pm,{\rm dyn})}$ from the HRG model will provide a pure thermal baseline contribution as a function of $\Delta\eta$. In the case of HIJING and UrQMD models, there is a strong dependence of

$\langle N_{\rm ch}\rangle\nu_{(\pm,{\rm dyn})}$ values on $\Delta\eta$ are observed for net-charge as well as for identified particles. The higher $\langle N_{\rm ch}\rangle\nu_{(\pm,{\rm dyn})}$ value at a lower $\Delta\eta$ interval suggests that the correlation is maximum for the smaller $\Delta\eta$ interval.

The curvature of $\langle N_{\rm ch}\rangle\nu_{(\pm,{\rm dyn})}$ shows a decreasing slope up to higher $\Delta\eta$ intervals. This is in contrast to the observation made by the ALICE experiment at higher collision energy $\sqrt{s_{NN}}$ = 2.76 TeV, which shows a flattening trend by extrapolating the fitted curve to higher $\Delta\eta$ range [104]. As can be seen, the $\langle N_{\rm ch}\rangle\nu_{(\pm,{\rm dyn})}$ values for net-pion are closer to the results obtained for net-charge fluctuations. The net-charge fluctuation is dominated by the contribution from the pion fluctuation as the majority of the charged particles are pions. Similarly, the $\langle N_{\rm ch}\rangle\nu_{(\pm,{\rm dyn})}$ values for net-kaon and net-proton are closer to each other with a reduced slope as compared to net-charge in the HIJING model. In the case of the UrQMD model, the slope of the $\langle N_{\rm ch}\rangle\nu_{(\pm,{\rm dyn})}$ values for net-proton shows a flattening trend at a small $\Delta\eta$ and starts decreasing as a function of $\Delta\eta$ at a larger rapidity window. Figure 2.2 shows the

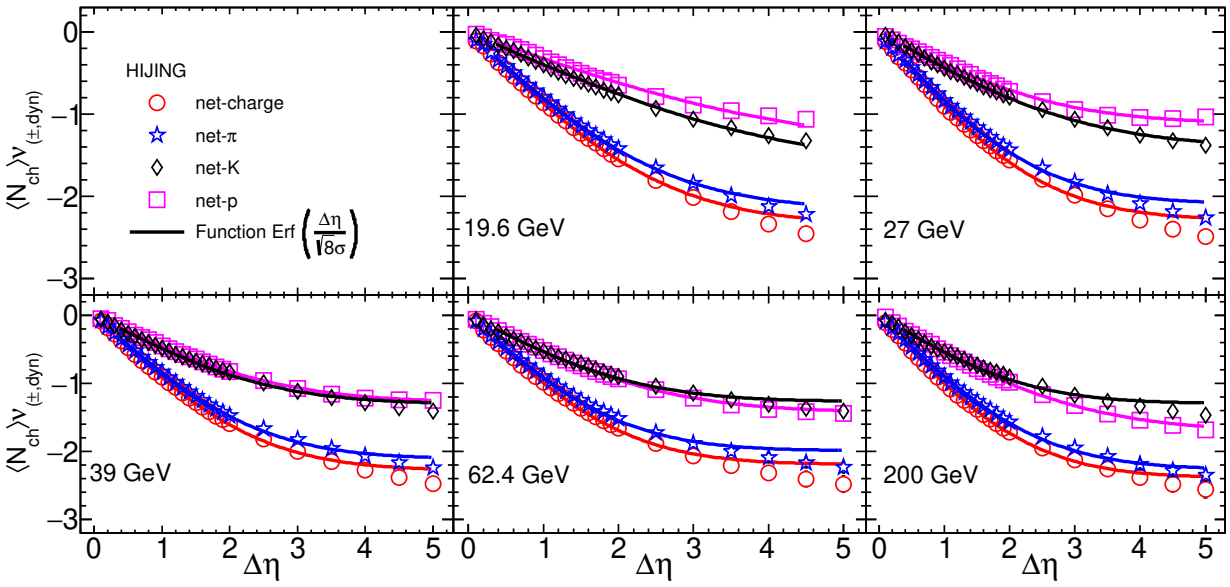

Figure 2.3: The $\langle N_{ch}\rangle\nu_{(\pm,{\rm dyn})}$ for net-charge (red circle), net-pion (blue star), net-kaon (black diamond), and net-proton (magenta square) as a function of $\Delta\eta$ window for (0−5%) centrality in Au−Au collisions at different $\sqrt{s_{NN}}$ in HIJING model. The simulated data points are fitted with the $Erf(\Delta\eta/\sqrt{8}\sigma)$ from $\Delta\eta$ = 0.35 to 4.5 at 19.6 GeV and $\Delta\eta$ = 0.35 to 5.0 at 27–200 GeV respectively. The fitted curves are shown in solid lines. The statistical errors are within symbol size.

collision energy dependence of $\langle N_{\rm ch}\rangle\nu_{(\pm,{\rm dyn})}$ values for net-charge and different identified net particles in most central Au−Au collisions using HRG (upper panel), HIJING (middle panel), and UrQMD (lower panel) models. The $\langle N_{\rm ch}\rangle\nu_{(\pm,{\rm dyn})}$ values for the net-charge in HRG model decrease with increasing collision energies. In the case of identified particles (net π, net p and net K) and contributions of resonance decay to these stable particles, the $\langle N_{\rm ch}\rangle\nu_{(\pm,{\rm dyn})}$ values do not change as a function of $\sqrt{s_{NN}}$. The $\langle N_{\rm ch}\rangle\nu_{(\pm,{\rm dyn})}$ values for net-charge, net-pion, and

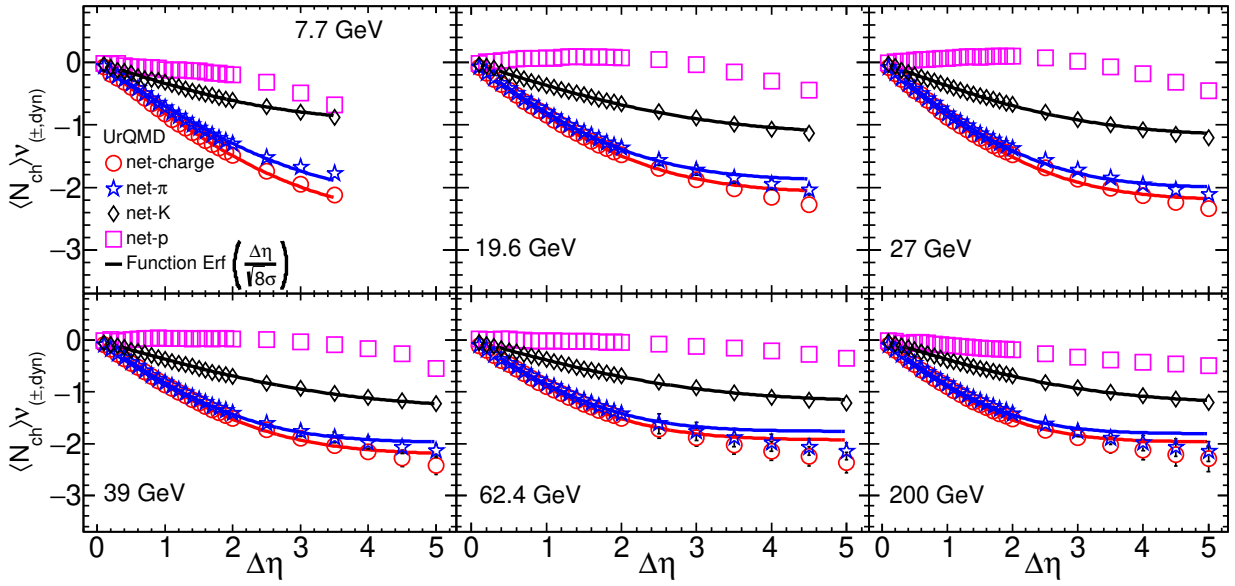

Figure 2.4: The $\langle N_{ch}\rangle\nu_{(\pm,\mathrm{dyn})}$ for net-charge (red circle), net-pion (blue star), net-kaon (black diamond), and net-proton (magenta square) as a function of $\Delta\eta$ window for (0−5%) centrality in Au−Au collisions at different $\sqrt{s_{NN}}$ in UrQMD model. The simulated data points are fitted with the $Erf(\Delta\eta/\sqrt{8}\sigma)$ from $\Delta\eta = 0.35$ to 3.5 at 7.7 GeV, $\Delta\eta = 0.35$ to 4.5 at 19.6 GeV, and $\Delta\eta = 0.35$ to 5.0 at 27–200 GeV respectively. The fitted curves are shown in solid lines. The statistical errors are within symbol size.

net-kaon are independent of $\sqrt{s_{NN}}$ in HIJING and UrQMD models. The $\langle N_{\mathrm{ch}}\rangle\nu_{(\pm,\mathrm{dyn})}$ values for the net-proton case show small energy dependence in both the models. There is a clear particle dependence of $\langle N_{\mathrm{ch}}\rangle\nu_{(\pm,\mathrm{dyn})}$ values for all collision energies in both the models.

Figures 2.3 and 2.4 show the $\langle N_{\mathrm{ch}}\rangle\nu_{(\pm,\mathrm{dyn})}$ as a function of $\Delta\eta$ intervals for (0−5%) centrality in Au−Au collisions at different $\sqrt{s_{NN}}$ using HIJING and UrQMD models, respectively. The $\Delta\eta$ dependence of $\langle N_{\mathrm{ch}}\rangle\nu_{(\pm,\mathrm{dyn})}$ for net-proton is qualitatively different in both HIJING and UrQMD models, whereas net-charge, net-pion and net-kaon show similar behavior in both the models. In the case of the UrQMD model, the $\langle N_{\mathrm{ch}}\rangle\nu_{(\pm,\mathrm{dyn})}$ values are flattened at higher $\Delta\eta$ with increasing $\sqrt{s_{NN}}$. For all the $\sqrt{s_{NN}}$, it is observed that the $\langle N_{\mathrm{ch}}\rangle\nu_{(\pm,\mathrm{dyn})}$ values of net-charge and net-pion have larger suppression as compared to net-proton and net-kaon. The observed suppression of $\langle N_{\mathrm{ch}}\rangle\nu_{(\pm,\mathrm{dyn})}$ for different particles may be due to the difference in the integral of the balance function of different identified particles [110].

Due to the diffusion of charged particles in the hadronic phase, the measured fluctuations may get diluted during evolution of the system and keep on approaching the equillibrated values in the hadronic medium until their kinetic freeze-out. Hence, the experimental measurements of not only the magnitudes of fluctuation quantities at a fixed $\Delta\eta$ but also their dependence on $\Delta\eta$ enable us to explore various aspect of the time evolution of the hot medium and the hadronization mechanism. It is proposed to study the fluctuations of identified particle species and estimated the rate of diffusion at various centre of mass energies ($\sqrt{s_{NN}}$) available at

BNL(RHIC) and in different rapidity interval for the measured particles.

2.4.1 Extraction of diffusion coefficient

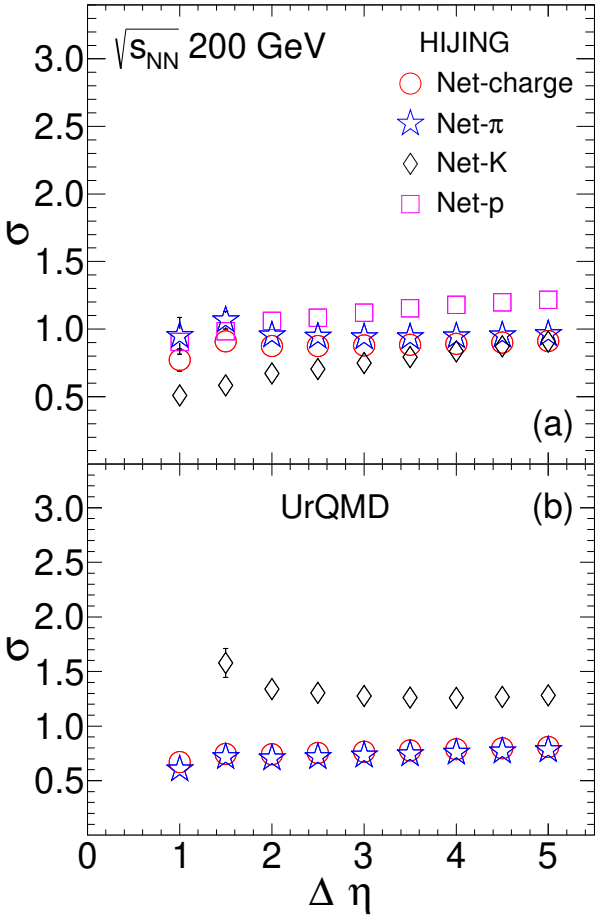

Figure 2.5: Diffusion coefficient σ as a function of $\Delta\eta$ window for net-charge (red circle), net-pion (blue star), net-kaon (black diamond), and net-proton (magenta square) are calculated using HIJING and UrQMD models for (0−5%) centrality in Au−Au collisions. The statistical errors are within symbol size.

The measured fluctuation signals may get attenuated during the evolution of the system from hadronization to kinetic freeze-out because of the diffusion of charged hadrons in rapidity space [106]. Figure 2.3 and 2.4 shows the $\langle N_{\rm ch}\rangle\nu_{(\pm,{\rm dyn})}$ as a function of $\Delta\eta$ intervals for (0−5%) centrality in Au−Au collisions at different center of mass energies($\sqrt{s_{NN}}$) using HIJING and UrQMD models, respectively. Following the Refs. [105, 106], the simulated data points are fitted with the error function[1], Erf($\Delta\eta/\sqrt{8}\sigma$) representing the diffusion in rapidity space. The fitted functions are shown as solid lines in Figs. 2.3 and 2.4. However, note that the breadth of the rapidity coverage is bound to include different physics phenomena at different beam energies. At 200 GeV, the beam rapidity is of order 5.2 while at 7.7 GeV it is of order of 2.

[1]The error function is a mathematical function defined by the integral, $erf(x) = \frac{1}{\sqrt{\pi}}\int_{-x}^{x} e^{-t^2}dt$. It represents the probability that a normally distributed random variable with mean zero and standard deviation of 1 falls within the range $[-x, x]$.

Therefore at $\sqrt{s_{_{NN}}} = 7.7$, and 19.6 GeV we consider $\Delta\eta$ upto 3.5 and 4.5 respectively. The data points are fitted within $\Delta\eta$ range, 0.35–3.5 at 7.7 GeV, 0.35–4.5 at 19.6 GeV, and 0.35–5.0 at energies 27 to 200 GeV, for net-charge, net-pion, net-kaon and net-proton. The fit parameter, σ in $\mathrm{Erf}(\Delta\eta/\sqrt{8}\sigma)$, characterizes the diffusion at freeze-out that accounts for the broadening of the rapidity distributions due to interactions and particle production. We have calculated the diffusion coefficients at $\sqrt{s_{_{NN}}}$ = 7.7, 19.6, 27, 39, 62.4 and 200 GeV for all charge and the identified particles which represent the proxy for conserved quantities (net-baryon, net-electric charge and net-strangeness) from both HIJING and UrQMD models. The slope of the fit function decreases with increasing particle mass. The $\Delta\eta$ dependence of $\langle N_{\mathrm{ch}}\rangle\nu_{(\pm,\mathrm{dyn})}$ for net-proton is qualitatively different in both HIJING and UrQMD models, whereas net-charge, net-pion and net-kaon have similar behaviour in both the models. In the case of UrQMD model, the $\langle N_{\mathrm{ch}}\rangle\nu_{(\pm,\mathrm{dyn})}$ values flattened at higher $\Delta\eta$ with increasing $\sqrt{s_{_{NN}}}$. Hence, the $\langle N_{\mathrm{ch}}\rangle\nu_{(\pm,\mathrm{dyn})}$ as a function of $\Delta\eta$ for net-proton not able to fit with $\mathrm{Erf}(\Delta\eta/\sqrt{8}\sigma)$ function unlike pions and kaons.

Figure 2.5 shows the diffusion coefficient as a function of $\Delta\eta$ window for net-charge, net-pion, net-kaon, and net-proton in Au−Au collisions at $\sqrt{s_{_{NN}}}$ = 200 GeV. The σ values are obtained by fitting the $\langle N_{\mathrm{ch}}\rangle\nu_{(\pm,\mathrm{dyn})}$ up to different $\Delta\eta$ range with the error function. In both the HIJING and UrQMD models, the diffusion coefficient for net-charge and net-pion are independent of $\Delta\eta$ window and match with each other. In HIJING model, the diffusion coefficients of net-kaon and net-proton show small $\Delta\eta$ dependence. The σ values of net-proton are systematically above, whereas σ values of net-kaon are systematically below the net-charge and net-pion values. Due to the qualitatively different nature of curvature of $\langle N_{\mathrm{ch}}\rangle\nu_{(\pm,\mathrm{dyn})}$ as a function $\Delta\eta$ for net-proton in UrQMD model, it was not possible to extract the σ values.

The extracted values of diffusion coefficient of identified particles as a function of $\sqrt{s_{_{NN}}}$ are shown in Fig. 2.6 from both HIJING and UrQMD models. The resulting values of σ are obtained by fitting the $\langle N_{\mathrm{ch}}\rangle\nu_{(\pm,\mathrm{dyn})}$ values up to $\Delta\eta = 3.5$ for 7.7 GeV, 4.5 for 19.6 GeV, and 5.0 for 27−200 GeV respectively with the error function. The σ values for net-charge and net-pion are close to each other at all the studied energies. The σ of net-proton and net-kaon are closer to each other and systematically higher than net-pion at all energies in both the models. We observe that the diffusion coefficients are constant as a function of studied collision energy range $\sqrt{s_{_{NN}}}$ = 7.7 to 200 GeV.

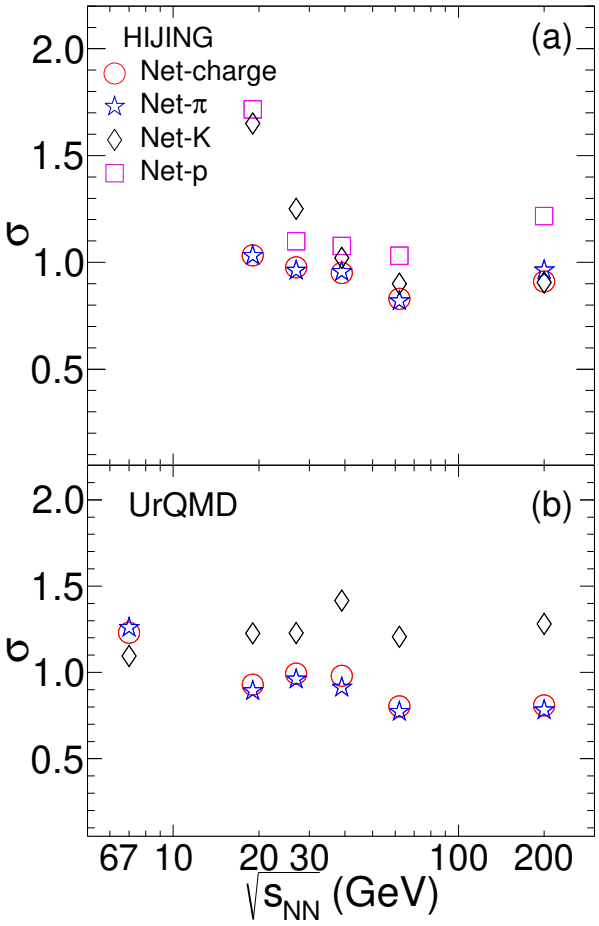

Figure 2.6: The collision energy dependence of diffusion coefficient (σ) for net-charge (red circle), net-pion (blue star), net-kaon (black diamond), and net-proton (magenta square) are calculated using HIJING and UrQMD models for (0−5%) centrality in Au−Au collisions. The statistical errors are within symbol size.

2.5 Summary

In summary, we have studied the fluctuations of net-charge, net-pion, net-kaon, and net-proton using the $\langle N_{\rm ch}\rangle\nu_{(\pm,{\rm dyn})}$ observable within the ambit of HIJING, and UrQMD models at different collision energies available at BNL(RHIC). The $\langle N_{\rm ch}\rangle\nu_{(\pm,{\rm dyn})}$values are estimated up to higher $\Delta\eta$ window. A stronger dependence of the $\langle N_{\rm ch}\rangle\nu_{(\pm,{\rm dyn})}$ value observed for lower $\Delta\eta$ and the decreasing trend continues up to higher $\Delta\eta$ with lower slope in both the models, except the net-proton in the UrQMD model. In case of net-proton in the UrQMD model, the curvature of $\langle N_{\rm ch}\rangle\nu_{(\pm,{\rm dyn})}$ values as a function of $\Delta\eta$ shows different behaviour. The $\langle N_{\rm ch}\rangle\nu_{(\pm,{\rm dyn})}$ values obtained from different model calculations are independent of collision energies but show particle species dependent. The diffusion coefficient (σ) has been estimated by fitting $\langle N_{\rm ch}\rangle\nu_{(\pm,{\rm dyn})}$ as a function of $\Delta\eta$ with the error function. The σ values are independent of collision energies. The σ values of net-kaons and net-protons are systematically higher than net-pion at all the studied energies. This study emphasizes the particle species dependence of diffusion coefficient and provides a realistic baseline for comparison with the experimental data.

Chapter 3

Experimental apparatus and setup

High-energy accelerators serve as necessary instruments within particle physics, enabling scientists to delve into the elemental constituents of the cosmos and scrutinize the governing laws of their interactions. These accelerators impart particles with exceptionally high velocities, facilitating collisions at energies replicating the conditions prevalent in the early universe. Particle accelerators exist in two primary forms: fixed-target machines and colliders. Fixed-target machines involve the acceleration of particles directed to collide with a stationary target. On the other hand, collider machines propel particles in opposing directions within a ring, leading to collisions at specific interaction points. The motivation behind developing collider machines, such as the Large Hadron Collider, lies in their capacity to achieve substantially higher collision energies than fixed-target machines. This elevated capability enables researchers to venture into previously inaccessible energy domains, embarking on novel trajectories within the realm of particle physics.

The study presented in this thesis originates from the data acquired utilizing the ALICE detector situated at the LHC. The structure of this chapter is organized as follows. The subsequent section briefly overviews the experiments conducted at the Large Hadron Collider at CERN. Section 3.2 delves into an in-depth discussion of the ALICE detector, offering insights into the various sub-detectors of ALICE, with a specific emphasis on their relevance to the analysis conducted within the scope of this thesis. Further details on each sub-detector are discussed in subsequent subsections from 3.2.1 to 3.2.5.

3.1 Large Hadron Collider (LHC)

The Large Hadron Collider at CERN stands as the most powerful accelerator globally, positioned beneath the Swiss-French border with a circumference spanning 27 kilometres. Constructed with unprecedented energy levels, the LHC was designed to tackle fundamental ques-

tions in particle physics. Its primary achievement was the discovery of the Higgs boson in 2012, marking a significant milestone. The LHC continues to play a pivotal role in probing Higgs boson properties, searching for new particles beyond the Standard Model, and delving into enigmatic realms like dark matter, dark energy, and the extreme conditions of quark-gluon plasma. The collider's comprehensive physics program aims to deepen our understanding of fundamental matter constituents and the forces governing their interactions, seeking to unravel the mysteries of the universe's origins and evolution.

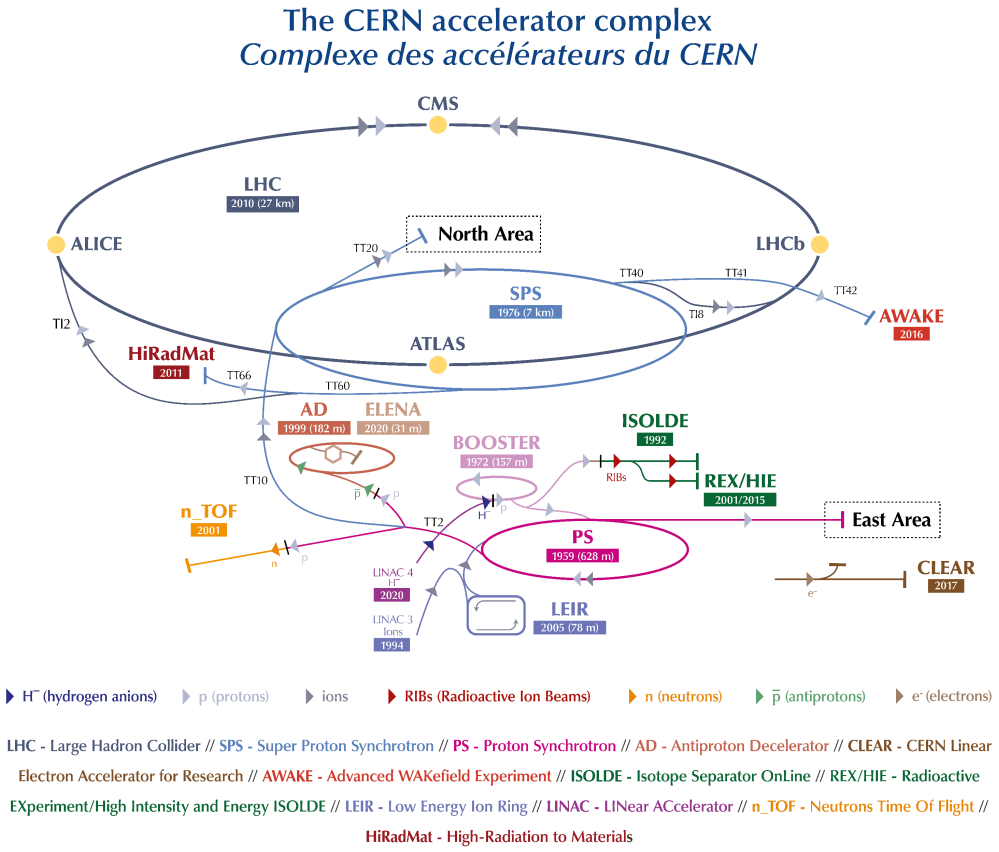

Figure 3.1: Schematic view of the CERN accelerator complex in 2019. Image sourced from [126]

At the LHC, data acquisition is organized into distinct time units. LHC run periods, spanning multiple years, are succeeded by extended shutdown periods. The two major LHC runs are Run-1, which occurred from 2009 to 2013, and Run-2, which occurred from 2015 to 2018. During Run-2 at the LHC, several experiments were conducted to address various aspects of particle physics. The key experiments include:

1. **ATLAS (A Toroidal LHC ApparatuS):** ATLAS is a general-purpose detector designed to investigate a wide range of physics phenomena, including the Higgs boson and new particles beyond the Standard Model [127].

2. **CMS (Compact Muon Solenoid):** CMS is another general-purpose detector, similar

to ATLAS, with a focus on precision measurements of the Higgs boson, searches for new particles, and studies of the fundamental forces [128].

3. **ALICE (A Large Ion Collider Experiment):** ALICE specializes in heavy-ion collisions, aiming to study the properties of quark-gluon plasma under extreme conditions. It provides insights into the early moments of the universe [129].

4. **LHCb (Large Hadron Collider beauty):** LHCb is dedicated to studying the subtle differences between matter and antimatter, particularly in the realm of beauty (b) and charm (c) quarks [130].

Each experiment was driven by specific physics motivations, ranging from unravelling the origin of mass to comprehending the asymmetry between matter and antimatter. The monumental scale of these experiments underscores the need for precision and sensitivity in capturing rare events and phenomena, pushing the boundaries of our knowledge in particle physics. Figure 3.1 provides a schematic view of the CERN accelerator complex during Run 2 in 2019, offering a comprehensive representation of the technical facilities available at CERN [126]. The immense scale of these experiments reflects the necessity for precision and sensitivity in capturing rare events and phenomena, pushing the boundaries of our knowledge in particle physics.

3.2 A Large Ion Collider Experiment (ALICE)

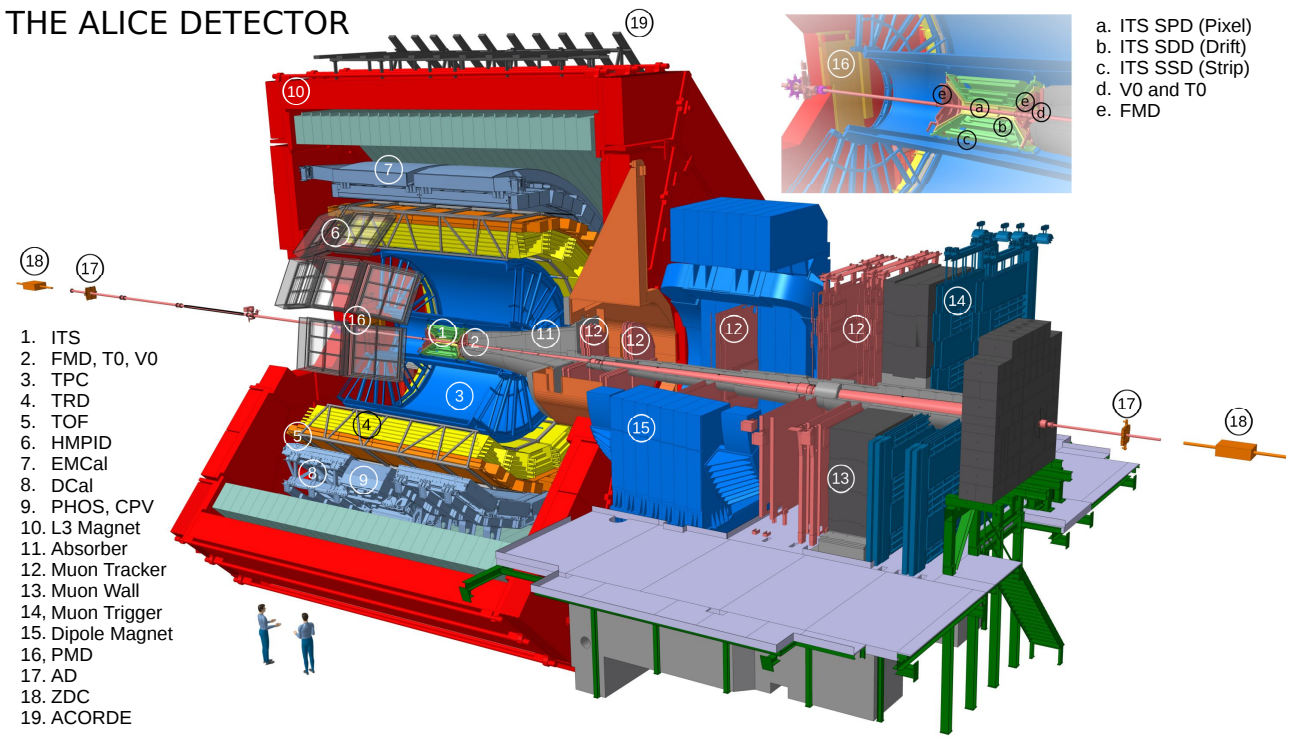

Figure 3.2: Schematic view of the ALICE detector. Image sourced from [131].

ALICE, situated within the LHC at CERN, is a multi-detector heavy-ion experiment designed to explore QCD and the strong interaction sector of the Standard Model. Focused on ultrarelativistic heavy-ion collisions, its primary goal is to investigate strongly interacting matter and the quark-gluon plasma under extreme energy density and temperature conditions. ALICE's comprehensive study involves analyzing particles like hadrons, electrons, muons, and photons resulting from heavy-nuclei collisions, leveraging its detector system's unique abilities to identify soft and hard probes. Its scientific program encompasses collision scenarios, including lighter ions, lower energy levels, and proton-nucleus runs, aiming to vary interaction volumes and energy densities. Furthermore, ALICE contributes vital reference data during proton-proton runs at peak LHC energy, addressing specific strong-interaction inquiries complementarily to other LHC detectors [132].

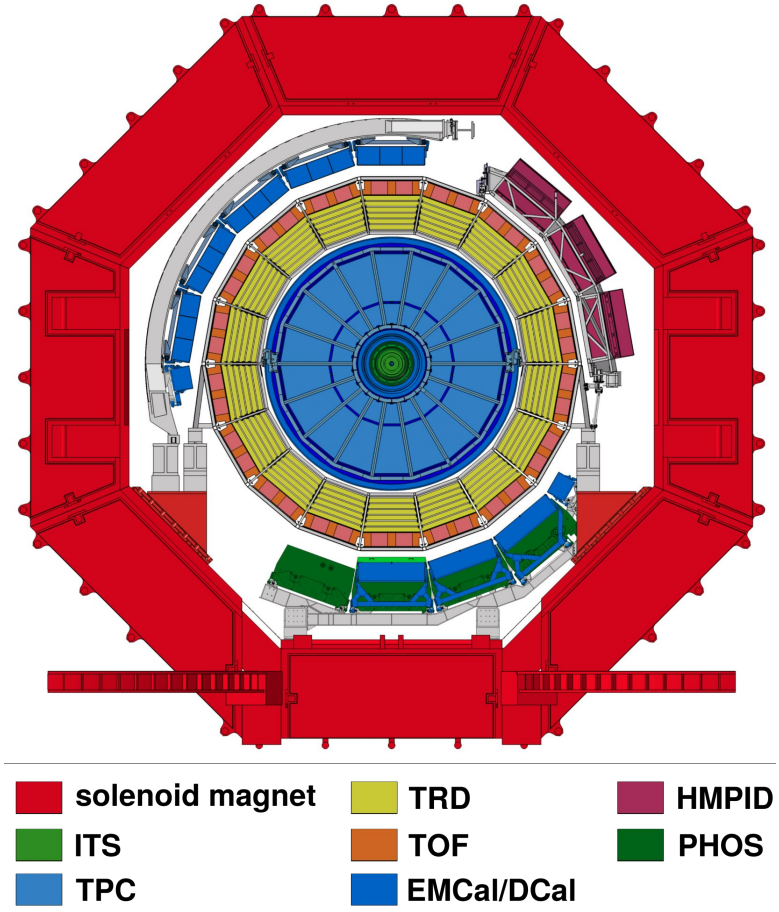

Figure 3.3: Schematic transverse view of the ALICE detector. Image sourced from [133].

The ALICE detector has dimensions of 16×16×26 m^3 and weighs ≈ 10,000 tons. It comprises an array of detectors employing diverse particle reconstruction and identification tech-

niques. Positioned within a central region covering a pseudorapidity of $|\eta| \leq 0.9$, it houses a substantial solenoid magnet, repurposed from the L3 experiment at LEP, generating a maximum 0.5 tesla field parallel to the beam direction. The detector structure consists, from innermost to outermost, of an Inner Tracking System (ITS) [134], a cylindrical Time-Projection Chamber (TPC) [135], and three particle identification arrays: Time-of-Flight (TOF) [136], High Momentum Particle Identification (HMPID) [137], and Transition Radiation (TRD) [138] detectors. Additionally, it includes two electromagnetic calorimeters - the PHOton Spectrometer (PHOS) [139] and the Electro Magnetic Calorimeter (EMCal) [133, 140]. Most detectors cover the full azimuth, except for HMPID, PHOS, and EMCal. The forward muon arm incorporates absorbers, a large dipole magnet, and fourteen tracking and triggering chamber planes. Small-angle detectors, including the Zero Degree Calorimeter (ZDC) [141], Photon Multiplicity Detector (PMD) [142], Forward Multiplicity Detector (FMD) [143], and VZERO (V0) [143], contribute to global event characterization and triggering. The TZERO (T0) [143] detector aids in timing and an array of scintillators (ACORDE) [144] atop the L3 magnet serves as a trigger for cosmic rays. For a comprehensive overview of the acceptance and location of the various detector systems, refer to Table 3.1 and Figures 3.2 and 3.3.

In this thesis, the tracking and particle identification tasks were accomplished using the ITS, TPC and EMCal detectors, and the V0 detectors were additionally utilized for triggering purposes for the analysis. The subsequent sections offer a brief overview of these detectors, specifically about their relevance in the analysis conducted within this thesis.

3.2.1 Inner Tracking System (ITS)

The detector system comprises six concentric cylindrical layers comprising high-resolution silicon detectors, spanning from an inner radius of 4 cm to an outer radius of 43 cm from the beam axis (z-axis), enclosing a pseudorapidity range of $|\eta| < 0.9$ and providing complete azimuthal coverage. These layers include the Silicon Pixel Detector (SPD), Silicon Drift Detector (SDD), and double-sided Silicon Strip Detectors (SSD), positioned at increasing radii from the beam pipe. The SPD layers, positioned at 3.9 cm and 7.6 cm from the beam axis, are designed to handle track densities of approximately 50 particles/cm^2. The subsequent two layers experience lower particle densities of around 7.2 and 2.5 particles/cm^2, located at 15.0 and 23.9 cm from the beam axis. Finally, the last two layers, consisting of double-sided Silicon Strip Detectors, are positioned at 38.0 and 43.0 cm, with particle densities below 1/cm^2. The ITS serves multiple essential purposes: Enhancement of momentum and angle resolution for particles reconstructed by the TPC and reconstruction of particles navigating through inactive regions of the TPC. Specifically, it significantly improves the resolution of the distance of closest approach (DCA)

Table 3.1: Overview of ALICE detector subsystems, detailing acceptance in η calculated from the nominal interaction point, with a 360° azimuth unless specified. Positions represent distances from the interaction point to the detector face, given as radii for barrel detectors (inner and outer for TPC and TRD) or along the beam (z coordinate) for others [132].

Detector	Acceptance (η, φ)	Position (m)
ITS layer 1,2 (SPD)	± 2, ± 1.4	0.039, 0.076
ITS layer 3,4 (SDD)	± 0.9, ± 0.9	0.150, 0.239
ITS layer 5,6 (SSD)	± 0.97, ± 0.97	0.380, 0.430
TPC	$\eta < \pm 0.9$ at r = 2.8 m	0.848, 2.466
	$\eta < \pm 1.5$ at r = 1.4 m	
TRD	$\eta < \pm 0.84$	2.90, 3.68
TOF	$\eta < \pm 0.9$	3.78
HMPID	$\eta < \pm 0.6$, $1.2° < \varphi < 58.8°$	5.0
PHOS	$\eta < \pm 0.12$, $220° < \varphi < 320°$	4.6
EMCal	$\eta < \pm 0.7$, $80° < \varphi < 187°$	4.36
ACORDE	$\eta < \pm 1.3$, $-60° < \varphi < 60°$	8.5
	Muon Spectrometer	
Tracking chambers	$-4 < \eta < -2.5$	$-$ 5.36
Trigger chambers	$-4 < \eta < -2.5$	$-$ 16.2
ZDC	$\eta > 8.8$	$\pm$ 113
	$\varphi < 10°$, $6.5 < \eta < 7.5$	
	$\varphi < 32°$, $4.8 < \eta < 5.7$	
PMD	$2.3 < \eta < 3.7$	3.64
FMD disc 1	$3.62 < \eta < 5.03$	3.2
FMD disc 2	$1.7 < \eta < 3.68$	0.834
FMD disc 3	$-3.4 < \eta < 1.7$	$-$ 0.752
V0A	$2.8 < \eta < 5.1$	3.4
V0C	$-3.7 < \eta < -1.7$	$-$ 0.897
T0A	$4.61 < \eta < 4.92$	3.75
T0C	$-3.28 < \eta < -2.97$	$-$ 0.727

of particle tracks to the primary vertex to better than 100 μm [132, 134, 145].

The four outer layers feature analogue readout capabilities, facilitating ionization loss ($\mathrm{d}E/\mathrm{d}x$) measurements and enabling the identification of low-momentum particles that might not reach the TPC. The ITS exhibits a $\mathrm{d}E/\mathrm{d}x$ resolution of approximately 11%. The ITS exhibits superior relative momentum resolution, achieving better than 2% for pions with transverse momenta ranging from 0.1 GeV/c to 3 GeV/c. The detector's granularity[1] is optimized to accommodate a high-multiplicity environment, specifically designed for a track density of 8000 per unit of rapidity tracks at mid-rapidity. With a spatial resolution in the order of a few tens of micrometres, the ITS detectors, especially those closest to the primary vertex (with the best precision at

[1]The term "granularity" refers to the level of detail or resolution with which a particle detector can spatially resolve or detect individual particles or particle tracks. Detectors with higher granularity are often favoured for better precision in reconstructing particle events.

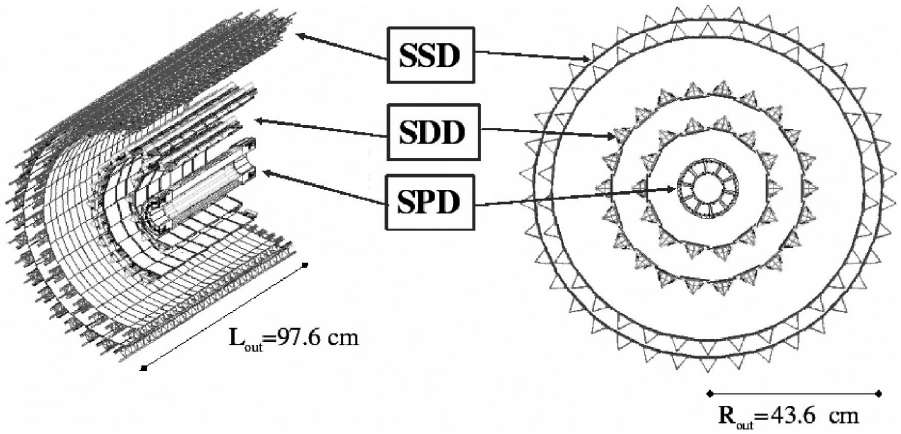

Figure 3.4: Schematic view of the ALICE Inner Tracking System. Image sourced from [145].

12 μm), provide impact-parameter measurements with resolution suitable for the detection of heavy-flavored particles (better than 60 μm in the rφ plane for p_{T} >1 GeV/c). Furthermore, at momenta exceeding 3 GeV/c, the ITS's spatial precision significantly contributes to the overall momentum resolution, solidifying its importance in high-energy particle tracking [145].

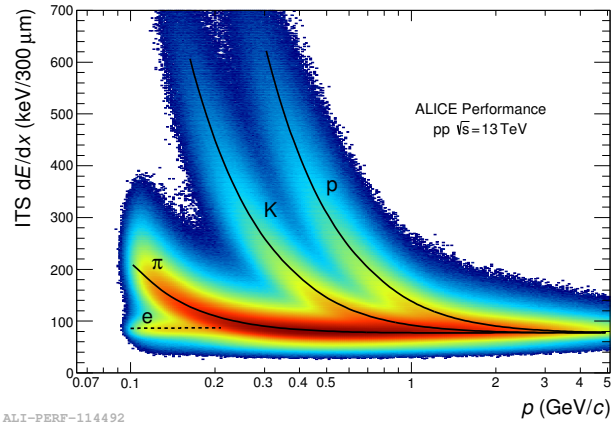

Figure 3.5: Average dE/dx of charged particles as a function of their momentum for ITS pure standalone tracks measured in proton-proton collisions at $\sqrt{s}$ = 13 TeV.

Figure 3.5 shows the average ionization loss (dE/dx) of charged particles as a function of their momentum, exclusively measured by the Inner Tracking System (ITS) in proton-proton collisions at a center-of-mass energy of 13 TeV. The curves represent a parametrization of the detector response, employing a hybrid approach with a polynomial function at low momentum per unit mass (p/m) and a "PHOBOS"[2] Bethe-Bloch formula [146].

[2]The PHOBOS detector was one of the four large experiments at RHIC and was designed to investigate the

3.2.2 Time Projection Chamber (TPC)

The primary tracking component within the central barrel, the Time-Projection Chamber, is optimized to deliver robust charged-particle momentum measurements, working in conjunction with other central barrel detectors. It facilitates efficient two-track separation, enables particle identification via energy loss measurements ($\mathrm{d}E/\mathrm{d}x$), and facilitates precise vertex determination. Covering a considerable phase space in pseudo-rapidity, the TPC spans $|\eta| < 0.9$ for tracks exhibiting full radial track length, encompassing matches in ITS, TRD, and TOF detectors. Additionally, it extends its coverage to about $|\eta| \leq 1.5$ for reduced track length, although with a compromised momentum resolution. Operating with complete azimuthal coverage, barring the dead zones in SPD, the TPC ensures a broad p_{T} range from as low as 0.1 GeV/c up to 100 GeV/c with excellent momentum resolution.

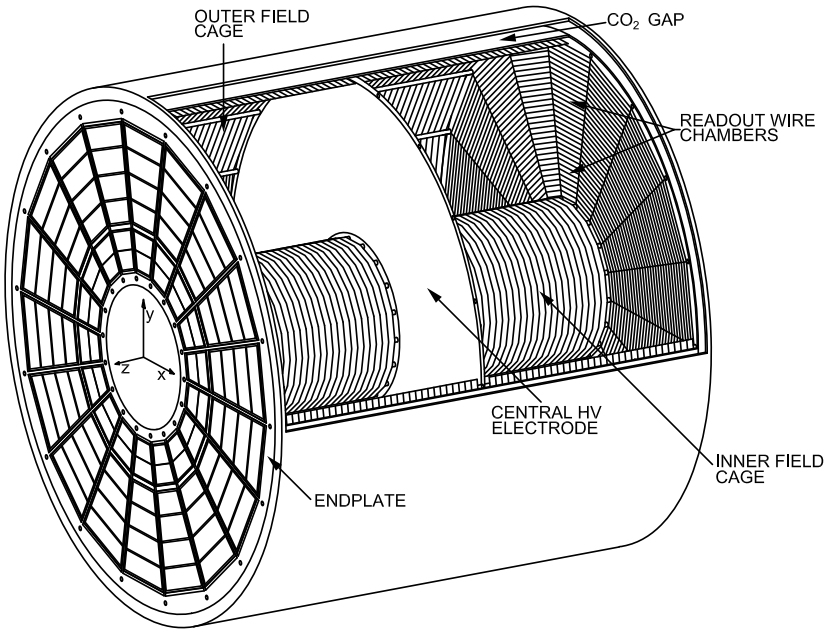

Figure 3.6: 3D view of the TPC field cage. The high voltag electrode is located at the center of the drift volume. The end-plates with 18 sectors and 36 readout chambers on each end are shown. Image sourced from [132]

The TPC adopts a cylindrical structure with an inner radius of approximately 85 cm, determined by the maximum acceptable hit density, and an outer radius of 250 cm, established to maintain a $\mathrm{d}E/\mathrm{d}x$ resolution below 10%. Spanning a length of about 500 cm along the beam direction, the TPC layout, as illustrated in Fig. 3.6, comprises a sizable field cage segmented by a central high-voltage electrode. This division ensures a uniform electric drift towards the end-caps. Filled with a gas mixture of Ne + CO_2 (90% + 10%), totalling 88 m^3, the TPC

properties of nuclear matter under extreme temperatures and energy densities. It concluded its data-taking operations in 2005.

facilitates the transport of primary electrons over 2.5 m on each side of the central electrode to the endplates. The endplates host multi-wire proportional chambers featuring cathode pad readout, arranged in 18 trapezoidal sectors per endplate, providing a total of 2×18 trapezoidal sectors, each covering 360° in azimuth. These endplates record the ionization electron position and time concerning the start of the collision, enabling the reconstruction of the original charged particle's path through the TPC gas. Additionally, the detector integrates a large cylindrical field cage isolated from the surrounding environment and filled with CO_2 to minimize electric field distortions within the drift volume. Figure 3.6 depicts a schematic detailing these components.

The TPC readout chambers have 159 tangential pad rows, allowing a track to generate up to 159 clusters within the TPC volume. The reconstruction of these tracks employs a Kalman filter[3] approach [147], utilizing both the TPC and the ITS. The track reconstruction process involves several key steps [148, 149]:

1. **Inward Propagation**

   - Tracks are initially identified in the TPC. Track seeds are constructed with two TPC clusters and the vertex point, followed by three clusters without the vertex constraint.
   - Seeds are propagated inward and updated at each step with the nearest cluster, subject to a proximity cut.
   - An algorithm is employed to prevent redundant reconstructions of the same physical track by searching for pairs of tracks with a fraction of common clusters exceeding a specified limit.
   - Only tracks with at least 20 clusters and missing no more than 50% of expected clusters are accepted.

2. **Transition to ITS**

   - Reconstructed TPC tracks serve as seeds for track finding in the outermost ITS layer.
   - Seeds are propagated inward and updated at each ITS layer by clusters within a proximity cut, accounting for positions and errors. Seeding is performed in two passes, with and without a vertex constraint.

[3]In particle physics experiments, detectors track charged particles through subsystems. The Kalman filter optimally combines information from these subsystems, enhancing trajectory accuracy amid experimental uncertainties and noise. This tool significantly improves precision in particle track reconstruction within complex detector systems.

- The result is a tree of track hypotheses in the ITS for each TPC track. Candidates are sorted according to reduced χ^2,[4] and conflicts between tracks are resolved based on cluster sharing.
- The highest-quality candidate from each hypothesis tree is added to the reconstructed event.

3. **Outward Propagation and Matching**

- All tracks are extrapolated to their point of closest approach to the preliminary interaction vertex.
- Tracks are refitted by the Kalman filter in the outward direction using clusters from the previous stage.
- Tracks reaching the TRD attempt to match with TRD tracklets[5] in each of the six TRD layers.
- Tracks reaching the TOF detector are matched to TOF clusters. Further propagation for matching with signals in EMCal, PHOS, and HMPID.

4. **Final Stage**

- All tracks are propagated inwards, starting from the outer radius of the TPC.
- Tracks are refitted in each detector (TPC and ITS) using previously found clusters.
- Determination of the track's position, direction, inverse curvature, and its associated covariance matrix.

In this thesis, electron identification relies on measuring the energy loss within the TPC gas. This process involves concurrently measuring the specific energy loss, charge, and momentum for each particle passing through the detector gas. Distinctive ionization energy loss patterns in the TPC gas indicate particles with different masses. The energy loss is quantified using the Bethe-Bloch formula and is further parametrized by a function initially proposed by the ALEPH collaboration [151].

$$f(\beta\gamma) = \frac{P_1}{\beta^{P_4}}\left(P_2 - \beta^{P_4} - ln\big(P_3 - \frac{1}{(\beta\gamma)^{P_5}}\big)\right) \tag{3.1}$$

Here, β represents the particle velocity, γ is the Lorentz factor, and P_1 to P_5 denote the fit parameters. In Fig. 3.8, the specific energy loss measured in the TPC is plotted against particle

[4] χ^2 is a statistical measure used to quantify the goodness of fit between a model and observed data. A smaller χ^2 value indicates a better agreement between the model and the observed data and vice versa.

[5] tracklets are concise track segments used as initial components for reconstructing complete particle trajectories within a detector system.

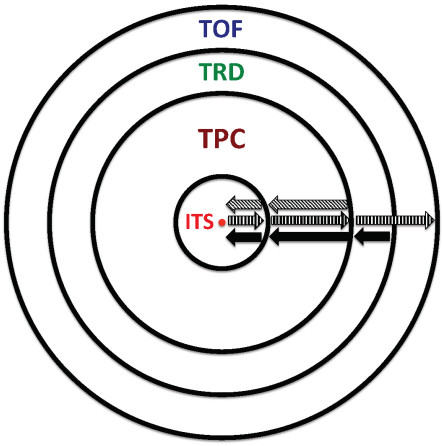

Figure 3.7: Schematic representation illustrating the three stages of the combined track finding process. Cross-sectional views of the central barrel detectors are presented perpendicular to the beam direction, ranging from the innermost (ITS) to the outermost (TOF) detectors. Image sourced from [150]

momentum, showing distinct separation among various particle species. The lines illustrate parametrizations of the expected mean energy loss. Notably, the TPC exhibits an energy loss resolution of approximately 5.2% for pp events and 6.5% for central Pb-Pb collisions. A comprehensive description of the TPC's specific energy loss utilization, particularly in electron identification, is outlined in Section 4.3.

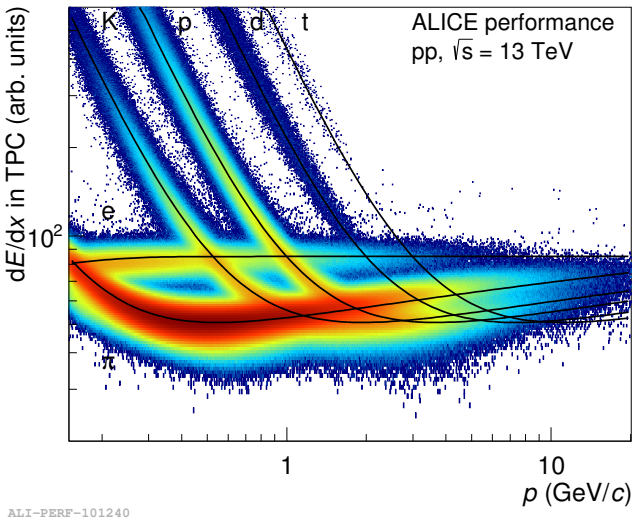

Figure 3.8: Specific energy loss ($\mathrm{d}E/\mathrm{d}x$) of charged particles as a function of their momentum measured with the ALICE Time Projection Chamber at a magnetic field of 0.2 T in proton-proton collisions at $\sqrt{s}$ = 13 TeV [152].

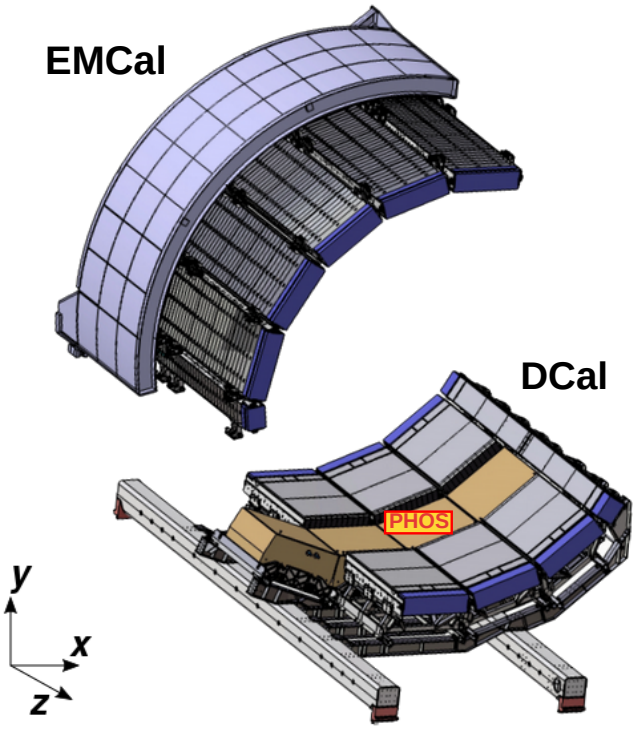

Figure 3.9: Schematic representation of the EMCal on the left and DCal on the right, emphasizing the placement of modules at approximately opposite azimuthal positions. The brown shading indicates the presence of the PHOS calorimeter within the DCal. Image sourced from [133].

3.2.3 ElectroMagnetic Calorimeter (EMCal)

Detector description and characteristics

In this analysis, the electromagnetic calorimeter plays an essential role in electron identification. Functioning as a lead-scintillator sampling calorimeter, it employs Shashlik technology with alternating lead and polystyrene scintillator layers, complemented by wavelength-shifting fibres [140]. Positioned 4.5 meters radially from the beam pipe, between the space-frame support structure and the L3 magnet coils, the EMCal spans two azimuthal ranges (Fig. 3.9). The fundamental unit of the EMCal is the module, comprising 2 × 2 optically isolated towers, as illustrated in Fig. 3.10. Each tower is individually read out and covers a region of $\Delta\eta \times \Delta\varphi \simeq 0.0143 \times 0.0143$. Modules are grouped into larger supermodules (SM) (12 × 24 modules); each SM weighs about 7.7 metric tons. The EMCal SMs were assembled in stages (SM0-3 in 2009, SM4-11 in 2011, and SM12–19 in 2014), with the last set forming the Di-Jet Calorimeter (DCal) for dijet measurements [153]. In this thesis, the entire system (EMCal+DCal) is collectively referred to as EMCal [133]. The calorimeter's design incorporates SMs of different sizes: full-size, 2/3-size, and 1/3-size. Each full-size SM comprises 288 modules organized into strip modules. The EMCal consists of ten full-size SMs and two 1/3-size SMs, covering $|\eta| < 0.7$ in pseudorapidity and $80° < \varphi < 187°$ in azimuth. The DCal is constructed from six 2/3-size SMs

and two 1/3-size SMs, featuring acceptance regions of $0.22 < |\eta| < 0.7$, $260° < \varphi < 320°$ and $|\eta| < 0.7$, $320° < \varphi < 327°$. Figure 3.11 provides a schematic view of the acceptance and the SM numbering scheme used in the offline software. The EMCal comprises 12,288 towers, while the DCal consists of 5,376 towers. The SMs are positioned in the experimental cavern, ensuring that the radial distance of the SM front face from the interaction point is approximately 4.3 m, as illustrated in Fig. 3.9. Table 3.2 and Figure 3.10 summarizes the physical characteristics and structure of the EMCal modules.

Table 3.2: Summary of physical parameters for the EMCal module

Parameter	**Value**
Tower Size (on front face)	$6.0 \times 6.0 \times 24.6\,\mathrm{cm}^3$
Tower Size (at $\eta = 0$)	$\Delta\eta \times \Delta\varphi \simeq 0.0143 \times 0.0143$
Sampling Ratio	1.44 mm Pb / 1.76 mm Scint.
Layers	77
Scintillator	Polystyrene (BASF143E + 1.5%pTP + 0.04%POPOP)
Absorber	natural lead
Effective radiation length X_0[6]	12.3 mm
Effective Molière radius R_M[7]	3.2 mm
Effective Density	5.68 g/cm^3
Sampling Fraction[8]	1/10.5
No. of radiation lengths	20.1

3.2.4 Clusterization

The calorimeter captures particles generating an electromagnetic (or hadronic) shower spreading over neighbouring cells. Calorimeter clusters, aggregates of cells with energy surpassing the noise threshold, are the primary objects in reconstruction. The reconstructed cluster energy approximates the particle energy for particles depositing full energy (e.g., photons, electrons). Depending on transverse momentum and calorimeter granularity, mesons like π^0 and η, decaying into two photons, may appear as separate or merged clusters. Various clusterization methods in the EMCal can distinguish these decay products depending on incident particle energies, and the method selection is analysis goal-dependent. In this study, the V2 clusterization algorithm is employed for the analysis to generate clusters. The clusterization process begins by identifying a 'seed' cell with a specified threshold energy (500 MeV). Subsequently, the algorithm iterates through neighbouring cells surrounding the seed cell, incorporating adjacent cells that satisfy a minimum energy threshold (100 MeV). This iterative process continues,

[6]Depth at which energy of electron (photon) is reduced by $1/e$.

[7]Measure of the lateral spread of an electromagnetic shower, 90% of shower energy is contained within cylinder of radius R_M (99% within 3.5 R_M).

[8]Ratio of the energy deposited in the active detector material to the total energy of incident particle.

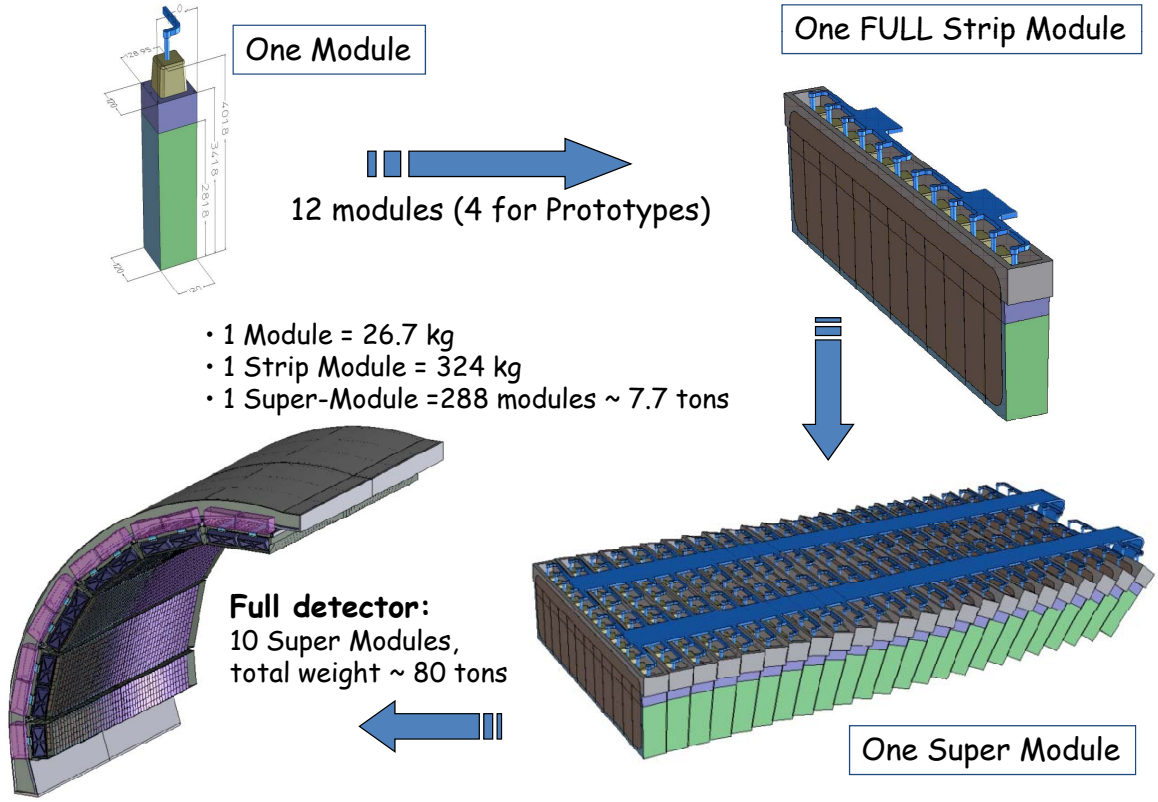

Figure 3.10: Schematic representation of the modular structure of EMCal detector. Image sourced from [133, 154].

expanding the cluster by seeking neighbours of the cells already added until the energy criteria are no longer met. Following the cluster identification, the clustering algorithm scans the remaining cells to identify a new seed cell to initiate the process again [155]. After the formation of a cluster, its energy E is computed by summing the energies of its constituent cells (E_i^{cell}), $E = \sum_i E_i^{cell}$, with i referring to a cell within the cluster. To establish the cluster's position (centroid) within the ALICE global coordinate system, a weighted average of the cell positions (x_i, y_i, z_i) is computed usine Eqn. 3.2.

$$\langle x \rangle = \sum_i \frac{\omega_i x_i}{\omega_{tot}}, \qquad \langle y \rangle = \sum_i \frac{\omega_i y_i}{\omega_{tot}}, \qquad \langle z \rangle = \sum_i \frac{\omega_i z_i}{\omega_{tot}}, \tag{3.2}$$

Each cell within the cluster is assigned a logarithmic weight (ω_i based on a logarithmic correlation with the cell's energy. This logarithmic weighting approach is employed due to the characteristic exponential decrease in shower energy. Using a linear energy weight could disproportionately influence the calculation, particularly given the ALICE EMCal's substantial granularity.

$$\omega_i = \text{Maximum}\left[0, \omega_{\max} + \ln(E_i^{cell}/E)\right] \quad \text{and} \quad \omega_{\text{tot}} = \sum_{\text{i}} \omega_{\text{i}} \tag{3.3}$$

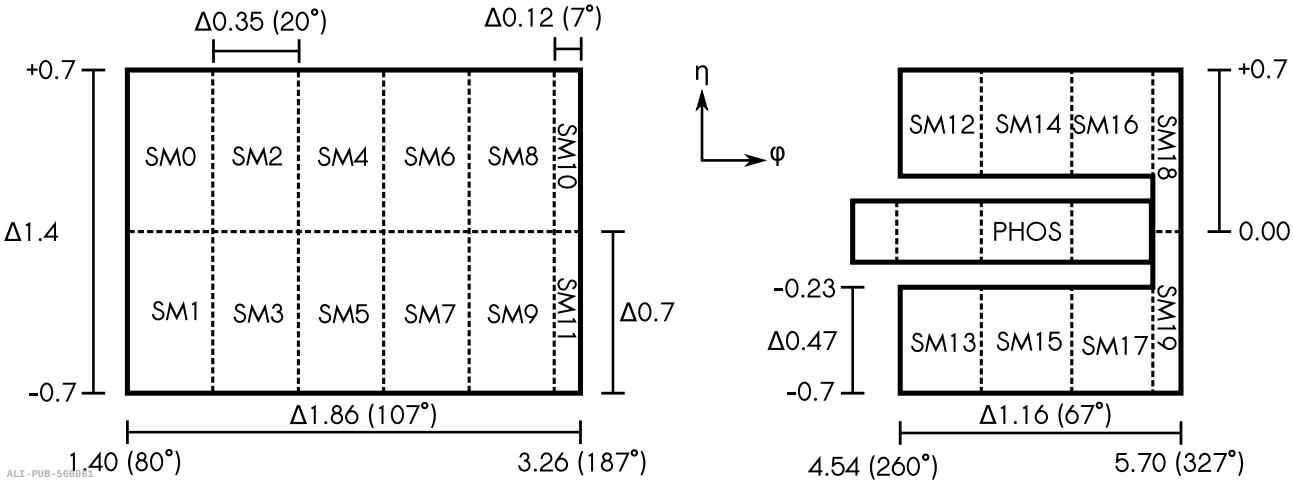

Figure 3.11: The diagram provides a geometric overview of the EMCal and DCal detectors in the $\eta - \varphi$ plane, featuring all 20 Super Modules (SM) and the PHOS detector in the DCal gap [133].

The parameter ω_{max} is a fixed constant selected to minimize the impact of cells with energy below 1.1% of the cluster's total energy. In the case of the ALICE EMCal, ω_{max}. For a more in-depth explanation of this weighting methodology, refer to [156].

Track-Cluster matching

The EMCal measures electromagnetic interaction energies, particularly for photons and electrons, though hadrons can also deposit energy through ionization or nuclear interactions[9]. Clusters are associated with charged-particle tracks to distinguish showers from charged and neutral particles. The matching algorithm extrapolates tracks to the EMCal, considering the ALICE magnetic field and energy loss. The process involves three steps: extrapolation to a fixed depth, refinement for angular distance, and calculation of residuals in η and φ.

If multiple tracks meet the matching criterion for a cluster, the closest track is chosen as the associated track. Residual distributions of clusters to their closest track are shown in Fig. 3.12, illustrating $\Delta\eta$ (a) and $\Delta\varphi$ (b) as functions of track p_{T} . Considering the dependence on particle transverse momentum, a p_{T} -dependent window in the $\Delta\eta - \Delta\varphi$ plane is used for selecting cluster-track pairs [133].

$$
\begin{aligned}
|\Delta\eta^{\mathrm{residual}}| &\leq 0.010 + (p_{\mathrm{T,track}} + 4.07)^{-2.5}\,, \\
|\Delta\varphi^{\mathrm{residual}}| &\leq 0.015 + (p_{\mathrm{T,track}} + 3.65)^{-2.0} \qquad (3.4) \\
\text{where, } \Delta\eta^{\mathrm{residual}} &= \eta_{\mathrm{track}} - \eta_{\mathrm{cluster}} \text{ and } \Delta\varphi^{\mathrm{residual}} = \varphi_{\mathrm{track}} - \varphi_{\mathrm{cluster}}
\end{aligned}
$$

[9]In EMCal, electron interactions are primarily governed by the radiation length (X_0), whereas hadron interactions are determined by the nuclear interaction length (λ_{int}).

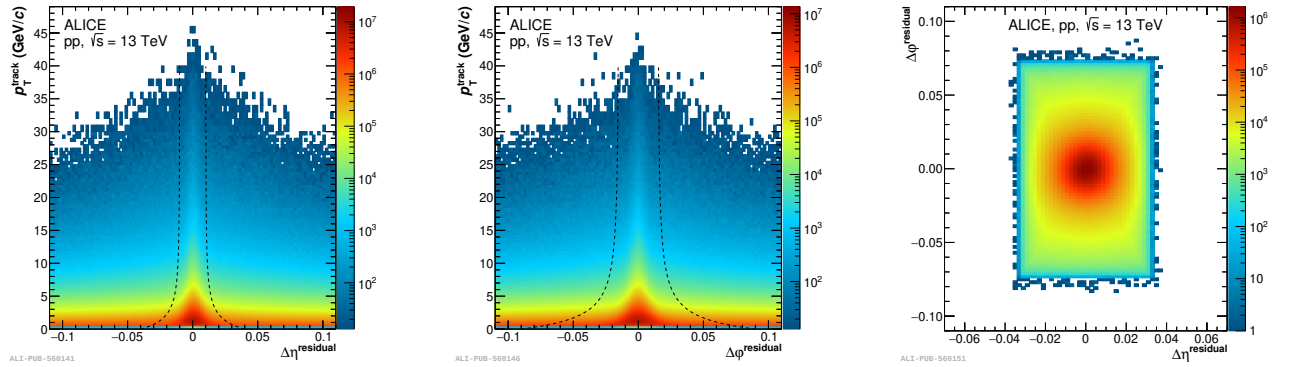

(a) (b) (c)

Figure 3.12: Dependence of the distance between a cluster and the closest projected track in η (a) or φ (b) on the track p_{T} , and for matched track-cluster pairs (c), in proton-proton collisions at $\sqrt{s}$ = 13 TeV obtained with the minimum bias trigger. The clusters are reconstructed using the V2 clusterizer. The suggested selection criteria, as defined in Eqn. 3.4, are represented by the black lines in the panels (a) and (b).

To differentiate between charged hadrons and electrons inside EMCal. The ratio of cluster energy (E) to track momentum(p) (i.e., E/p) is measured, exploiting the fact that electrons deposit their entire energy inside the EMCal, resulting in E/$p \approxeq 1$. In contrast, hadrons deposit only part of their total energy, and therefore, they tend to have an E/p ratio < 1[10]. Also, distinguishing between electron and photon clusters in the EMCal involves matching EMCal clusters to TPC tracks, as photons do not generate tracks inside the TPC. In this thesis, the electrons were identified and selected by analyzing the E/p ratio using data from the EMCal and TPC detectors.

Shower shape

The distribution of energy within a cluster, known as the 'shower shape', is characterized using a parametrization of the ellipse axes on the shower surface [157, 158]. The energy spread within a cluster across the η and φ directions is quantified using a covariance matrix that includes terms $\sigma^2_{\varphi\varphi}$, $\sigma^2_{\eta\eta}$ and $\sigma^2_{\eta\varphi}$. This matrix is calculated by incorporating logarithmic energy weights, denoted as ω_i (See Eqn. 3.2). After the energy weighting is applied, the shower dispersion, reflecting the second moment concerning the mean shower position coordinate, is determined for both the η and φ directions.

[10]In the ultra-relativistic limit ($pc \gg m_0c^2$), the rest mass term becomes negligible compared to the momentum term, simplifying the energy-momentum relation to: $E = \sqrt{E^2 + p^2} \approxeq p$ in natural units.

$$\begin{aligned}
\sigma^2_{\eta\eta} &= \sum_{\mathrm{i}} \frac{\omega_{\mathrm{i}}\eta_{\mathrm{i}}^2}{\omega_{\mathrm{tot}}} - \sum_{\mathrm{i}} \left(\frac{\omega_{\mathrm{i}}\eta_{\mathrm{i}}}{\omega_{\mathrm{tot}}}\right)^2 \\
\sigma^2_{\varphi\varphi} &= \sum_{i} \frac{\omega_i\varphi_i^2}{\omega_{tot}} - \sum_{i} \left(\frac{\omega_i\varphi_i}{\omega_{tot}}\right)^2 \\
\sigma^2_{\eta\varphi} &= \sum_{i} \frac{\omega_i\eta_i\varphi_i}{\omega_{tot}} - \sum_{i} \frac{\omega_i\eta_i}{\omega_{tot}} \cdot \sum_{i} \frac{\omega_i\varphi_i}{\omega_{tot}}
\end{aligned} \tag{3.5}$$

The parameters that define the shower shape, M02 (σ^2_{long}) and M20 ($\sigma^2_{\mathrm{short}}$), are determined as the eigenvalues of the covariance matrix, computed as follows:

$$\begin{aligned}
\mathrm{M02}(\sigma^2_{\mathrm{long}}) &= 0.5(\sigma^2_{\varphi\varphi} + \sigma^2_{\eta\eta}) + \sqrt{0.25(\sigma^2_{\varphi\varphi} - \sigma^2_{\eta\eta})^2 + \sigma^2_{\eta\varphi}}\,, \\
\mathrm{M20}(\sigma^2_{\mathrm{short}}) &= 0.5(\sigma^2_{\varphi\varphi} + \sigma^2_{\eta\eta}) - \sqrt{0.25(\sigma^2_{\varphi\varphi} - \sigma^2_{\eta\eta})^2 + \sigma^2_{\eta\varphi}}
\end{aligned} \tag{3.6}$$

The shower surface is established by the intersection of the cone encapsulating the shower with the front plane of the calorimeter, as illustrated in Fig. 3.13. The use of parameters M02 (long axis) and M20 (short axis) to measure the spread of particle showers enables the discrimination of symmetric electromagnetic showers (characterized by a small spread), which typically originate from photons or electrons, from nonsymmetric showers resulting from hadronic interactions involving neutrons, protons, or charged pions. Due to the distinct interactions of electrons and hadrons with the EMCal material, their showers in the detector exhibit, on average, slightly different long and short axes. Electrons, influenced by the magnetic field and rescattering in the detector material, display a tail in the M02 distribution extending to larger values, especially at low cluster energy. In contrast, hadrons exhibit a broader distribution with extended tails toward higher shower shape values. This thesis employs a cut on the long axis of the particle shower to enhance the purity of the electron signal [133, 159].

Trigger

The EMCal detector serves as a crucial decision-making tool during data acquisition, triggering the recording of specific events. The EMCal can trigger at two different levels, Level-0 (L0) and Level-1 (L1). In this study, the EMCal L1 gamma triggers, EG2 and EG1 [160, 161], are employed to select events with high energy depositions in the EMCal detector, indicating intermediate and high-momentum electrons or photons. This selection is achieved using a sliding 2 × 2 window algorithm that aggregates analogue charge information from patches of 4 × 4 towers. Upon reaching a predefined threshold, the data is forwarded to a Central

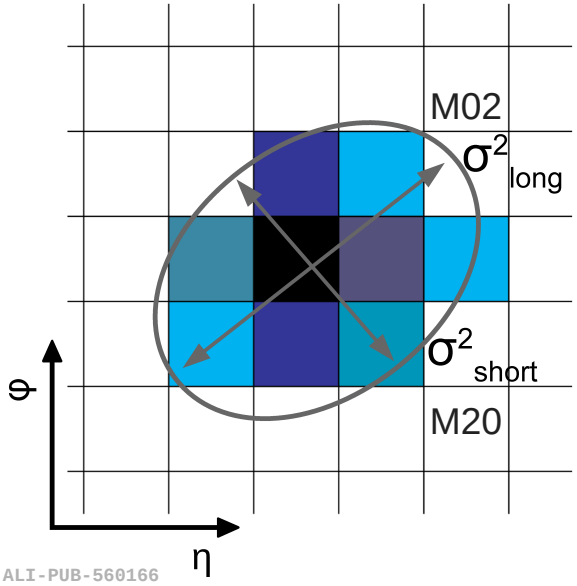

Figure 3.13: The schematic representation of an EMCal cluster with an ellipse parametrization of the shower shape illustrates its axes. The various colours indicate the amount of energy deposited in each cell, with darker shades representing higher energy levels [133].

Trigger Processor [162], which consolidates trigger information from other detectors (refer to Sec. 3.2.5 for details). Throughout the pp 13 TeV data collection, ranging from LHC16 to LHC18, the analog charge threshold corresponds to $\sim$ 4.5 GeV for EG2 and $\sim$ 10.5 GeV for EG1. This thesis utilizes events triggered by minimum bias selection for the lower p_{T} range ($3 \leq p_{\mathrm{T}}$ (GeV/c) ≤ 6). Additionally, EMCal triggered events, EG2 and EG1, with varying energy thresholds, contribute to extending the measurement to higher p_{T} ranges. EG2, with a threshold of $\sim$ 4.5 GeV, facilitates the measurement in the region $6 \leq p_{\mathrm{T}}$ (GeV/c) ≤ 12. Similarly, the EG1 trigger, with a threshold of $\sim$ 10.5 GeV, is applied for the measurement in the range $12 \leq p_{\mathrm{T}}$ (GeV/c) ≤ 35. By employing EG2 and EG1 triggers, the recording of events containing high-momentum electrons is increased, ensuring sufficient statistics for measuring charm and beauty hadron decay electrons up to higher transverse momenta, extended to $p_{\mathrm{T}} =$ 35 GeV/c [19].

3.2.5 VZERO (V0)

The V0 detector, a small-angle detection system, consists of two scintillator arrays, V0-A[11] and V0-C, strategically positioned on opposite sides of the ALICE interaction point. V0-A, situated 340 cm from the vertex on the side opposite the muon spectrometer, spans the pseudo-rapidity range $2.8 < \eta < 5.1$. In contrast, V0-C is fixed at the face of the front absorber of the muon spectrometer, positioned 90 cm from the vertex, covering the pseudo-rapidity range -3.7

[11] In the ALICE experiment, the detectors V0 and T0 refer to two distinct systems, A and C. These refer to the detector facing the ATLAS side and the CMS side.

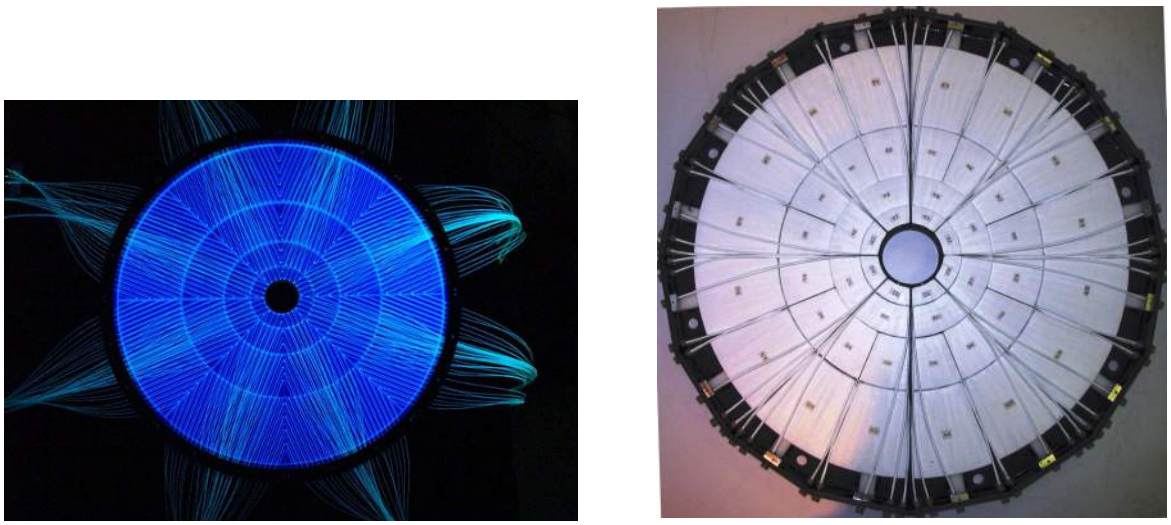

(a) (b)

Figure 3.14: Front view of V0-A (a) and V0-C (b) arrays. Image sourced from [132]

$< \eta <$ -1 [143]. V0-A and V0-C serve as critical components, offering minimum bias triggers for the central barrel detectors in proton-proton and heavy-ion collisions. The interaction of protons with the residual gas in the vacuum chamber generates tracks throughout the ALICE subdetectors. The minimum bias proton-gas trigger is employed to reject false events [163]. Like the EMCal, the V0 detector is crucial in triggering during the data acquisition. In the specific data-taking period under consideration in this thesis, the V0 detector played a vital role in providing a minimum bias trigger, a criterion for event selection and recording. A coincidence of signals surpassing a defined threshold in both the V0-A and V0-C arrays is required to activate the MB trigger.

Chapter 4

Measurement of electrons from beauty-hadron decays

4.1 Introduction

This chapter delves into the intriguing realm of heavy-quarks, precisely the charm and beauty quarks. Due to their large masses, heavy-quarks are primarily produced in the initial stages of hard scattering processes in hadronic collisions [164]. Their production occurs within a time frame shorter than the QGP formation time [165] ($\tau_{\rm QGP} \sim 1$ fm/c [87]), because their mass is much larger than the thermal energy scale, i.e. $m_{\rm c,b} \gg k_{\rm B}T_{\rm QGP}$, where $k_{\rm B}$ is the Boltzmann constant and $T_{\rm QGP}$ is the QGP temperature. Their trajectory within the medium encompasses a series of elastic (collisional) and inelastic (gluon radiation) collisions with the constituents of the hot and dense QCD matter [166–170]. Which makes them excellent probes for studying the QGP [164, 171], as they act as a direct observers of the entire evolution of the produced medium.

Due to their short lifetimes (t $\sim 10^{-12}$ s), D and B mesons undergo decay before they reach the detector. Therefore, they have to be studied through their decay products. The reconstruction of beauty-hadrons in heavy-ion collisions presents a formidable challenge due to their small production cross section and the large number of decay channels. Although it is feasible to reconstruct beauty-hadrons, like in the case of measuring $B^{\pm}$ mesons through their decay into J/ψ and K$^{\pm}$ particles, the small branching ratios of these channels inherently make such measurements very difficult. Additional insights can be obtained through comprehensive measurements of decay products from beauty-hadrons, including non-prompt J/ψ and non-prompt D mesons, as well as leptons originating from semi-leptonic decays of heavy-flavor hadrons. The investigation of open heavy-flavour production in ALICE employs two complementary approaches: 1) Full reconstruction of D and B mesons through their hadronic decay modes, and 2)

from the measurement of leptons originating from the leptonic or semi-leptonic decay modes of heavy-flavour hadrons. Studying leptons produced from heavy-quark decays provides valuable information about a broad range of hadrons and heavy-quark momenta, which helps to understand the complex interplay between collisional and radiative processes. The semi-electronic decay mode is exploited in this thesis, where the heavy-flavours undergo weak interactions, resulting in their decay into an electron(positron), anti-neutrino(neutrino), and one or more hadrons. The term "electron" indicates both electrons and positrons throughout the text. This decay channel has a branching ratio of approximately 10%. However, due to the undetectable neutrino, the momentum of the parent particles cannot be fully reconstructed, making it challenging to identify the heavy-flavour decay electrons (HFe). Therefore, to isolate these electrons, the non-heavy-flavour electrons (non-HFe) (i.e. background electrons) are subtracted from the inclusive electron sample. Exploiting the comparatively longer decay length of beauty-hadron decay compared to other electron sources, we can effectively extract the beauty-hadron decay electrons from the HFe sample [27].

The bullet points represent the primary motivations and objectives for studying and measuring electrons originating from beauty-hadron decays in proton-proton collisions at $\sqrt{s} = 13$ TeV:

1. Probing High Transverse Momentum Region: To explore beauty decay electrons within a higher transverse momentum range (up to 35 GeV/c), an area previously uncharted within the ALICE experiment.

2. Testing Perturbative QCD Models: The measurement of electrons from beauty-hadron production cross sections in proton-proton collisions is crucial for verifying the pQCD calculations including the widely used frameworks like FONLL [87, 88, 172] and GM-VFNS [89].

3. Establishing References for Heavy-Ion Collisions: The measurements in proton-proton collisions serve as a baseline for studying nuclear modifications in proton-nucleus (p−A) and nucleus-nucleus (A−A) collisions. This groundwork is vital in examining the mass-dependent energy loss within the medium, shedding light on the complex interactions occurring in these high-energy, heavy-ion collision environments [27, 173].

This chapter is structured as follows. The subsequent section outlines the analysis strategy used and the technical details. In Sec. 4.3, we discuss the techniques used in electron identification using TPC and EMCal. In Sec. 4.4, we focus on identifying and estimating the non-heavy-flavour electrons. Subsequently, in Sec. 4.5, we elaborate on the procedure for differentiating electrons from charm and beauty hadron decays to obtain the raw yield of electrons originating from beauty-hadron decay. Further, in Sec. 4.8, we delve into the acceptance and reconstruction Efficiency correction. Finally, Sec. 4.10 is dedicated to comprehensively exploring

systematic uncertainty studies.

4.2 Analysis stratergy

The measurements of electrons from beauty-hadron decays are generally done in four main stages [27]: (1) selecting suitable tracks, (2) identifying electrons, (3) extracting the signal to estimate the proportion of electrons originating from beauty-hadron decays, and (4) applying corrections for selection efficiencies and geometrical acceptance. The following bullet points provide a concise analysis overview with technical details.

1. The TPC and the EMCal detectors are used to identify the inclusive electron sample. This is achieved by measuring the distance of closest approach(DCA) to the primary vertex distribution for the range of $3 \leq p_{\mathrm{T}}$ (GeV/c) ≤ 35 .

2. The DCA distributions of hadron contamination, which include cases where hadrons are mistakenly identified as electrons, are estimated and subsequently subtracted from the DCA distribution of inclusive electrons. This process yields pure electron DCA distributions.

3. The DCA distribution of non-HFe, also known as photonic electron, is estimated from the enhanced Monte Carlo (MC) sample using the photonic electron tagging method (more details in Sec. 4.4).

4. The DCA distribution of non-HFe is subtracted from the DCA of pure electrons. The resultant DCA distribution primarily comprises electrons originating from charm and beauty decays, and therefore, it is called HFe DCA.

5. The DCA distribution templates for charm and beauty decay electrons are generated from the Monte Carlo simulations and corrected to have realistic behaviour as observed in actual data.

6. The HFe DCA distribution is fitted with charm and beauty decay electron templates using a weighted log-likelihood method to extract the raw beauty decay electron yield. Similarly, the inclusive electron DCA distribution is fitted with templates for hadronic, photonic, charm, and beauty decay electrons using a log-likelihood method to extract the raw beauty decay electron yield.

7. The raw beauty yield obtained through both methods undergoes corrections for acceptance, tracking, and particle identification (PID) efficiency to obtain the final beauty-hadron decay electron cross section.

4.2.1 Software

- The analysis was conducted within the AliROOT framework using the software packages provided by the Heavy Flavour Electron working group.
- To obtain the beauty decay electron cross section, the following classes were utilized: AliAnalysisHFEppEMCalBeauty.h, AliAnalysisHFEppEMCalBeauty.cxx, and AddTaskHFEppEMCalBeauty.C. These can be located in the Aliphysics path: AliPhysics/PWGHF/hfe.
- In order to ensure correct particle identification response and pile-up rejection, AddTaskPIDResponse.C and AddTaskPhysicsSelection.C were incorporated.
- AliTaskCDBconnect.C and EmcalCorrectionTask_NewNLFromFlorian.C were integrated into the EMCal correction task to calibrate misaligned modules and address problematic channels of the EMCal detector.
- For the EMCal correction tasks, the yaml files ElectronConfig_pp_NewNL-Aug25.yaml and ElectronConfig_ppMC_NewNL-Aug25.yaml containing the necessary parameters were used for data and MC, respectively [174]. These files can be found in the alimonitor path: alice/cern.ch/user/d/dthomas/yaml.
- To replicate the shift in the mean and resolution of DCA distribution in MC as observed in data, the improver task AliAnalysisTaskSEImproveITS.h, AliAnalysisTaskSEImproveITS.cxx, and AddTaskImproveITS.C were employed with the option SetMimicData(kTRUE). These can be located in the Aliphysics path: PWGHF/vertexingHF/macros [175].

4.2.2 Data set and event selection

The analysis was conducted using the LEGO train operations with Analysis Object Data (AOD) with the following data sets of pp collisions at 13 TeV:

- `LHC16 kl`(pass2) periods
- `LHC18 bdefhlgimnop` (pass2) periods

The selected runlist utilized for the analysis was based on the runs identified as "good" by the Data Preparation Group [176], with the detector requirements including SSD, SPD, SDD, V0, TPC, and EMCal. Events triggered by the Minimum Bias (MB) selection are used for the lower p_{T} range $3 \leq p_{\mathrm{T}}$ (GeV/c) ≤ 6. While two specific EMCal triggered events, EG2 and EG1, with two different energy thresholds, are used to provide the necessary statistics for extending the measurement to higher a p_{T} range. The trigger threshold for EG2 is $\sim$ 4.5 GeV, allowing for the

measurement of the region $6 \leq p_{\mathrm{T}}$ (GeV/c) ≤ 12. Similarly, the EG1 trigger with a threshold ∼10.5 GeV is utilized to measure the region $12 \leq p_{\mathrm{T}}$ (GeV/c) ≤ 35 [133]. A restriction on the primary Z vertex position ($|\mathrm{V_Z}| \leq \pm$ 10 cm) from the centre of the ALICE detector system is enforced along the beam direction to ensure a uniform reconstruction efficiency of the charged particles. A cut requiring more than two contributors to the primary vertex is implemented to select events with at least two tracks and a vertex located within the Z-vertex range. Pile-up events from the sample are discarded by employing the PhysicsSelectionTask with default pile-up cuts [177].

Table 4.1: The number of events selected after passing the selection criteria

Trigger	MB	EG2	EG1
Number of events ($\times 10^6$)	859	37	33

4.2.3 Monte Carlo

The MC sample used for the analysis consists of LHC18f4b anchored to LHC16k and LHC16l data periods, as well as LHC18l5b anchored to LHC18 periods [176]. The sample is is enriched with signals from π^0 and η particles to enhance the statistics of electrons originating from their decays at higher p_{T} , enabling a more precise estimation of photonic electron tagging efficiency at high p_{T} . Additionally, the sample has been enriched with charm and beauty events to boost the statistics of electrons originating from heavy-flavor hadron decays, which is necessary for the calculation of charm and beauty decay electron templates. The total number of events selected after applying all the selection cuts approximates to 16.7×10^6.

4.3 Identification of electrons using TPC and EMCal

4.3.1 Track reconstruction and selection

Tracks undergo a rigorous selection process for electron identification involving a series of specific track selection cuts. AOD tracks that successfully pass the filter mask `kTrkGlobalNoDCA` are considered for electron identification. These selection criteria are individually applied to each track, aiming to isolate a high-purity electron sample while excluding spurious and uncorrelated tracks that might generate signals in the detector. Table 4.2 outlines and summarises the detailed track selection cuts.

The filterBit `AliAODTrack::kTrkGlobalNoDCA` incorporates a standard cut with a very loose DCA. A $p_{\mathrm{T}} \geq 3$ GeV/c cut is imposed to ensure an accurate track-cluster matching. The

Table 4.2: A summary of track selection criteria used for filter mask `kTrkGlobalNoDCA`

Track Cut	**Selection Value**
All tracks p_{T}	≥ 3 GeV/c
Rapidity	$\lvert\eta\rvert < 0.6$
Number of TPC crossed rows for tracking	≥ 70
Number of TPC crossed rows for $\mathrm{d}E/\mathrm{d}x$ calculation	≥ 60
Ratio of TPC found/findable crossed rows	≥ 0.8
Number of ITS clusters	≥ 3
Hit on SPD layer	kAny
ITS and TPC refit	Required
DCA_{xy}	≤ 1 cm
DCA_{z}	≤ 2 cm
χ^2 clusters of the momentum fit in the TPC	4
Reject kink candidates	Required
TPC–EMCal matching	$\Delta\eta \leq 0.010 + (p_{\mathrm{T,track}} + 4.07)^{-2.5}$ $\Delta\varphi \leq 0.015 + (p_{\mathrm{T,track}} + 3.65)^{-2}$

EMCal detector's acceptance extends up to $|\eta| < 0.7$; therefore, a stricter limit of $|\eta| < 0.6$ is enforced to avoid edge effects and ensure uniform track reconstruction efficiency. Tracks with at least 70 TPC crossed rows are regarded as good quality tracks, meeting the criteria essential for this analysis. Moreover, a minimum of 80 TPC crossed rows is required for $\mathrm{d}E/\mathrm{d}x$ calculations crucial to particle identification. A minimum cut of 0.8 on the ratio of the number of found TPC crossed rows divided by the number of findable crossed rows is applied. Additionally, a minimum number of ITS hits, coupled with a hit in at least one of the SPD layers, is imposed to suppress gamma conversion electrons within the ITS. Each track candidate must undergo a final refit, employing the Kalman filter back to the identified primary vertex, to successfully pass through both the ITS and TPC. A stringent DCA cut of 1 cm in the radial direction and 2 cm along the beam direction is applied to the primary vertex, effectively rejecting tracks not originating from the primary vertex. Furthermore, a χ^2/ndf cut is applied to each track to suppress the contribution of a random uncorrelated combination of clusters in TPC during momentum reconstruction. Kink candidates, characterized by tracks exhibiting deviations from the continuous particle trajectory model due to in-flight decays or Bremsstrahlung emissions, are excluded from further analysis. This step is taken because the $\mathrm{d}E/\mathrm{d}x$ resolution of the TPC is less accurate for kink tracks compared to regular tracks. To identify electrons and differentiate them from photons within the EMCal, tracks originating from the TPC are matched with clusters detected in the EMCal. The deviation in both azimuthal angle (φ) and pseudorapidity (η) between the projection of charged particle tracks from the TPC onto the EMCal surface and the reconstructed cluster in the EMCal is required within,

$$\Delta\eta \leq 0.01 + (p_{\mathrm{T,track}} + 4.07)^{-2.5} \quad \text{and} \quad \Delta\varphi \leq 0.015 + (p_{\mathrm{T,track}} + 3.65)^{-2} \tag{4.1}$$

where, $\Delta\eta = \eta_{\text{track}} - \eta_{\text{cluster}}$ and $\Delta\varphi = \varphi_{\text{track}} - \varphi_{\text{cluster}}$.

4.3.2 Electron identification

The analysis utilizes the ALICE central-barrel detectors in the mid-rapidity region, the ITS is used for determining the reconstructed primary and secondary vertices, as well as for tracking. The TPC is also used for tracking, particle identification and momentum measurement of charged particles. The EMCal is employed for electron identification and triggering to select high p_{T} electron events. In TPC, particle identification is performed by measuring $\mathrm{d}E/\mathrm{d}x$ from the gas within the TPC as a function of the charged particle's momentum as shown in figure 4.1(a). Electrons are selected in TPC by implementing a $-1 \leq \mathrm{n}_{\sigma,\text{TPC}} \leq 3$ cut, where $\mathrm{n}_{\sigma,\text{TPC}}$ represents the deviation of the measured signal in the detector from the expected value for electrons, expressed in terms of the detector resolution i.e.

$$\mathrm{n}_{\sigma,\text{TPC}} = \frac{(\mathrm{d}E/\mathrm{d}x)_{\text{measured}} - (\mathrm{d}E/\mathrm{d}x)_{\text{expected}}}{\sigma^{\text{TPC}}} \tag{4.2}$$

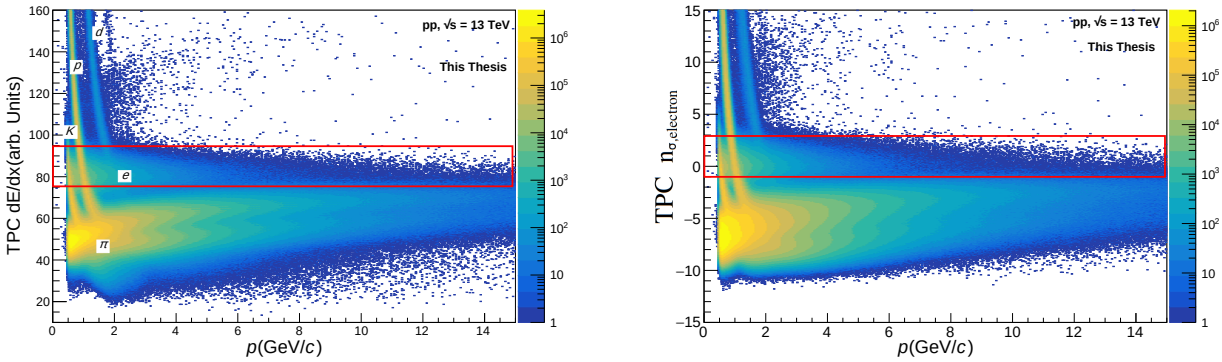

(a) TPC $\mathrm{d}E/\mathrm{d}x$ vs p distribution

(b) TPC $\mathrm{n}_{\sigma,\text{TPC}}$ vs p distribution

Figure 4.1: Electrons in TPC are identified by $\mathrm{d}E/\mathrm{d}x$ measurement and are selected by applying $\mathrm{n}_{\sigma,\text{TPC}}$ cut.

The figure 4.1(b), shows that the bands corresponding to pion, kaon, and proton pass through the electron band in the lower momentum region. On the contrary, in the higher momentum region, these bands merge ($p > 6$ GeV/c). This limits the TPC's capability for particle identification at both lower and higher momentum regions. To achieve high purity electron identification, the selected electron candidate tracks within the TPC are projected onto the surface of the EMCal taking into account the ALICE magnetic field (0.5T). Thus, TPC along with the EMCal is used for electron identification(eID) in the low and high p_{T} regions.

When electrons pass through the EMCal detector they generate an electromagnetic shower and deposit all of their energy in the form of clusters. The total energy E deposited by the

electrons in the EMCal is expected to be equal to their momentum p as measured by the TPC. Therefore, the ratio of the energy deposited in the EMCal to the momentum E/p is approximately 1. Unlike electrons, hadrons do not deposit their entire energy in the EMCal due to their interactions primarily occurring via the strong nuclear force. As a result, the ratio E/p for hadrons is expected to be less than 1. To ensure that the selected clusters are originated from electron showers and not from photons, a p_{T} dependent track-cluster matching cut as per Eq. 4.1 is employed. EMCal clusters are matched to tracks from the TPC, where photons are eliminated, since they do not leave a signal in the TPC [133].

In order to further enhance the purity of the selected electron sample and minimize contamination from hadrons, the parameters describing the shape of the shower created by particles on the surface of the EMCal detector are utilized. The shape of the shower on the EMCal surface can be characterized by an ellipse defined by its long axis (M02) and short axis (M20). A p_{T} -dependent cut is applied to the major axis of the shower shape ellipse [133] to refine the electron sample's purity while ensuring that there is no major impact on the electron selection efficiency. The cuts applied on the long axis of the shower shape ellipse are as follows: 0.05 $\leq$ M02 $\leq$ 0.9 for 3 $<$ p_{T} (GeV/c) $<$ 12, 0.05 $\leq$ M02 $\leq$ 0.7 for 12 $<$ p_{T} (GeV/c) $<$ 20, and 0.05 $\leq$ M02 $\leq$ 0.5 for 12 $<$ p_{T} (GeV/c) $<$ 35. To estimate the residual hadron contamination in each p_{T} bin of the electron sample, the E/p distribution of hadrons is obtained separately by selecting particles with $n_{\sigma,\mathrm{TPC}}$ $<$ -3.5 and M02 cut. It is observed that the majority of the hadron contamination is present in the lower E/p region and the hadron peak moves to the higher E/p region as p_{T} increases. The hadron E/p distribution is scaled to match the electron E/p distribution in the peak region. The scaling region also moves towards the higher E/p with an increase in p_{T} because the hadron peak moves towards higher E/p. Hence, a p_{T} dependent scaling is needed to match the amount of contamination in each p_{T} bin more accurately. The exact M02 cut used for electrons is applied to the hadrons because the hadron E/p does not correctly scale to match the electron E/p distribution. The scaled hadron contribution is subtracted from the E/p distribution of electron candidates, resulting in the E/p distribution of inclusive electrons [27, 178]. The figure 4.2 shows the E/p distribution of electron candidates, scaled hadrons and inclusive electrons obtained from minimum bias(MB) and EMCal triggered EG2 & EG1 data. The figure A.1 shows E/p distribution of the electrons, scaled hadrons and pure electrons in each analysis p_{T} bins obtained from MB, EG2 and EG1 triggered data respectively.

The E/p distribution of electrons shows a peak in the low E/p region(E/p $<$ 1), which are mainly the pions but misidentified as electrons. The height of this peak increases with an increase in p_{T} and becomes more prominent in EG2 and EG1 trigger data. This effect is mainly

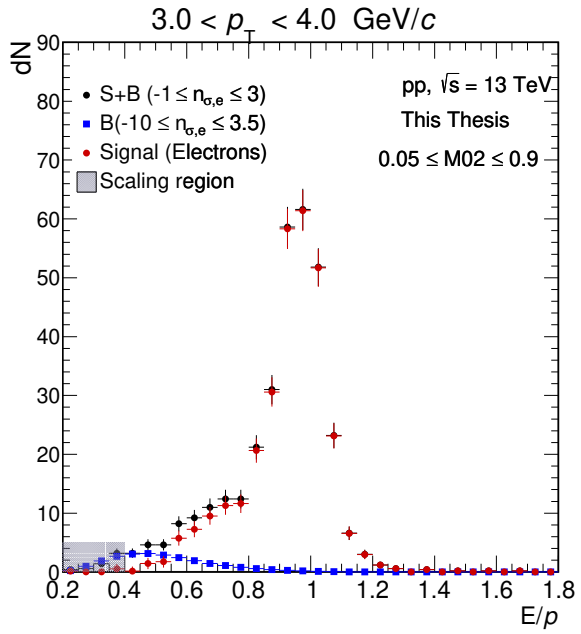

(a) MB trigger

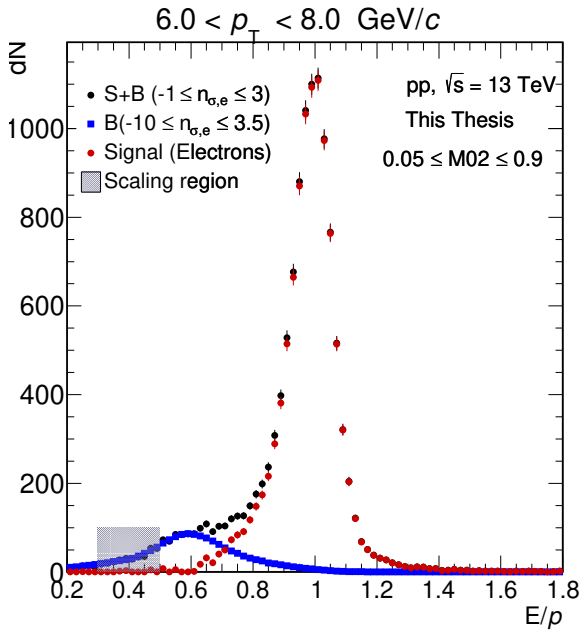

(b) EG2 trigger

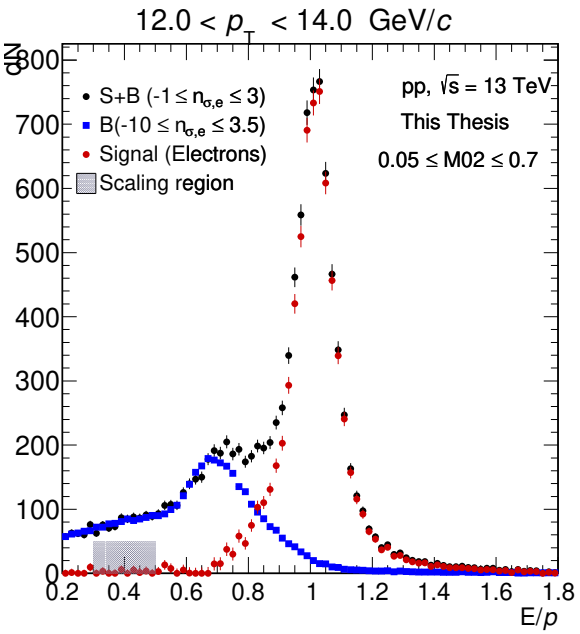

(c) EG1 trigger

Figure 4.2: The black distribution shows the E/p of electron candidates obtained after electron identification cuts. The blue distribution shows the estimated hadron contamination obtained after scaling the hadron E/p to match the electron E/p and the shaded portion represents the scaling region. The red distribution shows E/p of pure electrons obtained after subtracting the hadron contamination (blue) from electron candidates (black) in their respective p_{T} bins of MB, EG2 and EG1 triggered events.

because of the $n_{\sigma,\mathrm{TPC}}$ cut; as we move toward the higher p_{T} , the electron band starts merging with other hadrons, and therefore, the cut -1 to 3 on $n_{\sigma,\mathrm{TPC}}$ also selects these hadron tracks.

The smallest distance between the reconstructed track and the reconstructed primary vertex in (XY) plane perpendicular to the (Z) beam axis is called the impact parameter (d_0) or distance of closest approach (DCA) [179]. For this analysis, electrons and positrons are treated

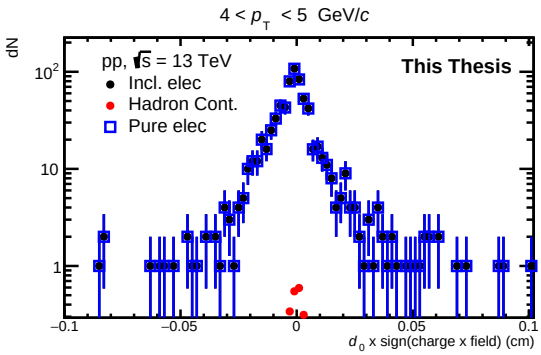

(a) MB trigger

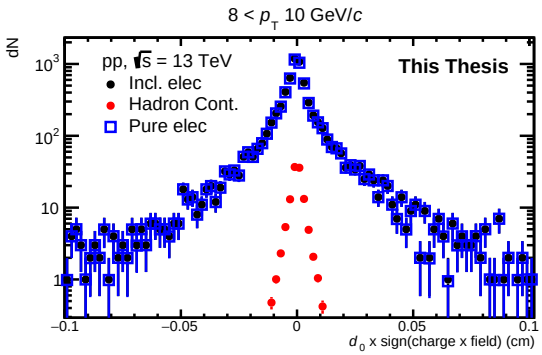

(b) EG2 trigger

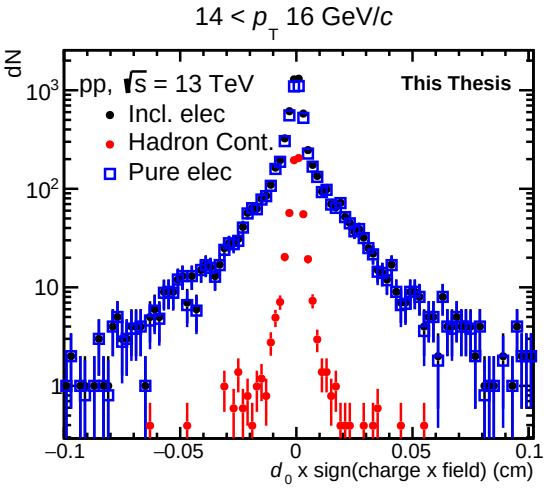

(c) EG1 trigger

Figure 4.3: The black distribution shows d_0 of electron candidates obtained after electron identification cuts. The red distribution shows the d_0 of estimated hadron contamination. The blue distribution represents d_0 of pure electrons obtained after subtracting the hadron contamination (red) from electron candidates (black) in their respective p_{T} bins of MB, EG2 and EG1 triggered events.

identically, differing only in the charge factor multiplied to the . The d_0 distribution of particles, satisfying the conditions of $0.85 < \mathrm{E}/p < 1.2$ and passing the M02 cut, within the range of $-1 \leq \mathrm{n}_{\sigma,\mathrm{TPC}} \leq 3$ provides the inclusive electron d_0 distribution in each p_{T} bin. Similarly, the d_0 distribution of particles passing the same E/p and M02 cut, but with $\mathrm{n}_{\sigma,\mathrm{TPC}} < -3.5$, provides the hadron d_0 distribution for each p_{T} bin. To account for contamination, the d_0 distribution of the hadrons is scaled to match the level of contamination observed in the scaled E/p distribution of hadrons within individual p_{T} bins. The scaled hadron DCA is subtracted from the inclusive electron DCA to get the pure electron DCA distribution. The electron and hadron identification (eID and hID) cuts are summarized in table 4.3.

Table 4.3: Selection criteria for electron and hadron candidates

Track Cut	Electron Selection Value	Hadron Selection Value
$n_{\sigma,TPC}$	$-1 \leq n_{\sigma,TPC} \leq 3$	$-10 \leq n_{\sigma,TPC} \leq -3.5$
E/p	$0.85 \leq E/p \leq 1.20$	Varied between the range
M02	$0.05 \leq M02 \leq 0.9$ $(3 < p_T\ (GeV/c) < 12\ )$ $0.05 \leq M02 \leq 0.7$ $(12 < p_T\ (GeV/c) < 20)$ $0.05 \leq M02 \leq 0.5$ $(20 < p_T\ (GeV/c) < 35)$	same as electron

4.4 Identification of non-heavy-flavour electrons

The electron sample obtained after removing the hadron contamination is called an inclusive electron sample. The subsequent task involves identifying electrons originating from beauty-hadron decays. Due to the undetectable neutrino in the semi-electroinc decay channel, it is impossible to identify the source of the electron directly. Therefore, a data-driven approach is employed to isolate electrons originating from heavy-flavour decays. In this approach, background electrons (non-HFe) are estimated using an indirect technique and subtracted from the inclusive electron sample, leaving us with electrons originating from heavy-flavour decays. The sources of non-HFe are the following:

1. Dalitz decay, i.e. electrons from decay of light neutral meson (π^0 and η)
2. electrons from photon conversion in the detector material
3. electrons from dielectron decays of light vector mesons (ω, ρ, ϕ)
4. electrons from dielectron decay of heavy quarkonia
5. electrons from weak $K \rightarrow e\pi\mu\,(K_{e3})$ decays and dielectron decays of light vector mesons
6. electrons originating from partonic hard scattering processes (Drell-Yan processes and prompt photon production)

The dominant background of non-HFe in the detector arises from the Dalitz decay of light neutral mesons (π^0 and η) and the conversion of photons to electrons in the detector material. Electrons from both sources are collectively referred to as photonic electrons. The electrons from the rest of the sources have a negligible contribution. However, the electrons from $W^{\pm}$ and Z boson decays contribute to the background, especially at the higher p_T range. The total contribution of W/Z decay electron has been calculated using PYTHIA+POWHEG simulation in reference [178] and is found to be negligible for $p_T < 20$ GeV/c. In the present study,

the contribution of W/Z decay electron needs to be addressed, and its contribution shall be included later. The photonic electrons have an essential feature that they are always created in electron-positron(e^-e^+) pairs, while the electron coming from HF decays will be single electron or positrion. Therefore, the invariant mass of e^-e^+ pairs coming from photonic electrons will peak at low invariant mass and on the other hand, no such peak must be observed for HF decays. The photonic electrons are identified by the following procedure:

- An invariant mass spectrum of all unlike sign (ULS) paired electrons (e^-, e^+) from the inclusive electron sample gives the correlated pairs, i.e. electrons from actual photonic decays and random uncorrelated pairs
- Similar to ULS pair an invariant mass spectrum of all like sign (LS) paired electrons (e^+, e^+) and (e^-, e^-) from the inclusive electron gives random uncorrelated pairs (combinatorial background)
- To reject the electrons from photon conversion, a cut of invariant mass $M_{\rm inv} < 0.14\,{\rm GeV}/c^2$ is applied on ULS and LS electron pairs as shown in Fig. 4.4
- The non-HFe can be obtained by subtracting the like sign paired electrons from unlike sign sample, $\mathrm{N}^{\mathrm{non-HFe}} = \mathrm{N}^{\mathrm{ULS}} - \mathrm{N}^{\mathrm{LS}}$

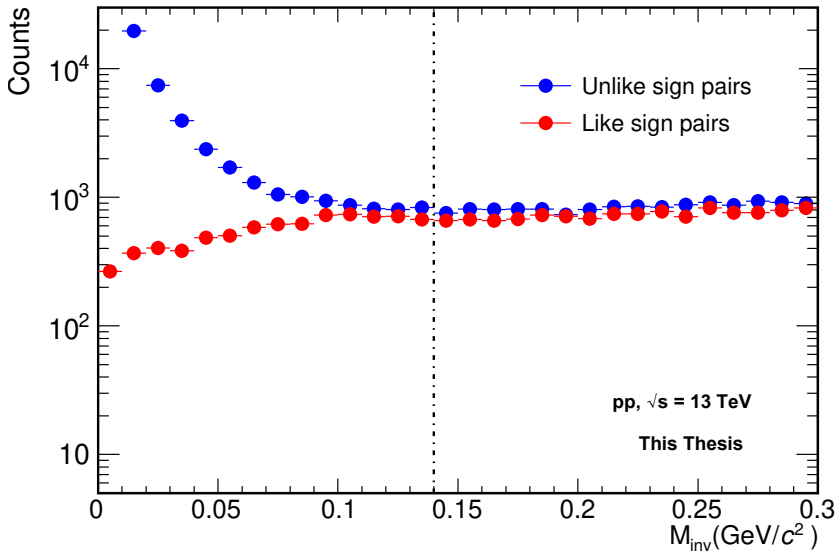

Figure 4.4: The invariant mass distribution for ULS and LS electron pairs selected within $M_{\rm inv} < 0.14{\rm GeV}/c^2$.

In the described procedure, the electron identification criteria are applied to tag one of the $e^{\pm}$ tracks orignating from the primary collision vertex. Subsequently, all remaining tracks within the same event are examined to identify the partner (associate) electron. The tracks

passing filter mask `AliAODTrack::kTrkTPCOnly` are taken into account for potential partner electrons. To maximize the probability of finding the associated partner track, a series of loose cuts are applied as outlined in in table 4.4.

Table 4.4: Selection criteria for associated electron track

Track Cut	**Selection Value**
FilterBit	`AliAODTrack::kTrkTPCOnly`
associated electron p_{T}	≥ 0.1 GeV/c
$\lvert\eta\rvert$	0.8
Number of TPC Clusters for tracking	≥ 60
Number of TPC Clusters for PID	≥ 60
ITS and TPC refit	Required
DCA_{xy}	≤ 1 cm
DCA_{z}	≤ 2 cm
χ^2 clusters of the momentum fit in the TPC	4
$\mathrm{n}_{\sigma,\mathrm{TPC}}$	$-3.5 \leq \mathrm{n}_{\sigma,\mathrm{TPC}} \leq 3.5$

4.4.1 non-HFe tagging efficiency

All the photonic electrons may not be identified using the invariant mass method because there might be instances of photonic (e^+, e^+) pairs where the corresponding partner electron either falls outside the detector's acceptance or fails to meet the necessary thresholds or slection criteria. Therefore, it becomes necessary to correct the count of non-HFe identified through the invariant mass method by applying the non-HFe tagging efficiency ($\epsilon_{tagg}^{non-HFe}$). This approach for estimating photonic electrons is referred to as the photonic electron tagging method. The tagging efficiency is defined as the ratio of the total number of photonic pairs originating from the same mother particle, which are identified after satisfying the partner electron selection criteria, to the total number of photonic electrons in the MC sample.

$$\epsilon_{\mathrm{tagg}}^{\mathrm{non-HFe}} = \frac{\mathrm{N}_{\mathrm{e^+e^-}}^{\mathrm{Found}}}{\mathrm{N}_{\mathrm{e^+e^-}}^{\mathrm{Total}}} \tag{4.3}$$

In this study, the non-HFe enhanced MC samples, subjected to the same selection criteria as the data, have been employed to compute the tagging efficiency. The use of enhanced samples is essential for accurately estimating the tagging efficiency in the higher p_{T} region. However, this introduces a complication: the p_{T} distribution of electrons orignating from enhanced π^0 and η tends to become flat, potentially biasing the efficiency calculation. To rectify this bias, a weighting factor is applied to the p_{T} distribution of electrons originating from enhanced π^0 and η. Figure 4.5 (a) illustrates the p_{T} distribution of π^0 and η from both minimum bias and enhanced events, while Figure 4.5 (b) and (c) depicts the ratio of p_{T} distributions between minimum bias and enhanced samples for π^0 and η respectively. The ratio plots are fitted

using the Hagedorn function, yielding fit parameters that determine the weight. This weight is subsequently applied to the daughter electrons based on the p_{T} of their enhanced mother particles (π^0 and η). The photonic electron sources considered in the analysis are:

$$\begin{aligned} \eta &\to e^+e^- \\ \eta \to \pi^0 &\to e^+e^- \\ \eta \to \gamma &\to e^+e^- \\ \eta \to \pi^0 \to \gamma &\to e^+e^- \\ \pi^0 &\to e^+e^- \\ \pi^0 \to \gamma &\to e^+e^- \end{aligned} \tag{4.4}$$

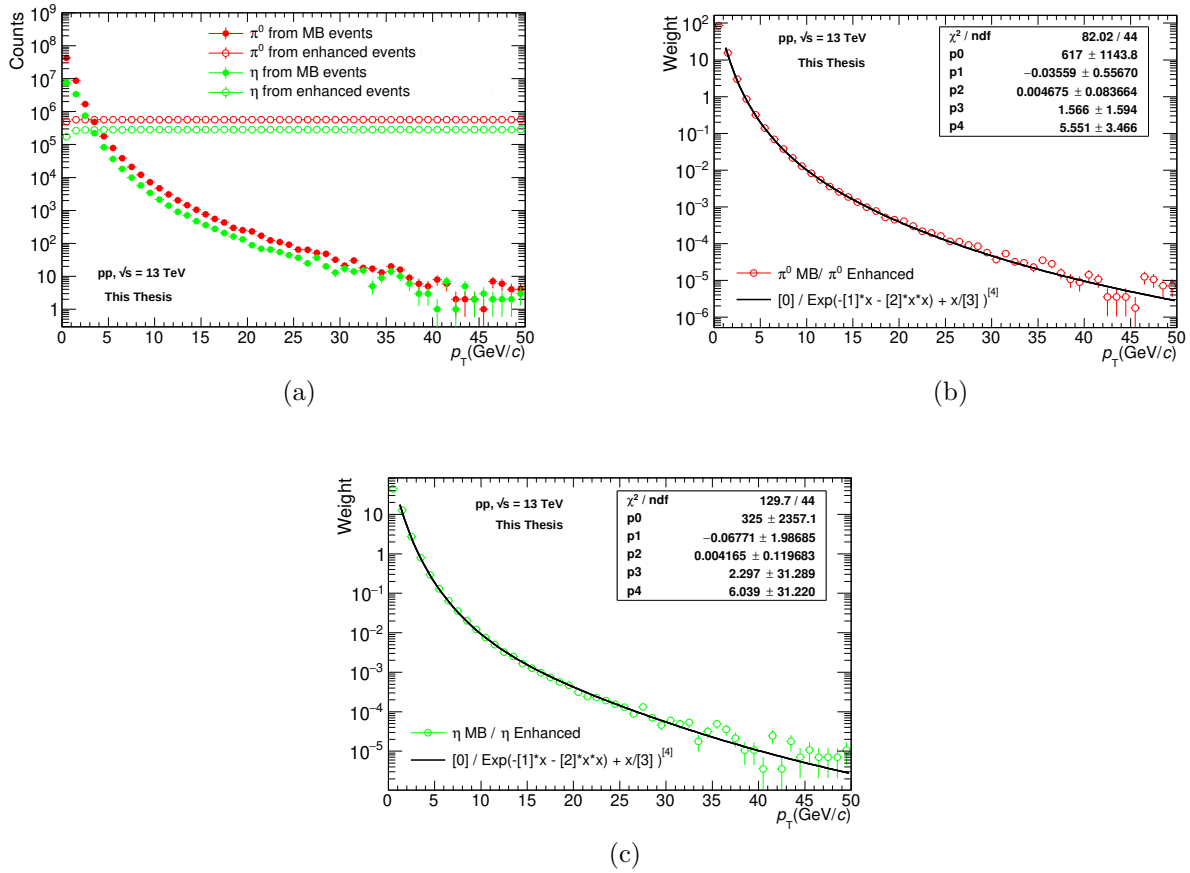

Figure 4.5: Figure (a) shows the p_{T} distribution of π^0 and η from both minimum bias (closed markers) events and embedded events (open markers) in the MC sample. Figure (b) and (c) illustrate the ratio of p_{T} distribution of minimum bias to enhanced events for π^0 and η, respectively, fitted with a Hagedorn function.

The p_{T} spectrum of the electrons originating from enhanced π^0 and η in MC, which combine to form an unlike-sign pair with an invariant mass less than 0.14 GeV/c^2, constitutes the numerator in the calculation of tagging efficiency. On the other hand, the p_{T} spectrum of

all electrons originating from enhanced π^0 and η, serves as the denominator for the tagging efficiency. The numerator and denominator of the $\epsilon_{tagg}^{non-HFe}$ must pass the track selection criteria in table 4.4. The resulting distribution of tagging efficiency undergoes a smoothing process through the fitting, as demonstrated in Figure 4.6.

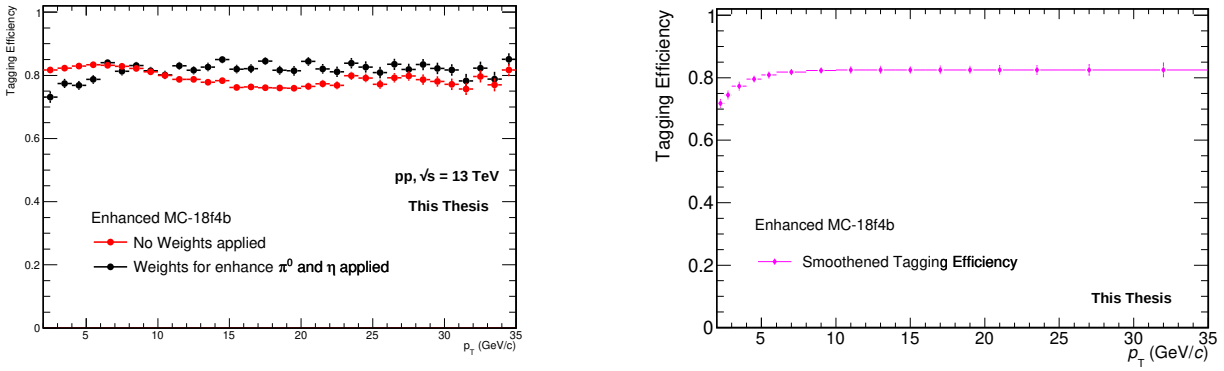

(a) (b)

Figure 4.6: Figure (a) shows the tagging efficiency of non-HFe before (red) and after (black) applying the weight to electrons from π^0 and η. Figure (b) shows the smoothened non-HFe tagging efficiency distribution.

The DCA distributions of the ULS pair and LS pair electron are selected with $m_{e^+e^-} < 0.14$ GeV/c^2. The LS pair DCA distribution is subtracted from the ULS pair DCA, and the resultant DCA is scaled by tagging efficiency to get the corrected DCA distribution of non-heavy-flavour electrons (photonic electron DCA). Finally, the photonic electron DCA is subtracted from pure electron DCA to obtain the HFe DCA distribution as shown in figure 4.8. The raw yield of heavy-flavor decay electrons is obtained by integrating the HFe DCA distribution in their individual p_{T} bins.

The contributions of $e^+ e^-$ pairs from J/ψ and low-mass vector mesons, which constitute other background sources, were considered negligible [180, 181] in comparison to the signal and consequently were not subtracted.

4.4.2 $\mathrm{W}^{\pm}$ and Z^0 boson decay electron contribution

Electrons originating from the decays of $\mathrm{W}^{\pm}$ and Z^0 bosons constitute a substantial background for heavy-flavour hadron decay electrons, particularly at high transverse momenta ($p_{\mathrm{T}} > 20$ GeV/c) [159, 178]. The spectra of electrons from $\mathrm{W}^{\pm}$ and Z^0 decays were computed utilizing the PYTHIA + POWHEG simulation. The W and Z boson production is simulated using POWHEG [182] as the event generator, incorporating next-to-leading-order (NLO) calculations to generate hard events encompassing diverse processes involving a variety of processes with heavy quarks, Higgs bosons, and electroweak bosons. As POWHEG primarily functions as a

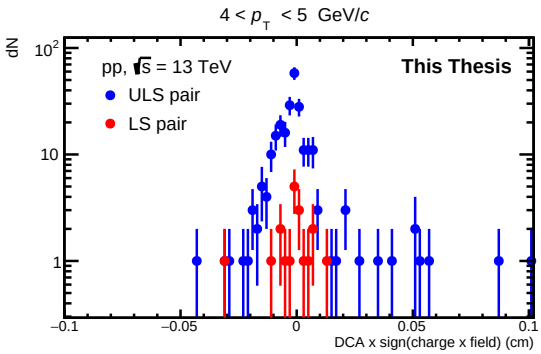

(a) MB trigger

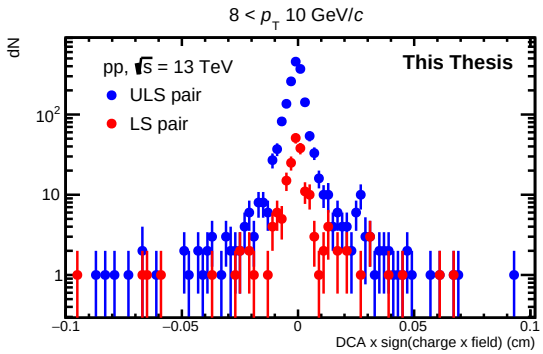

(b) EG2 trigger

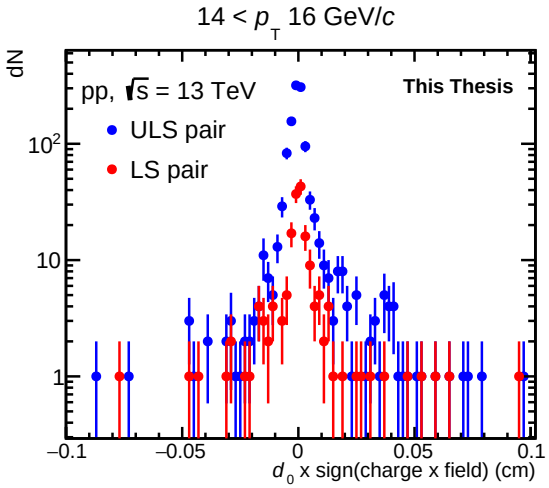

(c) EG1 trigger

Figure 4.7: The blue distribution shows the d_0 of the ULS electron pairs, while the red distribution shows the d_0 of LS electron pairs within the invariant mass selection in their respective p_{T} bins of MB, EG2, and EG1 triggered events.

hard event generator, it is interfaced with PYTHIA [183] for the showering processes in the subsequent stages [159].

Figure 4.9 illustrates the ratio between the $\mathrm{W}^{\pm}$ and Z^{0} boson decays to electrons and the FONLL predictions corresponding to decays from c and b quarks to electrons. The cumulative contribution originating from $\mathrm{W}^{\pm}$ and Z^{0} boson decay electrons exhibits a gradual escalation, starting at 1% for $p_{\mathrm{T}} = 15$ GeV/c and rising to approximately 3% at $p_{\mathrm{T}} = 20$ GeV/c. Notably, it reaches an approximate value of 14% within the p_{T} range of 25 to 30 GeV/c and expands further to around 40% within p_{T} spanning 29 to 35 GeV/c, relative to the yield of electrons arising from heavy-flavour decays [159].

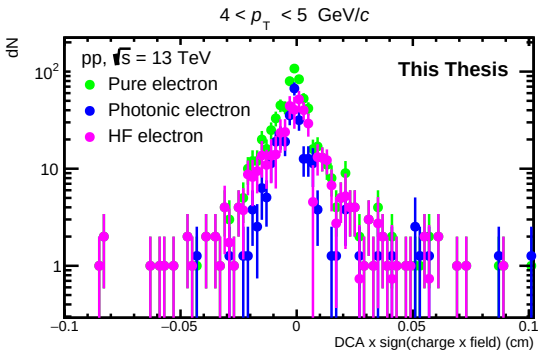

(a) MB trigger

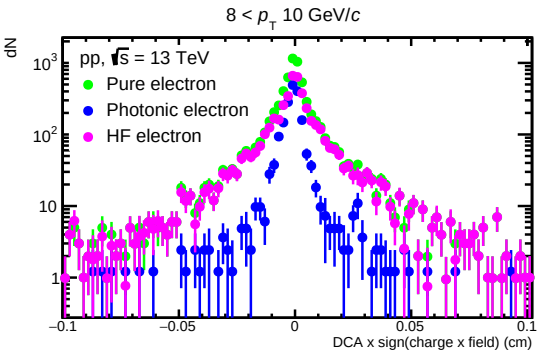

(b) EG2 trigger

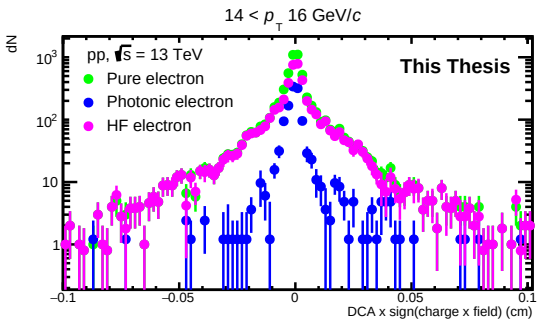

(c) EG1 trigger

Figure 4.8: The green distribution shows the d_0 of the pure electrons, while the blue distribution shows the d_0 of photonic electrons. The magenta distribution represents the d_0 of heavy-flavour decay electrons obtained after subtracting the d_0 of photonic electrons from the pure electrons in their respective p_{T} bins of MB, EG2, and EG1 triggered events.

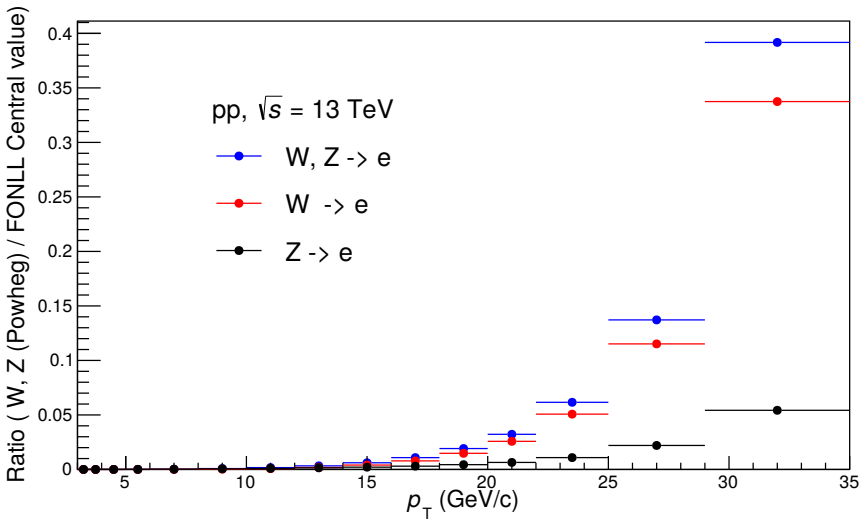

Figure 4.9: The ratio of the p_{T} -differential cross-section of electrons from the decay of $\mathrm{W}^{\pm}$ and Z^{0} bosons to the FONLL central predictions for heavy-flavour decay electrons in proton-proton collisions at $\sqrt{s}$ = 13 TeV [159].

4.5 Diffrentiating electrons from charm and beauty decays

The next step is to separate the electrons from charm and beauty decays to extract the raw beauty decay electron yield from the HFe sample. To differentiate the beauty-decay electrons ($b \to e$ & $b \to c \to e$) from charm-decay electron($c \to e$), the difference in decay length of the two sources is measured indirectly by examining the width of the DCA distribution. Electrons from beauty-hadron decay tend to have a longer lifetime before decay. Because of this, the DCA distribution of beauty-decay electrons becomes wider than that of charm-decay electrons. The decay length of charm and beauty-decay electrons are found to be $c\tau_c \approx 100 - 300\mu m$ and $c\tau_b \approx 500\mu m$ respectively. To extract the raw beauty yield, the HFe-DCA distribution is fitted with charm and beauty-decay electron DCA templates obtained from MC simulation. In the MC simulation, the electrons are identified using the PDG code information, and the templates are created by adding the electrons to their respective templates according to their mother's and grandmother's particle ID.

4.5.1 Corrections to MC template

The charm and beauty-decay electron templates are obtained from MC simulations, but it is known that MC simulations do not perfectly reproduce the same results as those found in the actual data. The MC sample used in this analysis is a heavy-flavour enhanced sample, which means that the MC used in constructing the templates already has some bias due to the enhancement. To eliminate these biases and make the MC DCA templates as close as possible to the DCA distributions that would be observed in the data, the following corrections are applied.

(a) DCA mean and resolution correction

The mean and resolution of the DCA distributions in the data do not match those in the MC simulations. Specifically, the mean of the DCA is slightly shifted towards negative values at low p_{T} in ALICE run-2 data. The current understanding is that this shift is due to the misalignment of SPD modules during data acquisition. Moreover, the shift depends on the azimuthal angle and polarity of the magnetic field, factors that are not accounted for in the MC simulations. Additionally, the resolution of the DCA distributions differs between the data and MC simulations. The mean shift and resolution difference between the data and MC DCA distributions is corrected using the improver task developed by the D2h group [175]

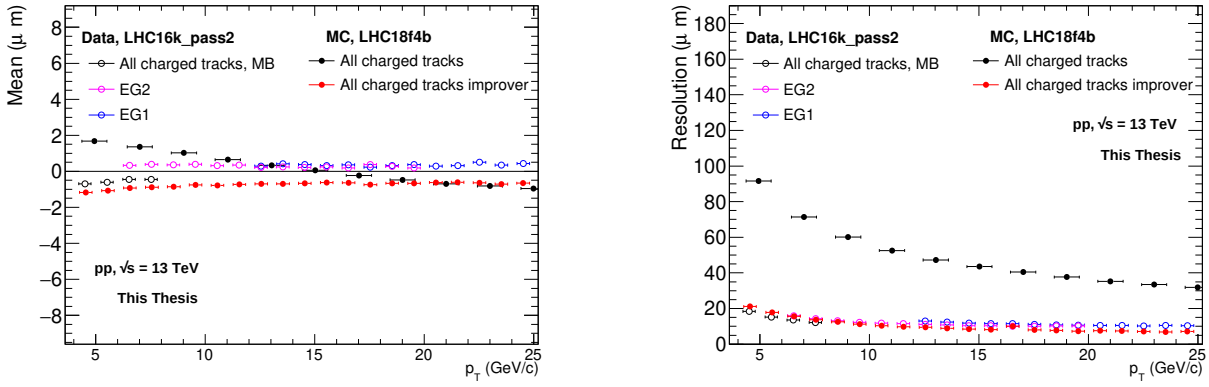

(a) (b)

Figure 4.10: Figure (a) shows the mean of DCA in data (open markers) and MC for all charge particle tracks before (black) and after (red) improver correction. Figure (b) shows the resolution of DCA in data (open markers) and MC for all charge particle tracks before (black) and after (red) improver correction.

Figure 4.10 compares the DCA mean and resolution before and after applying the improver corrections to the MC templates. When comparing the corrected DCA mean between the data and MC, we observe a difference of approximately 0.5 μm in the first three p_{T} bins and a constant difference of $\sim$ 1 μm in the remaining p_{T} bins. However, since the differences are minimal, the mean was sufficiently corrected for this analysis. Similarly, after implementing the improver correction, the DCA resolution in the MC simulations also aligns well with the data.

(b) D meson p_{T} spectrum correction

The d_0 distribution depends on the momentum of electron sources; therefore, it is necessary to correct the p_{T} distribution of the electron mother. The p_{T} spectrum of D mesons in the MC simulation is harder due to the heavy-flavour enhanced sample, which leads to a discrepancy with the data. Consequently, this causes the DCA of D mesons to differ between the MC and data. The strategy for dealing with the charm case involves utilizing the measured spectrum of D^0 mesons. Figure 4.11, shows the D^0 spectrum measured in pp collisions at $\sqrt{s}$ = 13 TeV [184] compared to the simulated D^0 p_{T} distribution. Both distributions are fitted using the Tsallis distribution. The ratio of these distributions is then compared with the ratio of the fitted functions, shown in Figure 4.11 (b), and they appear to be in good agreement. Hence, the correction factor applied to the D^0 meson seems appropriate for other D mesons like $D^{\pm}$ or $D_s^{\pm}$, as both p_{T} spectra closely resemble that of D^0 for pp collisions at $\sqrt{s}$ = 13 TeV[185]. As a result, the impact of a very minor influence can be disregarded, considering the uncertainties in the correction estimation. Therefore, the same weighting factor is employed for all D mesons.

Using a weighting method for charm hadrons would introduce a non-Poissonian distribution. To overcome this, a statistical correction method was adopted. The weight was set to 1 at the start of the lowest p_{T} interval, and electrons from charm hadron decays were then filtered out with a probability of $1 - \mathrm{w_D}$. This process rectifies the charm hadron p_{T} distribution while maintaining Poissonian statistics [96].

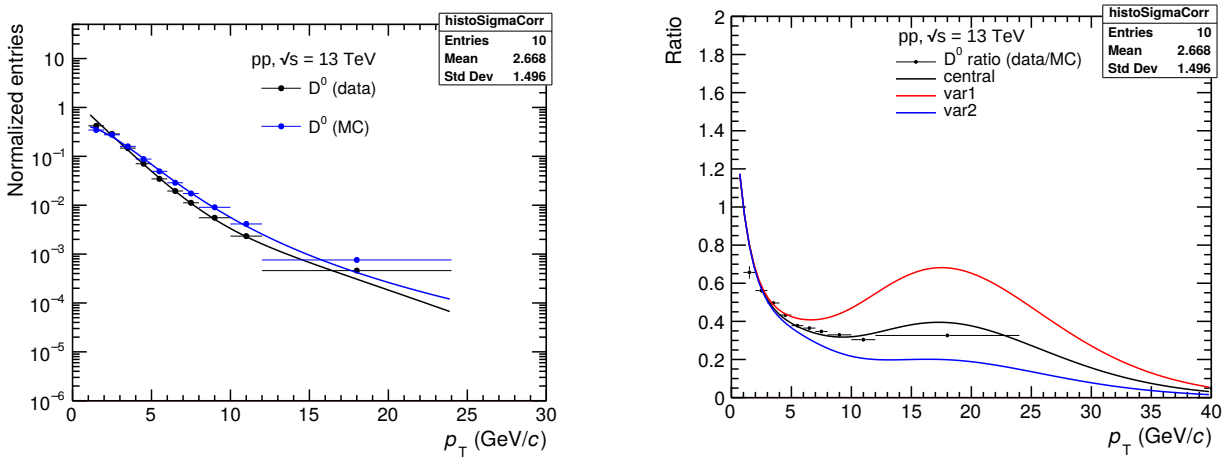

(a) (b)

Figure 4.11: (a) The p_{T} spectra of D^0 meson estimated from MC (blue) and measured from data (black) in proton–proton collisions at $\sqrt{s}$ = 13 TeV. (b) Illustrates the weighting factor utilized to correct electrons mother i.e. D mesons p_{T} spectra [96].

(c) B meson p_{T} spectrum correction

A similar correction is performed for B mesons to ensure that the p_{T} spectrum of B mesons considered in MC has the correct p_{T} shape. However, as no experimental data is available for the B meson p_{T} spectrum at pp 13 TeV, the central values of FONLL predictions are used to correct the shape of the B meson p_{T} spectrum in MC. The FONLL to MC p_{T} spectra ratio is employed as a weight to correct the B meson p_{T} spectrum in MC. Figure 4.12(a) shows the p_{T} spectrum of B mesons measured in MC (red) and FONLL predictions (green), while (b) shows the ratio spectra of FONLL central/MC, FONLL minimum/MC, and FONLL maximum/MC. The central red distribution is utilized as a weighting factor and applied to electrons for correcting the electron's mother, i.e., B mesons p_{T} spectra.

(d) Corrections to the proportion between charmed baryons and mesons

In the construction of MC templates of electrons orignating from heavy-flavour hadron decays, a mix set of signals from various hadron species is taken into account. Since beauty hadrons exhibit similar decay lengths and have not been subject to measurement, any correction for the yields of different beauty hadrons is both unnecessary and unfeasible. However, the ALICE

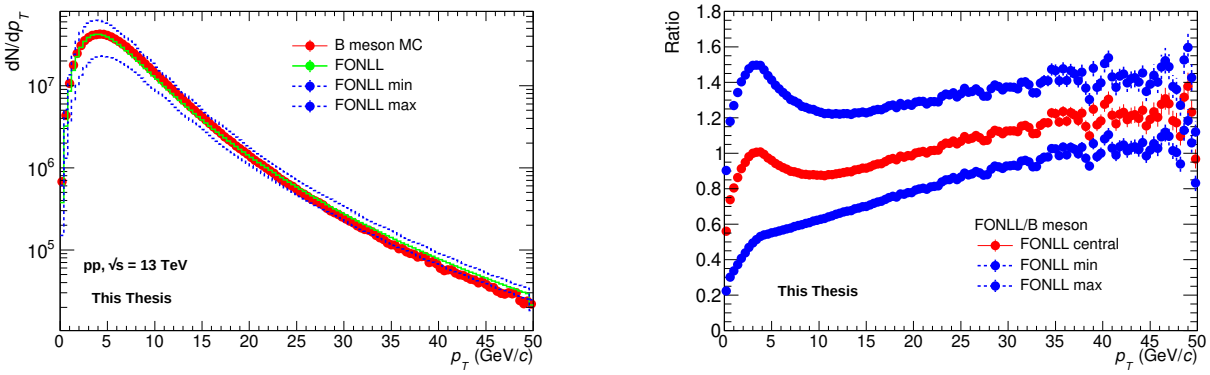

(a) B meson p_{T} spectrum (b) Ratio

Figure 4.12: (a) The p_{T} spectra of B mesons from the MC simulations (red) and FONLL predictions, i.e., central (green) and the associated uncertainties (blue). (b) The ratio of the FONLL predictions to the estimated MC distribution.

collaboration has measured several charm hadrons, revealing considerable variations in their decay lengths. Therefore, it is crucial to make adjustments based on these explicit measurements. The charm-decay electron template is estimated by incorporating contributions from charmed baryons and mesons, including D^0 , $D^{\pm}$, $D_s^{\pm}$, and Λ_c^+ . After correcting the mother transverse momentum (p_{T}) spectra of electrons originating from D mesons, it becomes apparent that the contributions of $D^{\pm}$ $/D^0$ and $D_s^{\pm}$ $/D^0$ are corrected, as these species have similar decay lengths [68, 186]. However, the Λ_c^+ baryon, characterized by its shorter decay length, results in a narrower distribution of impact parameters (DCA) among the measured D meson species(refer table 4.5). Additionally, the shape of the Λ_c^+ spectrum differs from that of D^0 . Consequently, the measured Λ_c^+ $/D^0$ ratio in the data exhibits p_{T} dependence, while the fractions of other mesons remain constant for p_{T} [185], such as ($D^{\pm}$ $/D^0$) being approximately 0.5 and ($D_s^{\pm}$ $/D^0$) approximately 0.25 as shown in the Figures 4.13.

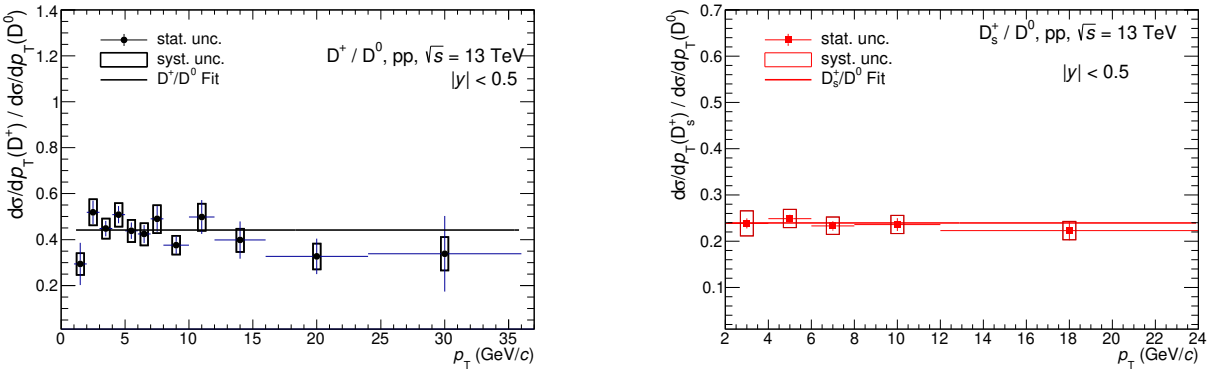

(a) (b)

Figure 4.13: The fraction of $D^{\pm}$ $/D^0$ and $D_s^{\pm}$ $/D^0$ measured in proton–proton collisions at $\sqrt{s}$ = 13 TeV, fitted with a constant function.

In Figure 4.14 (a), a comparative analysis of the Λ_c^+ to D^0 ratio is presented, comparing

data to the MC simulation. It is worth noting that the branching ratio (B.R.) is accounted for in the data analysis due to the measurements being conducted at the hadronic level. At the same time, the simulation is performed at the electron level. The MC sample underestimates the Λ_c^+ /D^0 ratio, prompting the scaling of Λ_c^+ /D^0 in the simulation by factors of 2 and 3. The data is intermediate concerning these scaling factors, aligning with the branching ratio consideration. Considering the energy loss during the decay from mother particle to daughter, it is expected that the electron-level ratio should shift towards lower values. As a result, the central correction involves scaling by a factor of 2, while factors of 3 and no scaling distributions will be utilized to estimate the systematic effects. In Figure 4.14 (b), the I.P. distribution of electrons originating from D mesons is shown, along with contributions from single and double (scaled by factor 2) Λ_c^+ baryon decays after correcting for the mother p_{T} .

Table 4.5: Summary table representing the properties of hadrons carrying open heavy-flavor with charm or bottom quarks. Given are the valence quark content, the hadron mass and their decay length.

Particle	**Quark content**	**Mass (GeV/c^2)**	$c\tau$ **(μm)**
D^+	c$\bar{d}$	1.8696 ± 0.0002	312 ± 2
D^0	c$\bar{u}$	1.8648 ± 0.0001	123 ± 1
D_s^+	c$\bar{s}$	1.9685 ± 0.0003	150 ± 2
$\Lambda_c^\pm$	udc	2.2865 ± 0.0001	60 ± 2
B^+	u$\bar{b}$	5.2792 ± 0.0003	492 ± 2
B^0	d$\bar{b}$	5.2795 ± 0.0003	455 ± 2
B_s^0	s$\bar{b}$	5.3663 ± 0.0006	441 ± 8

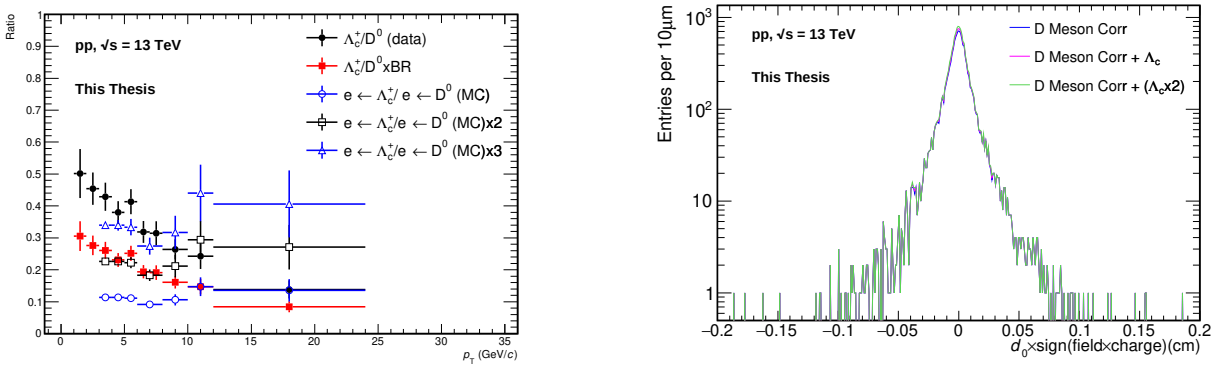

(a) (b)

Figure 4.14: (a): Comparison of the Λ_c^+ /D^0 ratio between data and MC in proton-proton collisions at $\sqrt{s}$ = 13 TeV. (b) Comparison of the charm-decay electron templates after correcting for the electron mother p_{T} spectrum and Λ_c^+ /D^0 fraction in MC.

Figure 4.15 compares the d_0 distributions of electrons originating from charm and beauty hadron decays. Notably, electrons from beauty hadron decays ($b \to (c \to) e$) exhibit a wider d_0 distribution when contrasted with those from charm hadron decays ($c \to e$) at the same p_{T} .

The black and red colours represent the d_0 distributions before applying mother p_{T} corrections to the beauty hadron decay electron ($b \rightarrow (c \rightarrow) e$) template. Interestingly, applying these corrections to the $b \rightarrow (c \rightarrow) e$ does not result in significant changes. However, in the case of the charm hadron decay electron ($c \rightarrow e$) template, the overall template becomes narrower after applying template corrections.

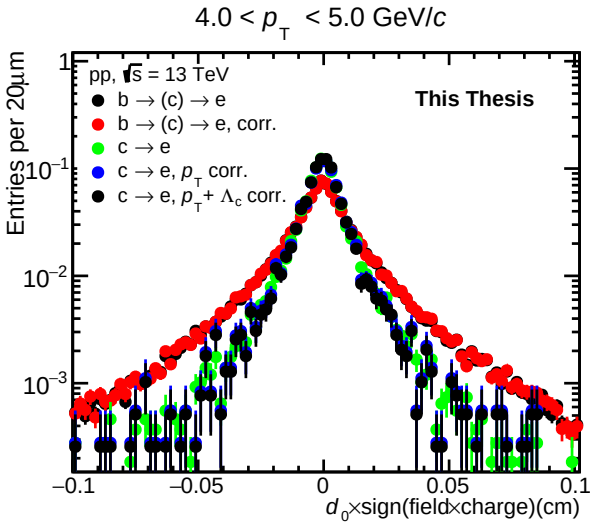

Figure 4.15: The d_0 distributions of electrons originating from charm and beauty hadron decays before and after applying the template corrections.

4.5.2 Template fitting procedure

The corrected $b \rightarrow (c \rightarrow) e$ and $c \rightarrow e$ templates are first normalized to unity, then fitted to the data (HFe DCA) using a likelihood fit approach to extract the raw $b \rightarrow (c \rightarrow) e$ yields in each p_{T} bin [187]. This method will be called the "Two-Template" fit method throughout the text [27]. It is important to note that likelihood fits used to extract the yield require that the data to which the templates are being fitted must adhere to Poissonian statistics. Recall that the HFe d_0 distribution was estimated by subtracting the contributions from hadron contamination and photonic electrons from the d_0 distribution of inclusive electrons. The data-driven method used to calculate the HFe DCA may introduce some uncertainties in assuming Poissonian statistics in the HFe d_0 distribution, a prerequisite for the likelihood fits. To address this concern, the weighted log-likelihood option "WL" is employed to fit the charm and beauty templates to HFe DCA [27].

To ensure the accuracy of the extracted $b \rightarrow (c \rightarrow) e$ yield, a double-check is performed by extracting the raw beauty yield using the "Four-Template" fit method. In this approach, the d_0 distributions of hadron contamination and photonic electrons are not subtracted from the inclusive electrons. Instead, they are utilized as templates and fitted to the inclusive electron

DCA using the log-likelihood fit "L" option, allowing for the extraction of the raw $b \to (c \to) e$ yield. It is important to note that the d_0 distributions of the hadron contamination and photonic electrons are obtained from the data. In contrast, the templates for beauty and charm decay electrons are sourced from Monte Carlo simulations [24].

1. **Two-Template fit method**

   In this method, the templates for electrons originating from charm and beauty-decay processes are subjected to a log-likelihood fit against the HFe DCA. The specific functional form employed for fitting the data is given by equation 4.7

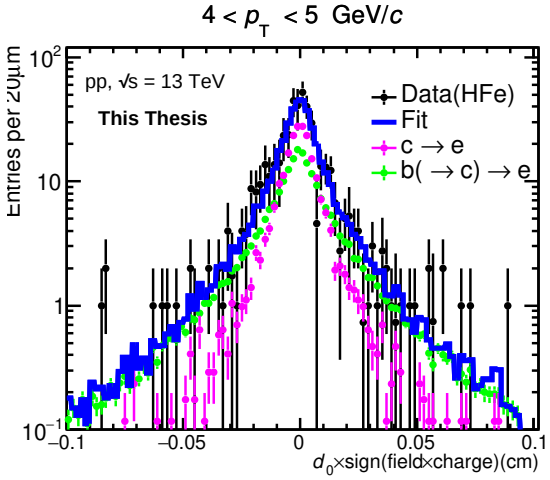

(a) MB trigger

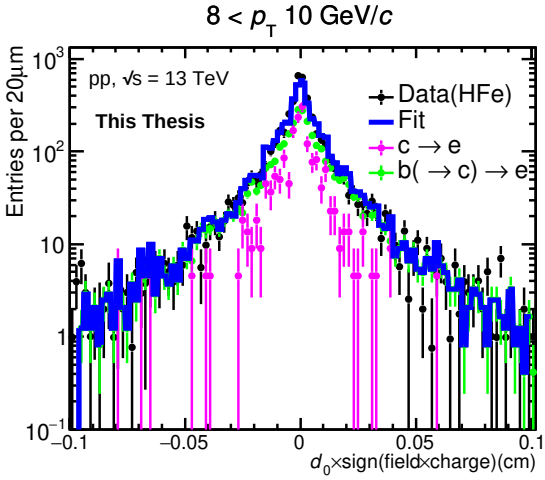

(b) EG2 trigger

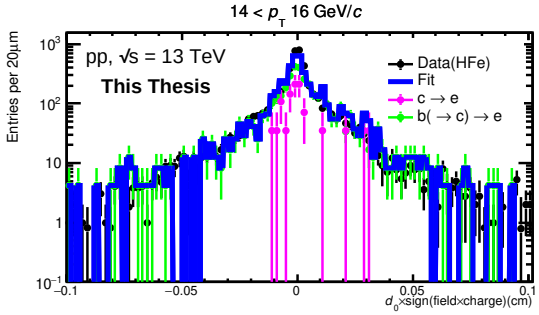

(c) EG1 trigger

Figure 4.16: The DCA distribution of heavy-flavor electron (black) fitted with charm (magenta) and beauty-decay electron (green) templates using a weighted log-likelihood fit option in their respective p_{T} bins of MB, EG2, and EG1 triggered events.

$$fit = p_0.d_0^{b\to(c\to)e} + p_1.d_0^{c\to e} \tag{4.5}$$

The fit function has two free parameters, denoted as p_0 and p_1, which provide the raw yields of beauty and charm-decay electrons, respectively. However, it is imperative to note that the total count of heavy-flavor electrons, represented as N_{HFe}, in a given sample

must equal the sum of electrons originating from charm and beauty decay processes. The quantity of heavy-flavour electrons within a specific p_{T} bin is determined by integrating the d_0 distribution of heavy-flavor electron.

$$\therefore \qquad N_{HFe} = p_0 + p_1 \tag{4.6}$$

With the above constraint, Eqn. 4.5 can be reformulated as

$$fit = p_0.d_0^{b\to(c\to)e} + (N_{HFe} - p_0).d_0^{c\to e} \tag{4.7}$$

The fitting procedure is repeated for each transverse momentum bin within the range 2 $\leq p_{\mathrm{T}}$ (GeV/c) $\leq$ 35 to obtain the raw $b \to (c \to) e$ yield.

2. **Four-Template fit method**

To avoid any potential biases in measuring the beauty-decay electron yield from the data-driven procedure employed for estimating HFe DCA in the two-template fit method, we utilize the scaled hadron DCA and photonic electron DCA derived from the data. These, along with the charm and beauty-decay electron Monte Carlo templates, are employed in fitting the inclusive electron DCA. In this method, we directly fit these data and MC templates to the inclusive electron DCA instead of the HFe DCA, thereby still validating the underlying assumption of Poissonian statistics in the templates. The log-likelihood fit option "L" is adequate for extracting the raw yield of beauty-decay electrons. The fitting function utilized in this method is defined by Eqn. 4.8.

$$fit = p_0.d_0^{b\to(c\to)e} + p_1.d_0^{c\to e} + p_2.d_0^{Hadron} + p_3.d_0^{Photonic} \tag{4.8}$$

The fit function has two free parameters, denoted as p_0 and p_1. The other two parameters, p_2 and p_3, are held fixed because the d_0 distributions of hadron contamination and photonic electrons were already estimated from the data. The integrals of these distributions provide the yields, which are used to determine the fixed values of p_2 and p_3, respectively, in each p_{T} bin. The parameters p_0 and p_1 represent the yields of electrons originating from charm and beauty hadron decays.

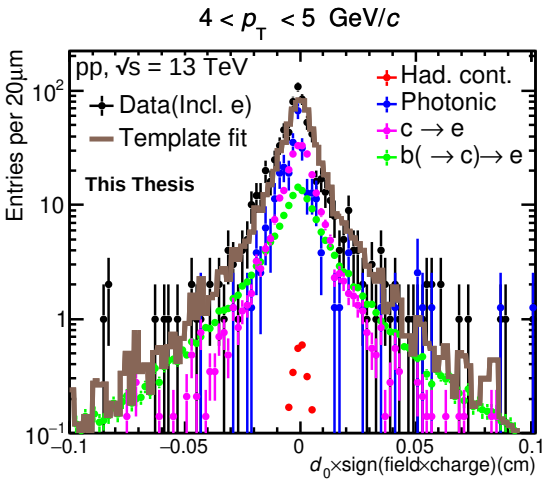

(a) MB trigger

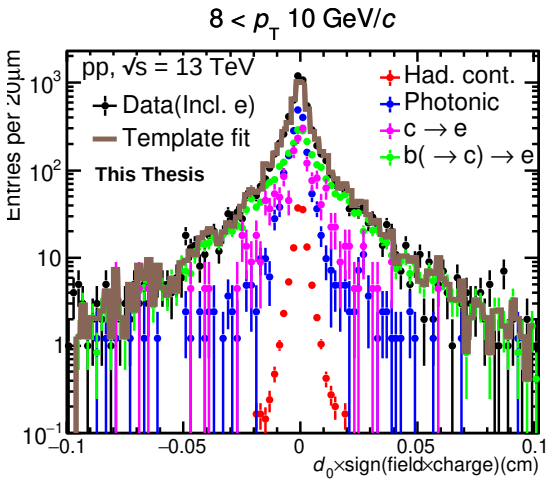

(b) EG2 trigger

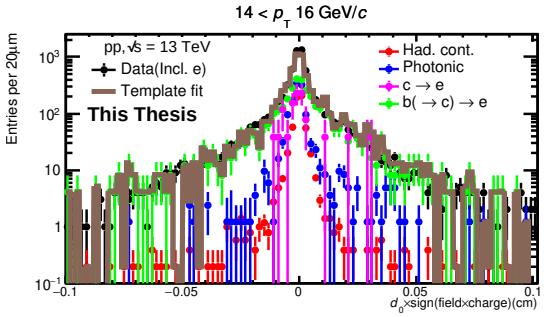

(c) EG1 trigger

Figure 4.17: The inclusive electron DCA distribution (black) fitted with hadronic (red), photonic electron (blue), charm (magenta), and beauty-decay electron (green) templates using a log-likelihood fit option in their respective p_{T} bins of MB, EG2, and EG1 triggered events.

4.6 EMCal trigger rejection factor

To select an electron-rich sample in the intermediate and higher p_{T} regions with sufficient statistics, we utilize events triggered by the EMCal, specifically EG2 and EG1, in addition to minimum bias triggered events. EG1 and EG2 are EMCal gamma triggers with threshold values set at 10.5 GeV and 4.5 GeV, respectively. While triggered events augment electron statistics at higher p_{T} , they introduce a bias at the cluster energy level. Consequently, the raw beauty yield measured with EG2 and EG1 triggered events is observed to be significantly higher than in minimum bias events. To rectify this, the beauty yield measured with EG2 and EG1 events must be scaled by the trigger rejection factor to align them with minimum bias events. The trigger rejection factor is computed by taking the ratio of the cluster energy distribution of triggered events (EG2 or EG1) to that of minimum bias events [19]. The ratio ($\mathrm{E}_{\mathrm{EG2}}^{\mathrm{Cluster}}/\mathrm{E}_{\mathrm{MB}}^{\mathrm{Cluster}}$) and ($\mathrm{E}_{\mathrm{EG1}}^{\mathrm{Cluster}}/\mathrm{E}_{\mathrm{MB}}^{\mathrm{Cluster}}$) is then fitted with equation 4.9. The rejection factor is chosen to be the value of the fit function where the distribution is nearly flat as shown in Fig. 4.18. To avoid fluctuations at higher p_{T} , the rejection factor for EG1 triggers is calculated

using Eqn. 4.10.

$$fit\ function = p_0 + \frac{p_1}{1 + e^{-(x-p_2)/p_3}} \tag{4.9}$$

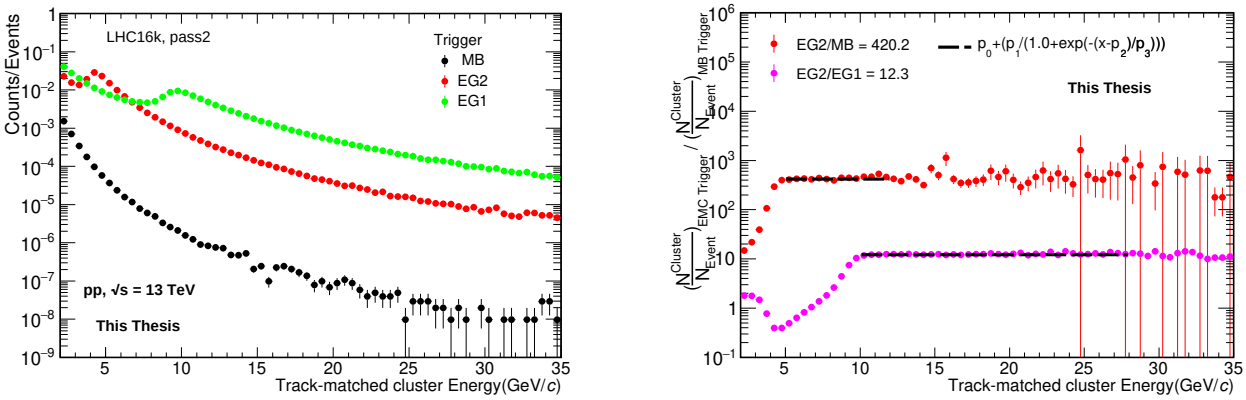

(a) (b)

Figure 4.18: (a): The distribution of EMCal cluster energy for minimum bias events (black) and EMCal triggered events EG2 (red) and EG1 (green). (b): The ratios ($E^{Cluster}_{EG2}/E^{Cluster}_{MB}$) and ($E^{Cluster}_{EG2}/E^{Cluster}_{EG1}$) are fitted with equation 4.9 to estimate the trigger rejection factors.

$$RF_{EG2} = \frac{f^{cl}_{EG2}}{f^{cl}_{MB}} \quad \text{and} \quad RF_{EG1} = \frac{f^{cl}_{EG1}}{f^{cl}_{MB}} = \frac{f^{cl}_{EG1}}{f^{cl}_{EG2}}.\frac{f^{cl}_{EG2}}{f^{cl}_{MB}} = \frac{f^{cl}_{EG1}}{f^{cl}_{EG2}}.RF_{EG2} \tag{4.10}$$

Table 4.6: Summary of EMCal trigger rejection factor

period	RF_{EG2}	RF_{EG1}
LHC16k	420	5168
LHC18	398	4739

4.7 Measured electron yields from heavy-flavor and beauty-hadron decays

Figure A.4 shows the d_0 distribution of heavy-flavor decay electrons within various transverse momentum intervals ranging from $2 < p_T$ (GeV/c) < 35. The integral of the HF electron d_0 distribution provides the raw yield of heavy-flavor electrons in the respective p_T intervals. Figure 4.19 (a) shows the estimated raw HF electron yield using the photonic electron tagging method. The yields obtained from events triggered by EMCal with EG2 (red) and EG1 (blue) triggers appear higher compared to those from MB triggered events. The raw yields obtained from EG2 and EG1 triggered events are normalized by their corresponding trigger rejection factor and the number of events to facilitate comparison with MB triggered events.

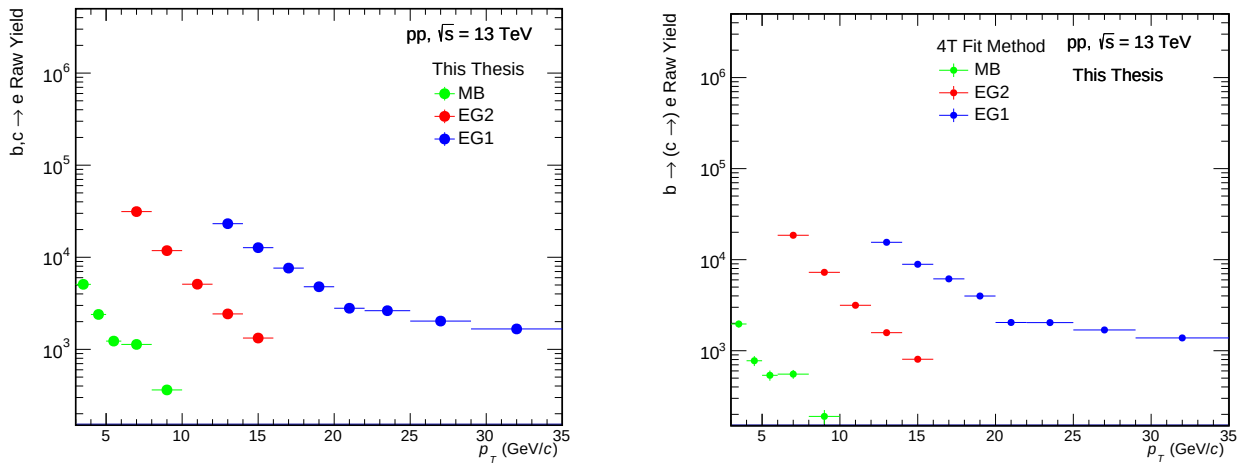

(a) (b)

Figure 4.19: (a): The yield of heavy-flavor decay electrons. (b): The yield of beauty-hadron decay electrons, categorized in their respective p_{T} bins for events triggered by MB, EG2, and EG1 triggers.

Figure 4.19 (b) shows the estimated raw yield of electrons from beauty-hadron decays, determined through a template fit method. Yields from EMCal-triggered events with EG2 (red) and EG1 (blue) triggers are higher than those from MB triggered events. Raw yields from EG2 and EG1 triggered events are normalized by their respective trigger rejection factors and event counts for comparison with MB triggered events.

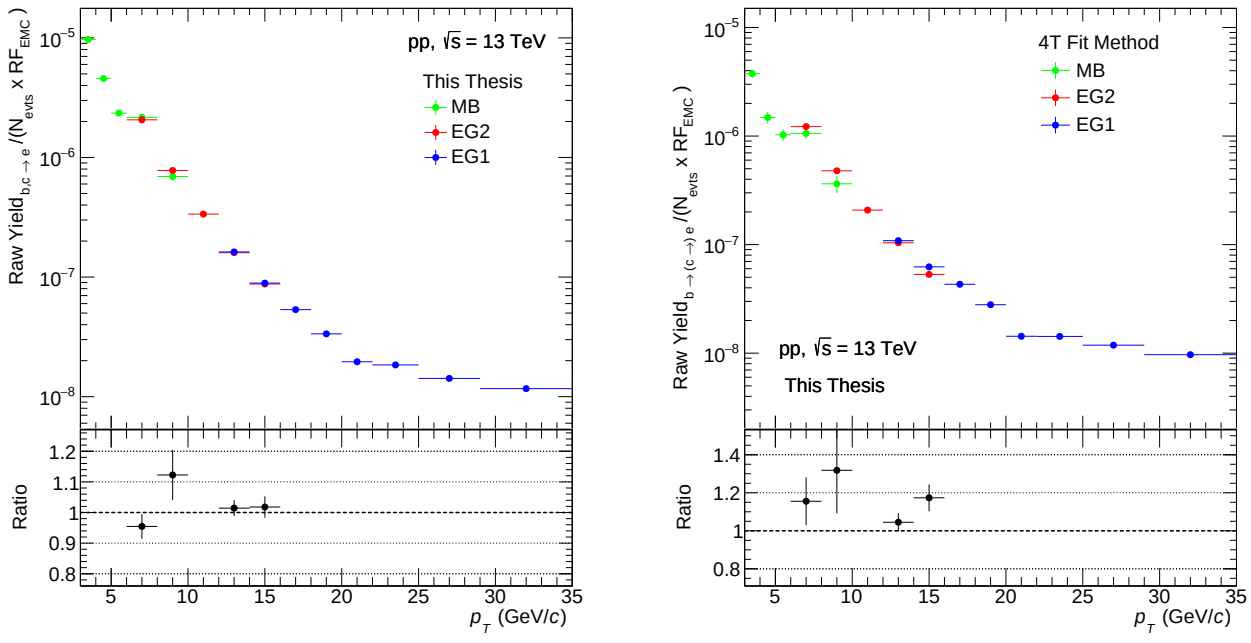

(a) (b)

Figure 4.20: The raw electron yields normalized by the number of events and EMCal trigger rejection factors estimated from heavy-flavor (a) and beauty-hadron (b) decays. The ratio of yields in overlapping p_{T} bins.

The top panels of Fig. 4.20 show the normalized yield of electrons from heavy-flavor (a)

and beauty-hadron (b) decays. The bottom panels illustrate the ratio of yields obtained in the overlapping p_{T} bins of MB and EG2 (i.e., $6 < p_{\mathrm{T}}$ GeV/c < 10) and in the overlapping p_{T} bins of EG2 and EG1 (i.e., $12 < p_{\mathrm{T}}$ GeV/c < 16) for consistency checking. Yields in the ranges $3 < p_{\mathrm{T}}$ GeV/c $<$ from MB, $6 < p_{\mathrm{T}}$ GeV/c < 12 from EG2, and $12 < p_{\mathrm{T}}$ GeV/c < 35 are selected for estimating heavy-flavour electron and beauty-decay electron cross-sections to reduce statistical errors.

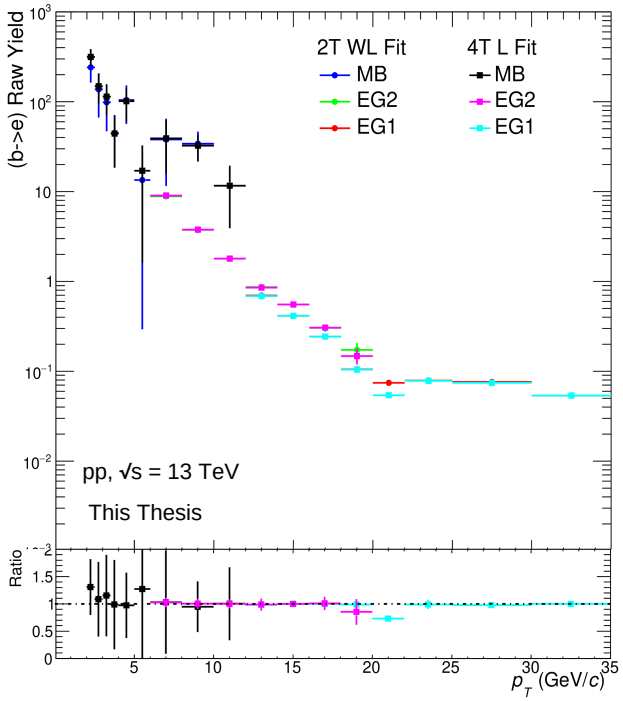

Figure 4.21: Comparison of normalized $b \rightarrow (c \rightarrow) e$ yield estimated using Two-Template weighted log-likelihood and Four-Template log-likelihood fit methods in proton-proton collisions at collisions at $\sqrt{s}$ = 13 TeV.

The top panel of Fig. 4.21 shows a comparison of the normalized beauty-hadron decay electron ($b \rightarrow (c \rightarrow) e$) yields, derived through the Two-Template (2T) and Four-Template (4T) fit methods. In the bottom panel, the ratio of yields obtained from the 4T fit to the 2T fit method is depicted across their respective p_{T} bins for MB, EG2, and EG1 triggered events. The yields obtained from both methods exhibit consistency and agreement within statistical uncertainties. Notably, for the bin $20 < p_{\mathrm{T}}$ (GeV/c) < 22 triggered by EG1, the yield from the 2T fit method is higher by approximately 20% compared to the 4T fit method. However, it is essential to note that an exhaustive toy model study, as detailed in the reference [188], demonstrates that both fitting techniques yield similar results, provided that the data and templates have reasonably large statistics to mitigate fluctuations. Consequently, the raw yields obtained from the Four-Template fits were utilized for computing the final $b \rightarrow (c \rightarrow) e$ cross-section, a discussion of which will follow in subsequent sections.

4.8 Acceptance and reconstruction efficiency

The p_{T} spectra of electrons originating from heavy-flavour decays, including those from beauty hadron decays, are corrected for detector effects such as acceptance and reconstruction efficiency. The reconstruction efficiency is defined as the ratio of electron candidates passing geometric acceptance, track quality, and particle identification cuts to the total number of electrons generated within the same MC sample and detector acceptance [19]. The total reconstruction efficiency of electrons can be calculated using the formula provided in Eqn. 4.15.

$$\mathcal{E}_{\mathrm{Reco}} = \frac{\text{HFe counts after passing (track slection } + \text{track cluster matching } + \text{eID) cuts}}{\text{Generated HFe counts in MC sample}}$$

$$= \frac{N^{\mathrm{e}}_{\text{Pass Track Cuts}}}{N^{\mathrm{e}}_{\text{Generated in MC sample}}} \times \frac{N^{\mathrm{e}}_{\text{Pass TrackMatch Cut}}}{N^{\mathrm{e}}_{\text{Pass Track Cuts}}} \times \frac{N^{\mathrm{e}}_{\text{Pass E}/p\text{ Cut}}}{N^{\mathrm{e}}_{\text{Pass TrackMatch Cuts}}} \times \frac{N^{\mathrm{e}}_{\text{Pass n}_{\sigma,\text{TPC}}\text{ Cut}}}{N^{\mathrm{e}}_{\text{Pass E}/p\text{ Cuts}}} \times \frac{N^{\mathrm{e}}_{\text{Pass M02 Cut}}}{N^{\mathrm{e}}_{\text{Pass n}_{\sigma,\text{TPC}}\text{ Cut}}} \tag{4.11}$$

$$\therefore \quad \mathcal{E}^{\mathrm{MC}}_{\mathrm{Reco}} = \mathcal{E}_{\text{Track Selection Cut}} \times \mathcal{E}_{\text{Track Match Cut}} \times \mathcal{E}_{\text{E/p Cut}} \times \mathcal{E}_{\mathrm{n}_{\sigma,\text{TPC}}\text{ Cut}} \times \mathcal{E}_{\text{M02 Cut}}$$

The EMCal acceptance efficiency correction is incorporated into the track-cluster matching term $\mathcal{E}_{\text{Track Match Cut}}$ of the reconstruction efficiency, eliminating the need for a separate correction. However, a discrepancy in the efficiency of the TPC electron identification cut and EMCal shower shape cut is observed between the data and MC simulations. As a result, the $\mathcal{E}_{\mathrm{n}_{\sigma,\text{TPC}}\text{ Cut}}$ and $\mathcal{E}_{\text{M02 Cut}}$ is calculated using the data.

4.8.1 Efficiency of $\mathrm{n}_{\sigma,\mathrm{TPC}}$ cut

The TPC $\mathrm{n}_{\sigma,\mathrm{TPC}}$ cut efficiency is determined by computing the ratio of the integral of the electron Gaussian[1] distribution within the range $-1 \leq \mathrm{n}_{\sigma,\mathrm{TPC}} \leq 3$ to the total electrons contained within the Gaussian fit representing the electron contribution, after applying the E/p and M02 cuts [19, 27].

$$\mathcal{E}_{\mathrm{n}_{\sigma,\mathrm{TPC}}} = \frac{\text{Number of electrons in } -1 \leq \mathrm{n}_{\sigma,\mathrm{TPC}} \leq 3}{\text{Total number of electrons in the blue Guassian}} \tag{4.12}$$

Figure 4.22 displays the $\mathrm{n}_{\sigma,\mathrm{TPC}}$ distribution obtained after applying the E/p and M02 cuts.

[1]Gaussian distribution: $f(x) = \frac{1}{\sigma\sqrt{2\pi}} e^{-\frac{1}{2}\left(\frac{x-\mu}{\sigma}\right)^2}$, where μ is the mean and σ is the standard deviation. Landau distribution: $p(x) = \frac{1}{\pi}\int_0^\infty e^{-t\log(t)-xt}\sin(\pi t)dt$.

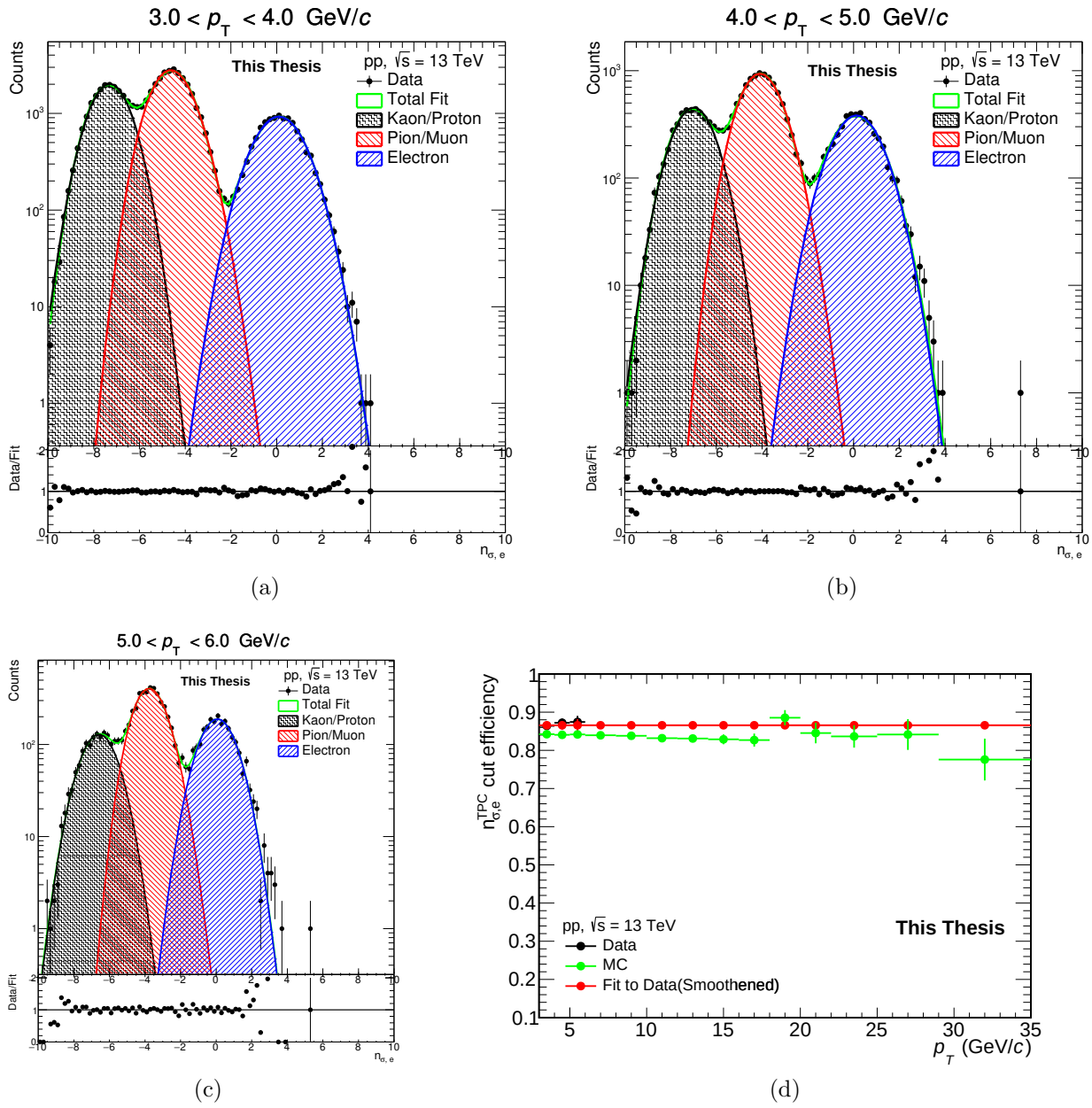

Figure 4.22: $n_{\sigma,\mathrm{TPC}}$ distributions are fitted with Gaussian (for kaon/proton) + Landau × Exponential (for pion) + Gaussian (for electron) in the range $3 < p_{\mathrm{T}}$ (GeV/c) < 4 (a), $4 < p_{\mathrm{T}}$ (GeV/c) < 5 (b), and $5 < p_{\mathrm{T}}$ (GeV/c) < 6 (c) respectively. (d): Comparison of TPC electron identification efficiency between data (black) and MC (green) in proton–proton collisions at $\sqrt{s}$ = 13 TeV.

The integral of the electron Gaussian (shown in blue) in the region $(-1 \leq n_{\sigma,\mathrm{TPC}} \leq 3)$ provides the numerator for the TPC eID efficiency, while the total integral of the electron Gaussian serves as the denominator. The $n_{\sigma,\mathrm{TPC}}$ cut efficiency from data is calculated in the lower p_{T} region. This choice is made because, as we move towards higher p_{T} (> 8 GeV/c), the TPC is unable to distinguish electrons from hadrons due to the band merging effect. To estimate the efficiency at higher p_{T} , data points in the lower p_{T} bins are fitted with a zero-order polynomial and extrapolated into the higher p_{T} region, as shown in Fig. 4.22 (d). The $n_{\sigma,\mathrm{TPC}}$ efficiency in data is observed to be $\sim 86\%$, which is slightly higher than the efficiency observed in MC

simulations, which is $\sim 84\%$.

4.8.2 Purity of identified electron sample and efficiency of shower shape cut

The sub-section discusses the assessment of the purity in the identified electron sample and evaluates the efficiency of the shower shape cut. The purity and efficiency of the shower shape cut both are determined using the E/p distributions shown in figure A.1. The purpose of analyzing the shape of showers created by particles inside the EMCal is to distinguish genuine electron tracks from hadron tracks that are misidentified as electron tracks, primarily based on the long axis of the particle shower (M02). The purity of the identified electron sample is calculated by computing the ratio of the integral of the pure electron E/p distribution divided by the integral of the electron candidate E/p distribution, both within the range of $-0.85 \leq E/p \leq 1.2$, for each p_{T} , using Eqn. 4.13.

$$\mathcal{P}_{\mathrm{electron}} = \frac{\text{Electron counts within } (-0.85 \leq \mathrm{E}/p \leq 1.2)}{(\text{Hadron} + \text{Electron}) \text{ counts within } (-0.85 \leq \mathrm{E}/p \leq 1.2)} \tag{4.13}$$

The ratio of electron counts from the E/p distribution after the application of M02, E/p, and $\mathrm{n}_{\sigma,\mathrm{TPC}}$ cuts, to the electron counts from the E/p distribution with only E/p and $\mathrm{n}_{\sigma,\mathrm{TPC}}$ cuts applied, provides the efficiency of the shower shape cut [19].

$$\mathcal{E}_{\mathrm{M02}} = \frac{\text{Electron counts after passing } (\mathrm{n}_{\sigma,\mathrm{TPC}} + \mathrm{E}/p + \mathrm{M02}) \text{ cuts}}{\text{Electron counts after passing } (\mathrm{n}_{\sigma,\mathrm{TPC}} + \mathrm{E}/p) \text{ cuts}} \tag{4.14}$$

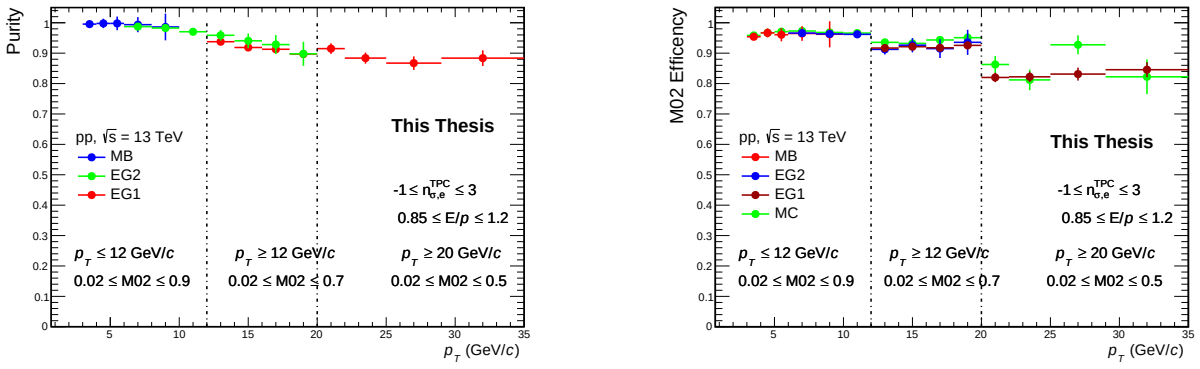

(a) (b)

Figure 4.23: (a): Purity of the identified electron sample in data. (b): Comparison between the efficiency of the shower shape cut in data and Monte Carlo simulations.

The resulting identified electron sample purity after implementing the shower shape slection criteria M02 and efficiency of the cut used, exceeds 90% for $p_{\mathrm{T}} < 20$ GeV/c and remains above 80% for p_{T} up to 35 GeV/c.

4.8.3 Estimation of data-driven reconstruction efficiency

$$\mathcal{E}_{\text{Reco}}^{\text{Data-Driven}} = \mathcal{E}_{\text{Track Selection Cut}}^{\text{MC}} \times \mathcal{E}_{\text{Track Match Cut}}^{\text{MC}} \times \mathcal{E}_{\text{E/p Cut}}^{\text{MC}} \times \mathcal{E}_{\text{n}_{\sigma,\text{TPC}}\text{ Cut}}^{\text{Data}} \times \mathcal{E}_{\text{M02 Cut}}^{\text{Data}} \tag{4.15}$$

The total data-driven reconstruction efficiency is calculated using Eqn. 4.15. Figures 4.24(a) and 4.25(a) respectively show the reconstruction efficiency of HFe and beauty-hadron decay electrons estimated using pure MC simulations. Meanwhile, Figures 4.24(b) and 4.25(b) show the data-driven reconstruction efficiency of HFe and beauty-hadron decay electrons, respectively.

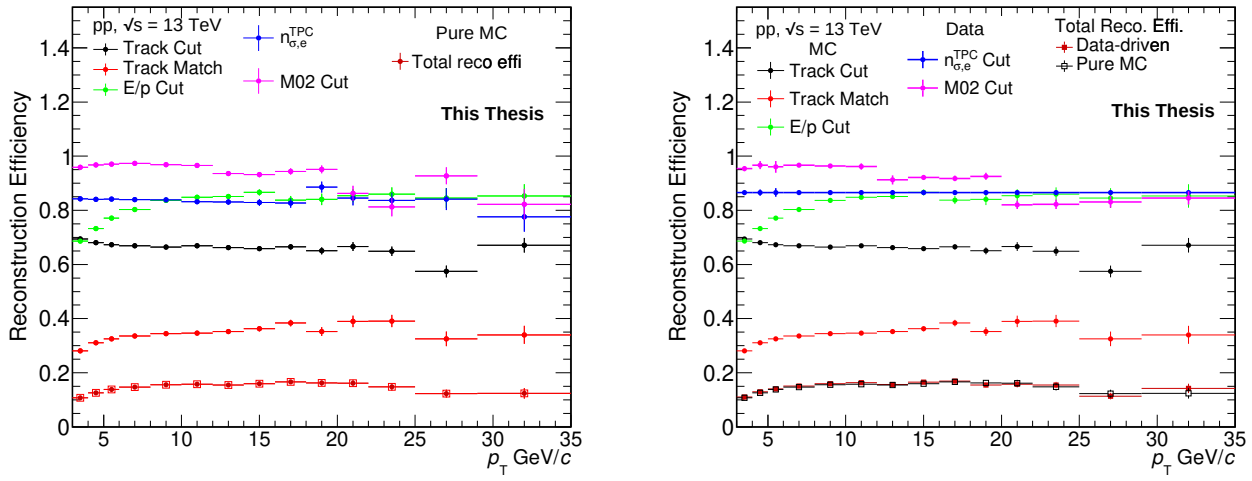

(a) (b)

Figure 4.24: The total HFe reconstruction efficiency estimated from (a) pure MC and (b) data-driven approach

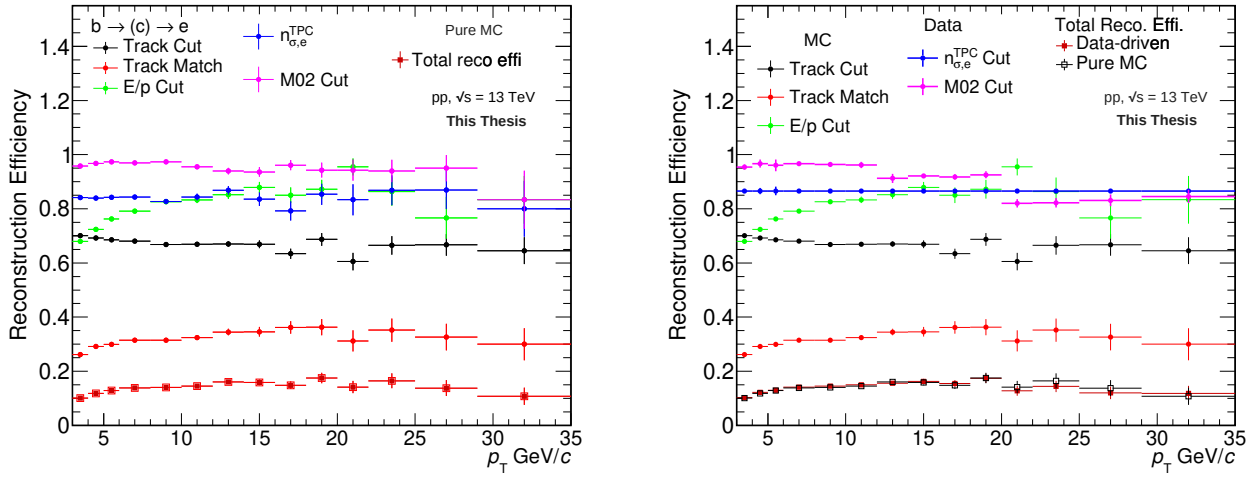

(a) (b)

Figure 4.25: The total $b \to (c \to) e$ reconstruction efficiency estimated using (a) pure MC and (b) data-driven approach.

4.9 Combining spectra from different periods

To ensure consistency across different periods, a merging process was employed to derive the final spectra. The merging of spectra was accomplished using the formula:

$$\frac{\sum_{i=1}^{N} x_i/\sigma_i^2}{\sum_{i=1}^{N} 1/\sigma_i^2} \tag{4.16}$$

The statistical error was computed using the formula:

$$\sigma = \sqrt{\frac{1}{\sum_{i=1}^{N} 1/\sigma_i^2}} \tag{4.17}$$

Here, x_i represents the measured data, and σ_i signifies the statistical error associated with individual periods.

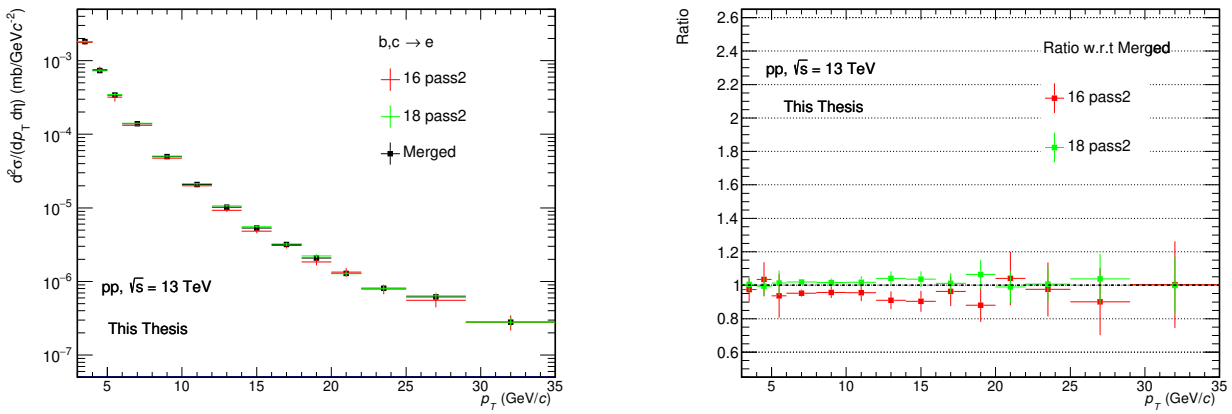

(a) (b)

Figure 4.26: (a): A comparison of heavy-flavor electron spectra between periods 16 and 18, alongside the merged spectra. (b): Ratio illustrating the variation in HFe spectra across different periods relative to the merged spectra.

Figure 4.26 illustrates the comparison of HFe spectra estimated from LHC periods 16 and 18, superimposed with the combined spectra containing data from both periods. Figure (b) presents the ratio between the spectra of periods 16 and 18 with respect to the combined spectra. Notably, the relative error associated with the data from period 16 appears larger, primarily attributable to lower statistical significance when compared to the data from period 18. The relative error becomes notably greater for $p_{\mathrm{T}} < 6$ GeV/c, as the spectra within this range are computed from MB sample. Triggered samples exhibit higher electron statistics compared to the minimum bias sample, leading to a reduction in the relative error. However, the error bars begin to escalate at higher p_{T} values due to inadequate electron statistics. The

identical procedure for merging the HFe spectra was applied to combine the beauty-decay electron spectra. In figure 4.27 (a), the combined $b \rightarrow (c \rightarrow) e$ spectra superimposed with data from 16 and 18 periods. Figure 4.27 (b) illustrates the ratio of $b \rightarrow (c \rightarrow) e$ spectra from the 16 and 18 periods relative to the combined spectra.

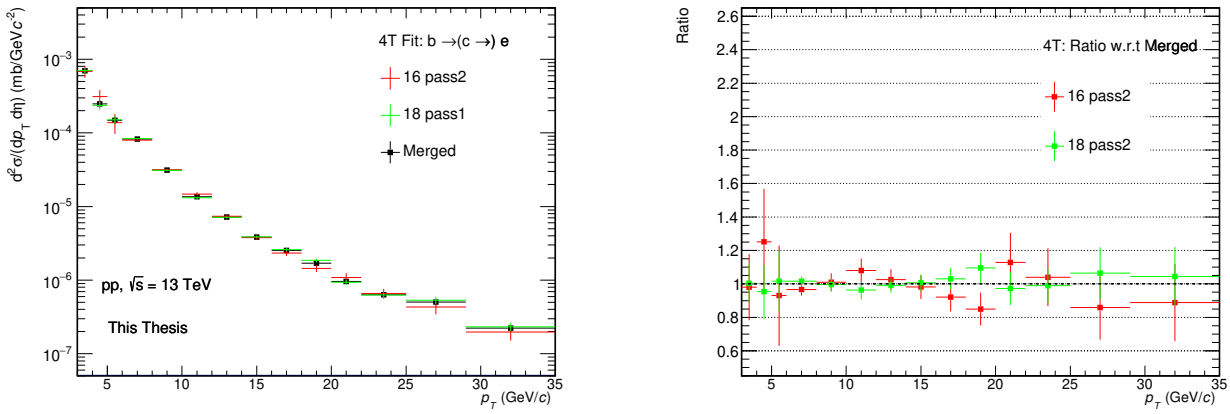

(a) (b)

Figure 4.27: (a): A comparison of beauty-decay electron spectra between periods 16 and 18, alongside the merged spectra. (b): Ratio illustrating the variation in $b \rightarrow (c \rightarrow) e$ electron spectra across different periods relative to the merged spectra.

4.10 Systematic uncertainity studies

Once the cross-section has been determined, the next step is to estimate the systematic uncertainties that may result from various selection criteria and corrections. Systematic error is the deviation from the true value caused by non-statistical effects, even when there is enough statistical data available. This error originates from inherent imperfections in the measurement process, such as detector flaws or inaccuracies in calibrations, which persist regardless of the number of measurements taken. In the case of cross-section measurements, systematic error arises from factors such as detector imperfections and calibrations, and every correction made to a spectrum introduces its own associated systematic error that must be taken into account.

Previous analyses of heavy-flavour and beauty-hadron decay electron data have investigated various sources of systematic error, including track reconstruction, hadron contamination, non-heavy flavour electron subtraction, HF spectra correction, fit stability, and EMCal trigger rejection factor. These sources, along with others, are discussed in Ref. [19, 27]. Of all the sources examined, electron identification cuts were found to produce the largest systematic error. It is important to note that the systematic error presented in the HFe and $b \rightarrow (c \rightarrow) e$ cross-sections only reflects the contribution from electron identification cuts. The contribution from the other sources will be addressed once the ongoing study is completed, and the final

adjustments to the systematic errors will be made to the final results.

4.10.1 Electron identification cut variation

Table 4.7: Summary of variations studied for electron identification cuts

Electron identification	Standard cut	Variations
$n_{\sigma,TPC}$	$(-1, 3)$	$(-0.75, 3)$, $(-1.5, 3)$ $(-1, 3.5)$
E/p	(0.85, 1.2)	(0.75, 1.2), (0.8, 1.2), (0.9, 1.2) (0.85, 1.15), (0.85, 1.25)
M02	$0.02 \leq$ M02 $\leq$ 0.9, 0.7, 0.5 $p_T < 12$, $p_T < 20$, $p_T > 20$ (GeV/c)	$0.02 \leq$ M02 $\leq$ 0.8, 0.6, 0.4 $0.02 \leq$ M02 $\leq$ 1.0, 0.8, 0.6

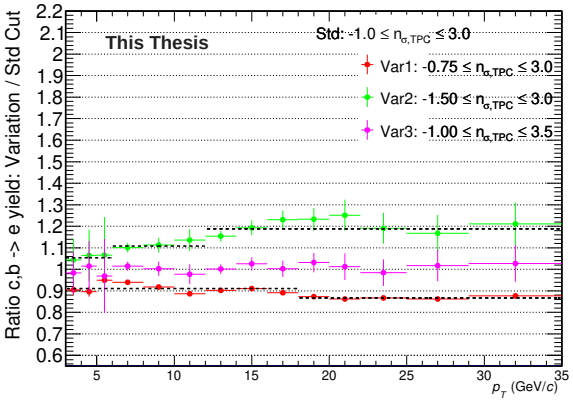

(a) $n_{\sigma,TPC}$ cut

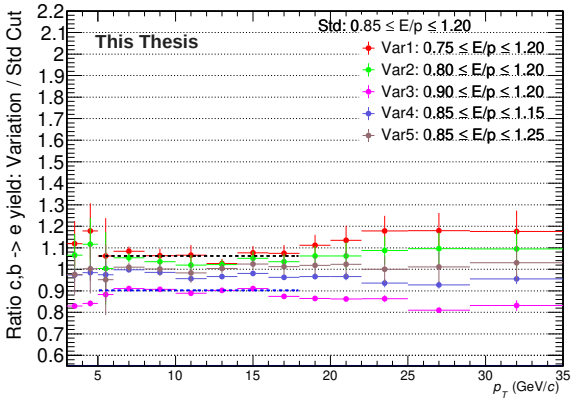

(b) E/p cut

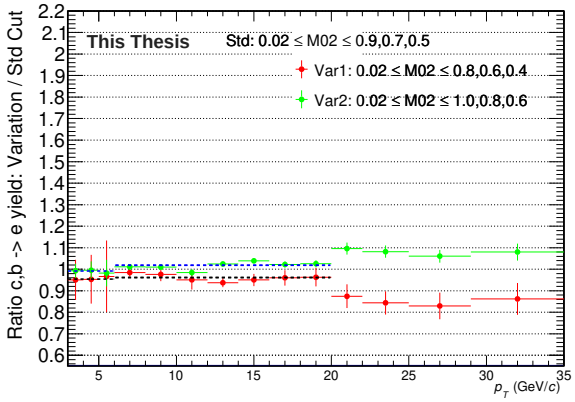

(c) Shower shape cut

Figure 4.28: Ratio of HFe yield obtained for varied cuts compared to the yield obtained for standard electron identification cuts.

Table 4.7 presents a summary of the standard cut values along with their variations utilized for assessing systematics from eID cuts ($n_{\sigma,TPC}$, E/p, and M02). The ratio of HFe yield obtained for varied cuts compared to the yield obtained for standard electron identification cuts is depicted in Fig. 4.28. Deviations are fitted with a straight line to estimate the systematic effects from each identification in different p_T regions. Subsequently, the estimated deviations from

the standard yield are combined in quadrature. A systematic error of approximately 10.5% to 13% for the $3 \leq p_{\mathrm{T}}$ (GeV/c) ≤ 35 bins is assigned. It's important to note that a rough value of systematic error has been assigned to the final result at this stage for caution. The final adjustments to the systematic errors from all the potential sources, considering both data and Monte Carlo simulations, will be made to obtain accurate values of systematic error.

4.11 The p_{T} -differential production cross-section

To calculate the invariant cross section, the efficiency corrected spectra must be normalized by several factors: the number of analyzed events (N_{evts}), the space element factors $\mathrm{d}\eta = 1.2$ (per unit rapidity) and $\mathrm{d}\varphi = 2\pi$ (per unit azimutal coverage), as well as p_{T} $\mathrm{d}p_{\mathrm{T}}$ (bin centre and bin width), a correction factor of 2 for electron-positron balance ($\frac{e^{+}+e^{-}}{2}$) and a multiplication by 57.95 (the Minimum Bias cross-section for proton-proton collisions at $\sqrt{s}$ = 13 TeV, $\sigma_{\mathrm{MB}} = 57.95 \pm 0.9$ mb [189]). Equation 4.18 outlines the specific steps to derive the invariant cross-section from the raw yield $N_{\mathrm{raw}}(p_{\mathrm{T}})$, wherein $\mathscr{L}_{int}$ represents the integrated luminosity, derived from the cross-section σ_{MB} and the number of events, i.e., $\mathscr{L}_{\mathrm{int}} = N_{\mathrm{evts}}/\sigma_{\mathrm{MB}}$ [96].

$$\frac{\mathrm{d}^2\sigma}{\mathrm{d}p_{\mathrm{T}}\mathrm{d}\eta} = \frac{N_{\mathrm{raw}}(p_{\mathrm{T}})}{2 \cdot 2\pi \cdot p_{\mathrm{T}}\Delta p_{\mathrm{T}}\Delta\eta \cdot \mathcal{E}_{\mathrm{Reco}}^{\mathrm{Data-Driven}}(p_{\mathrm{T}}) \cdot \mathscr{L}_{\mathrm{int}}} \tag{4.18}$$

The p_{T} -differential cross-section of heavy-flavour decay electrons [Fig. 4.29 (a)] and beauty-hadron decay electrons [Fig. 4.29 (b)] are subsequently compared with pQCD predictions using FONLL [87, 88, 172]. Vertical error bars denote statistical uncertainties, while systematic uncertainties are indicated by rectangular boxes on the measured data. The uncertainty bands in the FONLL calculations arise from various considerations, , including variations in the mass of charm and beauty quarks, choices in factorization and renormalization scales, and fluctuations within the set of parton distribution functions (PDF) employed in the pQCD calculations. To predict the transverse momentum (p_{T}) distribution of leptons originating from $c, b \rightarrow e$ and $b \rightarrow (c \rightarrow) e$, FONLL calculations employ a numerical convolution involving a perturbative cross section, a non-perturbative fragmentation function, and a decay function for the hadron's weak decay into a lepton [88]. The parameters of the fragmentation function are deduced from e^{+} e^{-} collision data involving B^{+}, B^{-}, and B^{0} mesons. The weak decay function and branching ratios are also determined from experimental data. Notably, FONLL calculations overlook potential distinctions in the fragmentation and decay kinematics of the substantial contribution from beauty baryons [190] since the fragmentation functions are derived solely from B meson data [27].

The FONLL calculations adequately describe both the measurements within statistical and

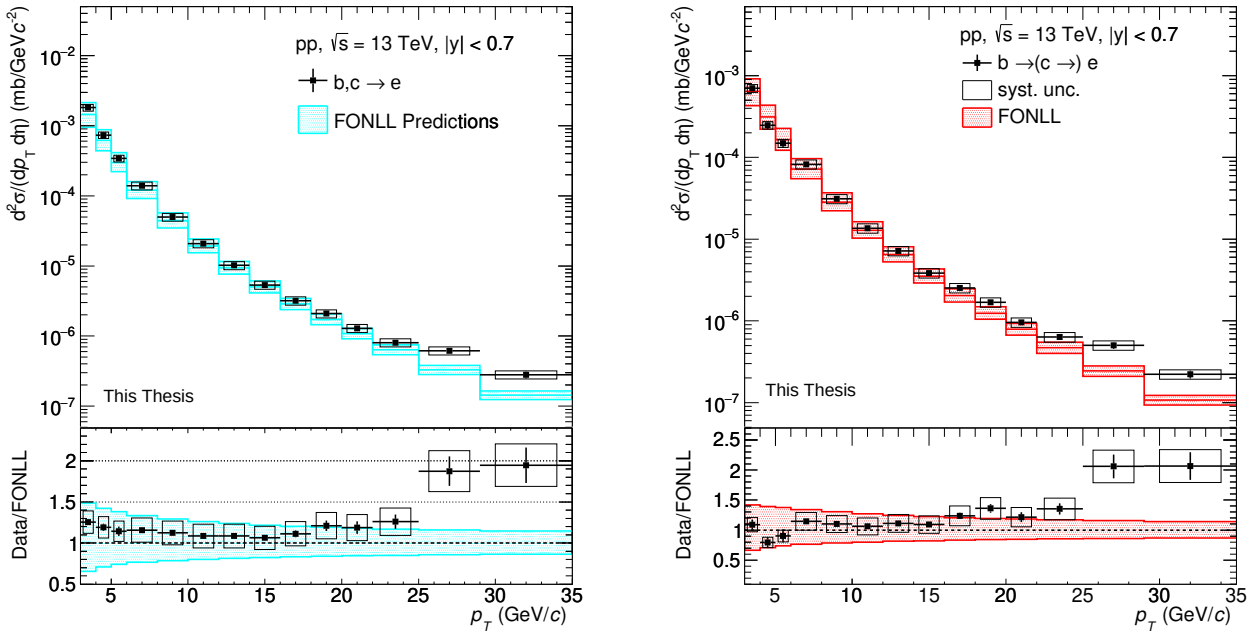

(a) (b)

Figure 4.29: The invariant cross-section of heavy-flavour decay electrons (a) and beauty-hadron decay electrons (b) in proton-proton collisions at a center-of-mass energy of $\sqrt{s}$ = 13 TeV, compared with FONLL predictions.

systematic uncertainties. The data points are observed to closely align with the central or upper edges of the pQCD predictions up to $p_{\mathrm{T}} < 25$ GeV/c. A similar trend is observed in proton-proton collisions at centre-of-mass energies of $\sqrt{s}$ = 2.76, 5.02 and 7 TeV [27, 92, 95, 180, 191–193]. However, the $b \to (c \to) e$ data underestimates the FONLL central values in the $4 < p_{\mathrm{T}}$ (GeV/c) < 6 region. In both p_{T} spectra, for $c, b \to e$ and $b \to (c \to) e$, the last two bins ($25 - 30$ GeV/c and $30 - 35$ GeV/c) exhibit significantly higher measurements than FONLL predictions, nearly double the anticipated values. It's worth noting that contributions from $W^{\pm}/Z^0$ decays to electrons were not corrected for and account for approximately 12% at $p_{\mathrm{T}} = 25 - 30$ GeV/c and 40 % at $p_{\mathrm{T}} = 30 - 35$ GeV/c. Moreover, at such high p_{T} , the likelihood of including hadrons mistaken for electrons increases due to the merging of the $\mathrm{n}_{\sigma,\mathrm{TPC}}$ band of electrons with other hadrons. As a result, it becomes considerably challenging to isolate these contributions accurately. Therefore, the substantial deviation of the last two bins from FONLL predictions might be due to the inclusion of miss-identified electrons, contributing significantly to the spectra's elevation compared to FONLL predictions.

Figure 4.30 shows the fraction of electrons originating from beauty-hadron decays relative to the total heavy-flavor decay electrons, plotted as a function of transverse momentum in proton-proton collisions at a center-of-mass energy of $\sqrt{s}$ = 13 TeV, and compared with FONLL predictions. The measured data is found to be in agreement with the theoretical predictions for $p_{\mathrm{T}} < 30$ GeV/c within statistical and systematic uncertainties. However, the final bin

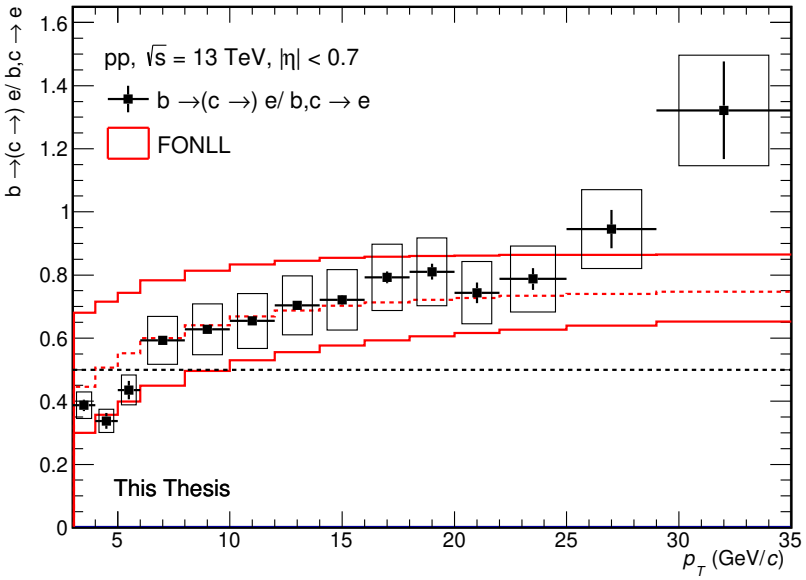

Figure 4.30: The ratio of p_{T} -differential cross-section of beauty-hadron decay electrons to heavy-flavour decay electrons in proton-proton collisions at a center-of-mass energy of $\sqrt{s}$ = 13 TeV, compared with FONLL.

exhibits a notable elevation from the FONLL predictions. The data suggests an increasing dominance of beauty contributions among total heavy-flavour decay electrons with rising p_{T} , indirectly indicating that beauty production begins to dominate with increasing p_{T} in proton-proton collisions at $\sqrt{s}$ = 13 TeV. Despite the appearance of FONLL central values plateauing at high p_{T} , hinting at enhanced beauty production within the heavy-flavour overall output, rigorous testing of pQCD models is required in the much higher p_{T} range of $25 < p_{\mathrm{T}}$ (GeV/c) < 50. The extension of the $b \to (c \to) e$ measurement to $p_{\mathrm{T}} = 35$ GeV/c with TPC+EMCal in Run2 data presented a significant challenge. However, the acquisition of triggerless Run3 data holds promise for a more precise measurement of heavy-flavor particles at such high p_{T} . Additionally, the determination of the baryon-to-meson ratio for beauty, unexplored in ALICE, represents a future outlook for this thesis, alongside multiplicity-dependent studies.

Chapter 5

Summary

In this thesis, a comprehensive exploration of particle collision dynamics in both proton-proton and nucleus-nucleus collisions is presented, aiming to investigate the low and high-temperature regimes of the QCD phase diagram. The chapter provides a summary of the results obtained, with a focus on potential future directions. The investigation covers both low and high-temperature regimes of the QCD phase diagram through experimental data analysis and phenomenological studies. The initial segment concentrates on the low-temperature domain of the QCD phase diagram, employing analyses of net charge and identified particle fluctuations along with the estimation of diffusion coefficients in rapidity space is carried out using the HIJING and UrQMD models at various collision energies available at RHIC.

The study explores event-by-event fluctuations of net-charge, net-pion, net-kaon, and net-proton using the variable $\nu_{(\pm,\mathrm{dyn})}$ across various models (HRG, HIJING, UrQMD) at different collision energies available at BNL RHIC. The analysis focuses on a 0.2 million central Au$-$Au events dataset at RHIC energies, considering a transverse momentum (p_{T}) range of $0.2 \leq p_T$ (GeV/c) ≤ 5.0 and a broad rapidity window ($0 \leq \Delta\eta \leq 5$). Results reveal a pronounced dependence of $\langle N_{\mathrm{ch}}\rangle\nu_{(\pm,\mathrm{dyn})}$ values on lower $\Delta\eta$, persisting to higher values with a lower slope in both models, except for the net protons in UrQMD. The UrQMD model shows distinct behaviour for net protons. Dynamical fluctuations of net-kaons and net-protons surpass those of net-pions and net-charged particles, with net-protons exhibiting slightly larger fluctuations than net-kaons. Notably, $\langle N_{\mathrm{ch}}\rangle\nu_{(\pm,\mathrm{dyn})}$ values from different models remain independent of collision energies but exhibit clear particle species dependence. This investigation enhances our understanding of dynamical fluctuations in various particle species within the RHIC collision environment [22, 108].

The fluctuations measured in the rapidity space may get diluted by the diffusion of charged hadrons during the system's evolution from hadronization to kinetic freeze-out. Investigating these fluctuations and their dependence on $\Delta\eta$ is crucial for understanding the medium's time

evolution and the hadronization process. Experimental observations show a lack of charge fluctuation suppression, typical in QGP, contrasting with observed suppressions aligned with diffusion estimates. These differences are significant: QGP suppression represents historical effects, while critical fluctuations pertain to equilibrium at freeze-out, necessitating diffusion to establish them. The study estimates diffusion rates for identified particle species at RHIC energies, fitting simulated data points with the error function to characterize diffusion in rapidity space. Results indicate a decrease in diffusion parameter with increasing particle mass, with net-proton and net-kaon diffusion coefficients consistently higher than net-pions across all energies. The diffusion process is influenced by particle mass, strangeness conservation, and baryon number conservation, with diffusion coefficients remaining constant across a wide collision energy range. These findings, presented in references [22, 23], serve as a baseline for RHIC measurements, highlighting the need for awaited experimental data to enhance our understanding of particle production mechanisms.

The latter part of the thesis shifts its focus to investigating the high-temperature regime of the QCD phase diagram, specifically exploring heavy quarks like charm and beauty. Besides the heavy-ion program, LHC experiments employ proton beams for proton-proton (pp) collisions, serving as reference data for systems without QGP. Despite the initial expectation that a QGP medium would not form in small systems like proton-proton collisions due to the smaller size of protons compared to heavy ions, LHC results have revealed soft signatures of QGP at high multiplicity in these small system collisions. Consequently, studying particle production in high-energy pp collisions focusing on multiplicity dependence has become crucial for understanding the particle production mechanism in such systems. The thesis uses data from the ALICE experiment at LHC, CERN to measure the production cross-section of electrons from beauty-hadron decays in pp collisions at a centre-of-mass energy of $\sqrt{s}$ = 13 TeV. The primary motivations and objectives for conducting the measurement are to investigate electrons from beauty-hadron decays in a higher transverse momentum range, extending up to 35 GeV/c, an unexplored domain within the ALICE experiment. Additionally, the measurement aims to test perturbative QCD calculations and serves as a baseline for studying nuclear modifications in proton-nucleus (p−A) and nucleus-nucleus (A−A) collisions. Such studies provide insights into the effects of cold nuclear matter in p−A collisions and shed light on how the QGP impacts heavy quark's behaviour as they traverse the medium in A−A collisions. The comparison between beauty and charm measurements, mainly the beauty-decay electron and heavy-flavor decay electron R_{AA}, offers a prospect to test mass-dependent energy loss effects, indicating a future outlook for this thesis.

The analysis utilizes a combination of ALICE central-barrel detectors, namely ITS, TPC,

and EMCal, which play critical roles in vertex determination, tracking, and particle identification for electron identification and selection. Events are triggered based on MB selection for the lower p_{T} range and two specific EMCal triggers, EG2 and EG1, for the higher p_{T} range. Particle identification within the TPC is achieved by measuring specific energy loss ($\mathrm{d}E/\mathrm{d}x$), with electrons selected within $-1 \leq \mathrm{n}_{\sigma,\mathrm{TPC}} \leq 3$. A p_{T} -dependent cut is applied to the long axis of the shower shape ellipse (M02) to enhance the purity of the electron sample. The selected electron sample is further refined by scaling and subtracting hadron contributions, utilizing the E/p distribution in each p_{T} bin of the analysis to minimize hadron contamination. Background from non-heavy-flavor electrons, specifically photonic electrons, is addressed through invariant mass distributions and tagging efficiency calculations (photonic electron tagging method). Impact parameter distributions (d_0) of inclusive electrons, hadrons, and non-heavy-flavour electrons are estimated from the data. In contrast, the d_0 of charm- and beauty-decay electrons are obtained from MC simulations and corrected to reflect realistic behaviour as observed in the data. Additionally, the contribution from electrons originating from W/Z boson decays is acknowledged, with corrections pending. Electrons from $b \rightarrow (c \rightarrow) e$ are measured using the d_0 fit method, involving templates from various sources fitted to the d_0 distribution of inclusive electrons. Finally, the estimated yield is corrected for geometrical acceptance and detector effects to obtain the p_{T} -differential cross-section.

The analysis of the measured cross-section reveals overall agreement with FONLL within the data uncertainties. However, specific p_{T} ranges exhibit variations; between 4 and 6 GeV/c, the data underestimates the FONLL central value, while in the 16 to 20 GeV/c range, the results align with the upper edge of FONLL predictions. Notably, for p_{T} values exceeding 20 GeV/c, the data points significantly surpass FONLL predictions. This divergence is attributed to the influence of W/Z boson decay electrons, a factor not corrected for in the measured data for this p_{T} range. A key focus is investigating the relative contribution of electrons from beauty quarks to the total heavy-flavour electron yield. The production cross-section of electrons from heavy-flavour hadron decay serves to estimate the fraction of beauty hadron decay electrons. Comparisons with FONLL predictions demonstrate consistency within the model's uncertainties. It's emphasized that the beauty quark contribution dominates the total heavy-flavour electron yield for p_{T} values greater than 6 GeV/c. These results provide valuable insights into electron production and contributions from beauty hadron decays, offering a meaningful comparison with pQCD predictions and enhancing our comprehension of heavy-flavour physics in high-energy collisions. Further investigations, particularly the correction for W/Z boson decay electrons, are crucial for refining these measurements and achieving a comprehensive understanding of heavy-flavour electron production.

Chapter 6

Future Outlook

The upcoming phase of the analysis involves obtaining the p_{T} -differential cross-section of beauty-hadron decay electrons ($b \rightarrow (c \rightarrow) e$) while correcting for the contribution of W/Z boson decay electrons. The future perspective of the thesis is to extend the measurement of $b \rightarrow (c \rightarrow) e$ in pp collisions at 13 TeV, focusing on multiplicity dependence studies to estimate self-normalized yields and associated systematic uncertainties. This will be achieved using the Run 2 ALICE data with TPC+EMCal detectors, with a future aim to propose a paper combining results from TPC+TOF and TPC+EMCal. The ongoing upgrade of the ALICE detector for Run 3 (started in 2022) and subsequent Run 4 presents exciting opportunities in proton-proton and nucleus-nucleus collisions. Recent data collection in 2022 and 2023, post-long shutdown (LS2), has laid the groundwork for analysis in the newly built O2 framework by the ALICE Collaboration, which is still in development. The detector upgrades and increased beam luminosity in future runs will enhance beauty measurements. Notably, the ITS upgrade promises improved primary vertex and impact-parameter resolution, offering a chance for precision measurements. With ALICE Run 3 data, the expectation is to measure fully reconstructed B meson decays (via the $B^{+} \rightarrow D^{0} + \pi^{+}$ channel) down to $p_{\mathrm{T}} = 2$ GeV/c and the Λ_b baryon down to around $p_{\mathrm{T}} = 7$ GeV/c [194]. This would mark a first for ALICE in B meson measurements, and the Λ_b baryon measurement has not been performed in heavy-ion experiments or by ALICE during Run 1 and 2. Comparing B mesons and Λ_b will allow testing of beauty-quark hadronization processes, considering the expected increase in the relative fraction of baryons like Λ_b over mesons due to coalescence. Additionally, full reconstruction of beauty hadrons will enable a direct comparison with measurements of reconstructed charm hadrons, providing insights into the charm and beauty R_{AA} and, consequently, the mass dependence of energy loss. The future of beauty studies in heavy-ion physics holds considerable promise, with new avenues for exploration and understanding.

Appendix A

Appendix

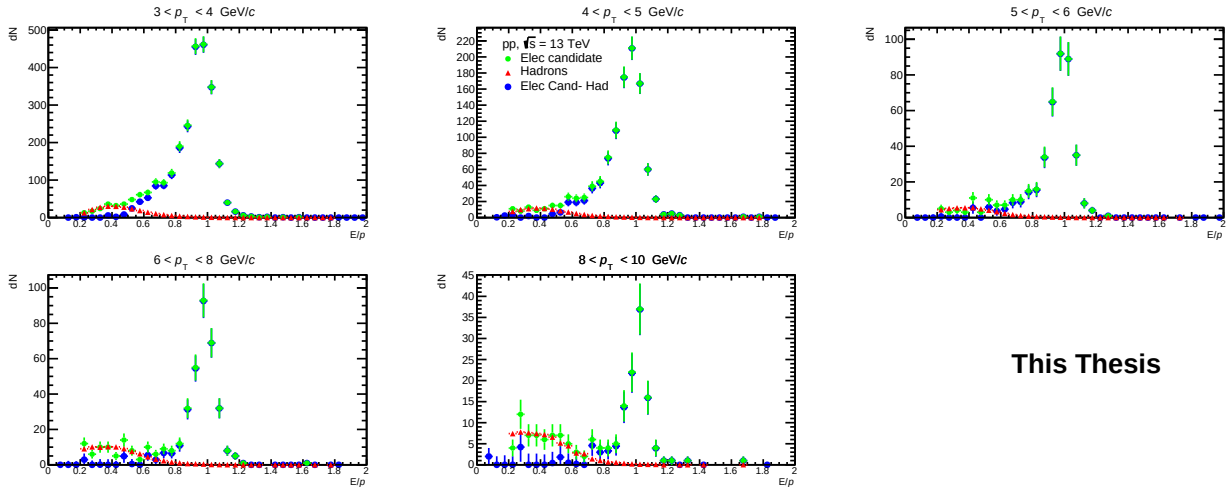

(a) MB trigger

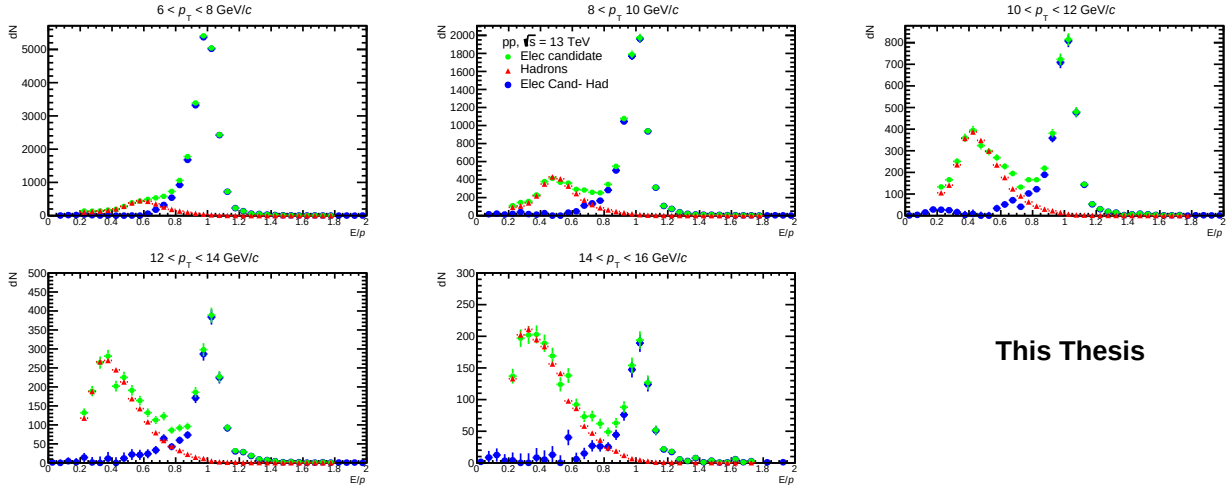

(b) EG2 trigger

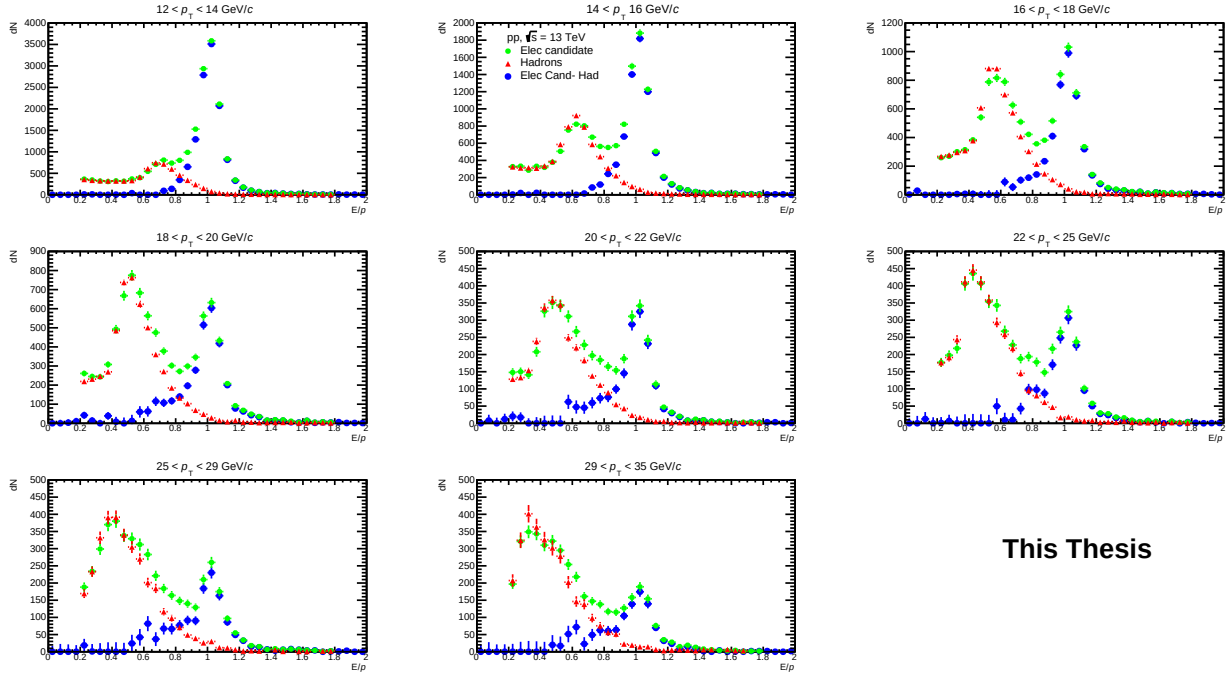

(c) EG1 trigger

Figure A.1: The E/p distribution of electron candidates (green) obtained after applying eID cuts, estimated hadron contamination (red) and pure electrons candidates (blue) in respective p_{T} bins of MB, EG2 and EG1 triggered events.

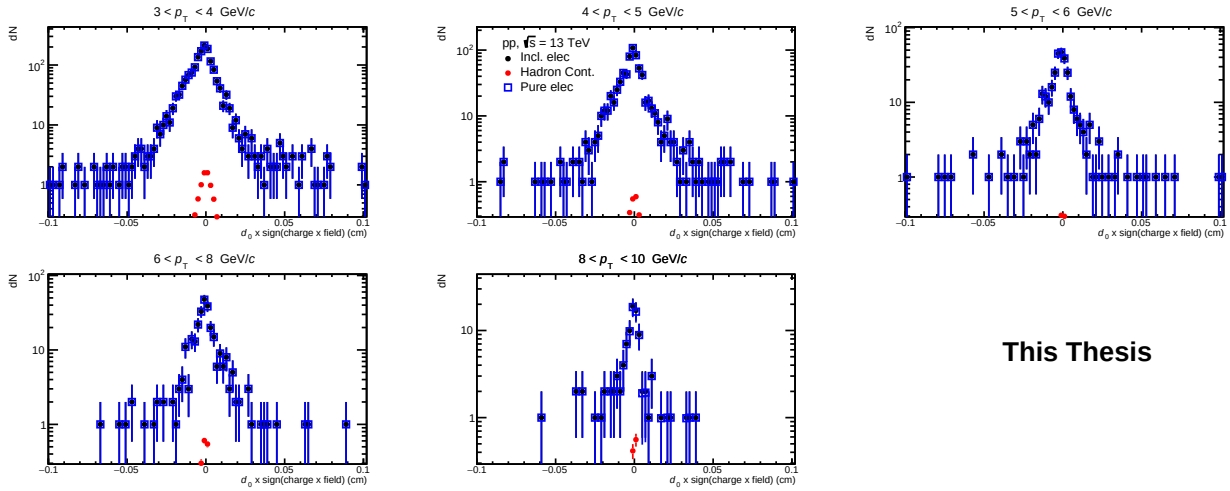

(a) MB trigger

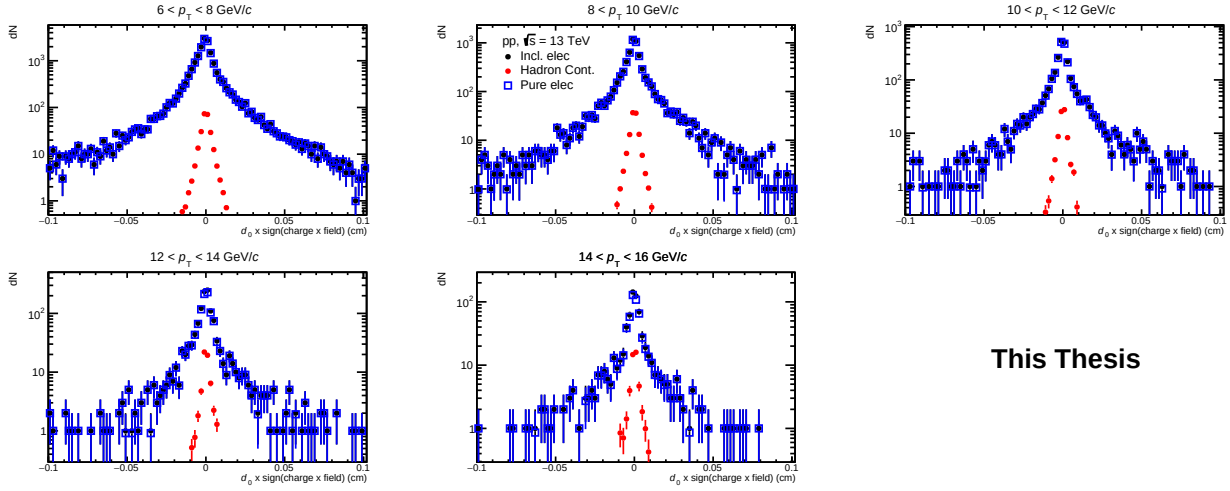

(b) EG2 trigger

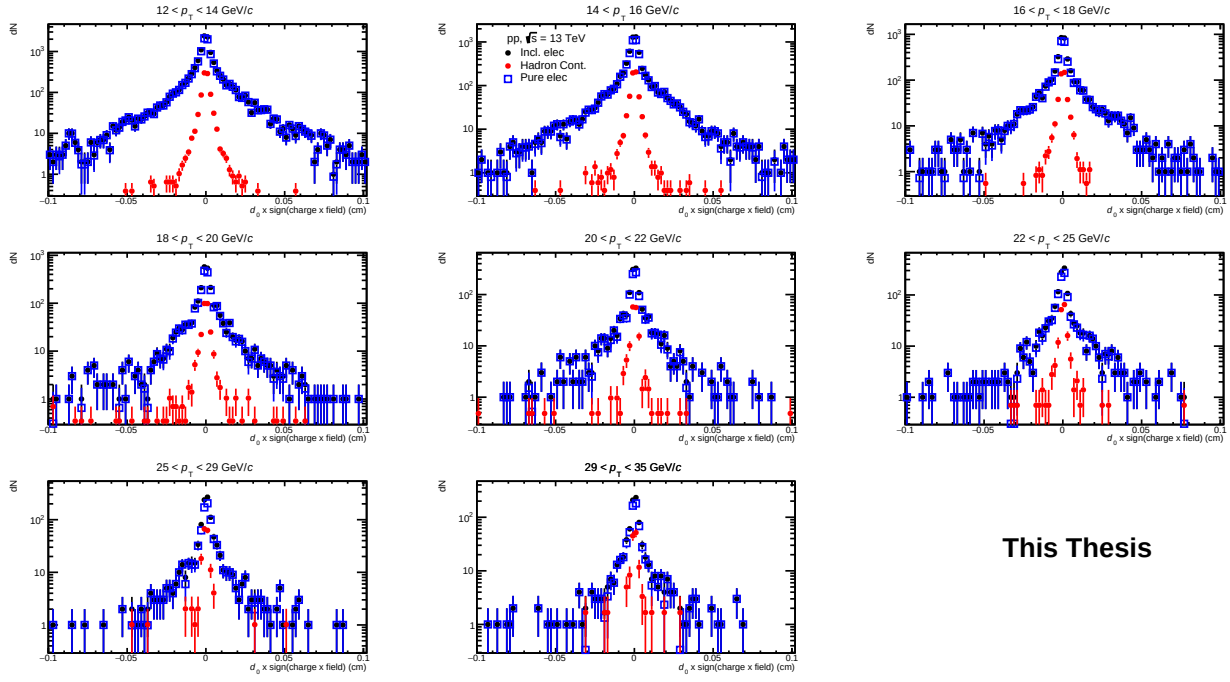

(c) EG1 trigger

Figure A.2: The d_0 distribution of inclusive electrons (black), hadron contamination (red) and pure electrons (blue) in respective p_T bins of MB, EG2 and EG1 triggered trigger events.

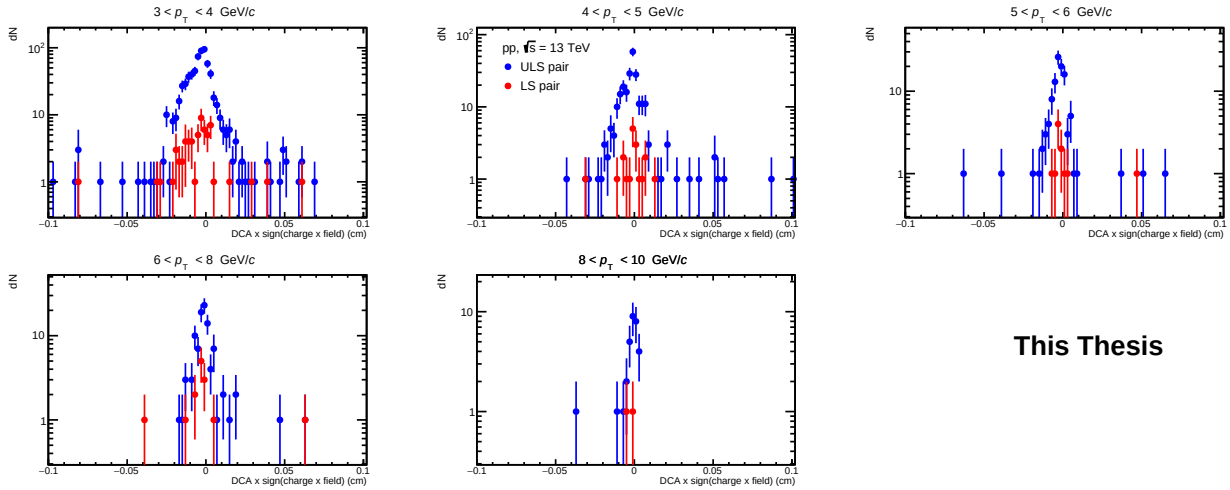

(a) MB trigger

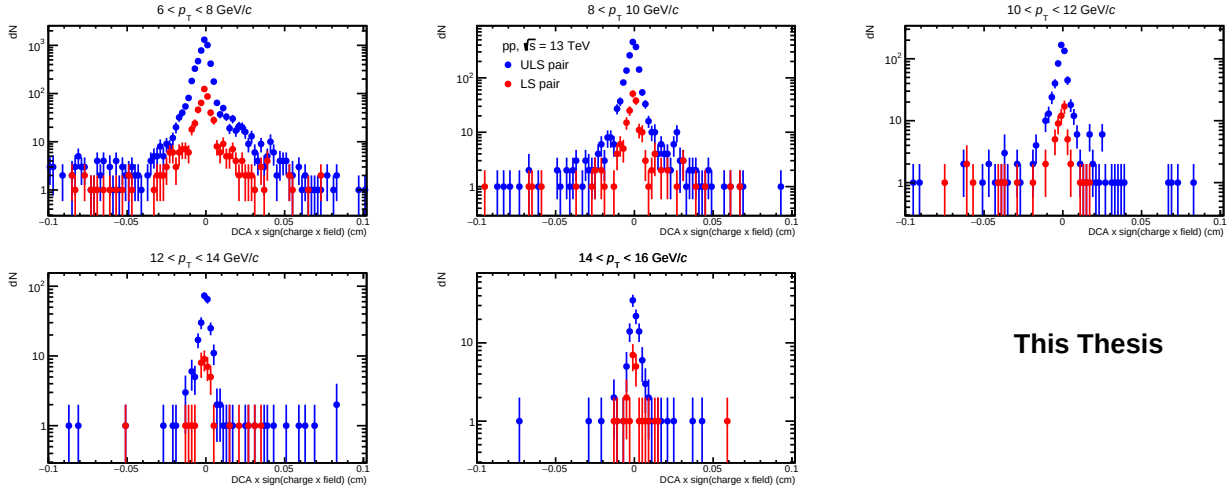

(b) EG2 trigger

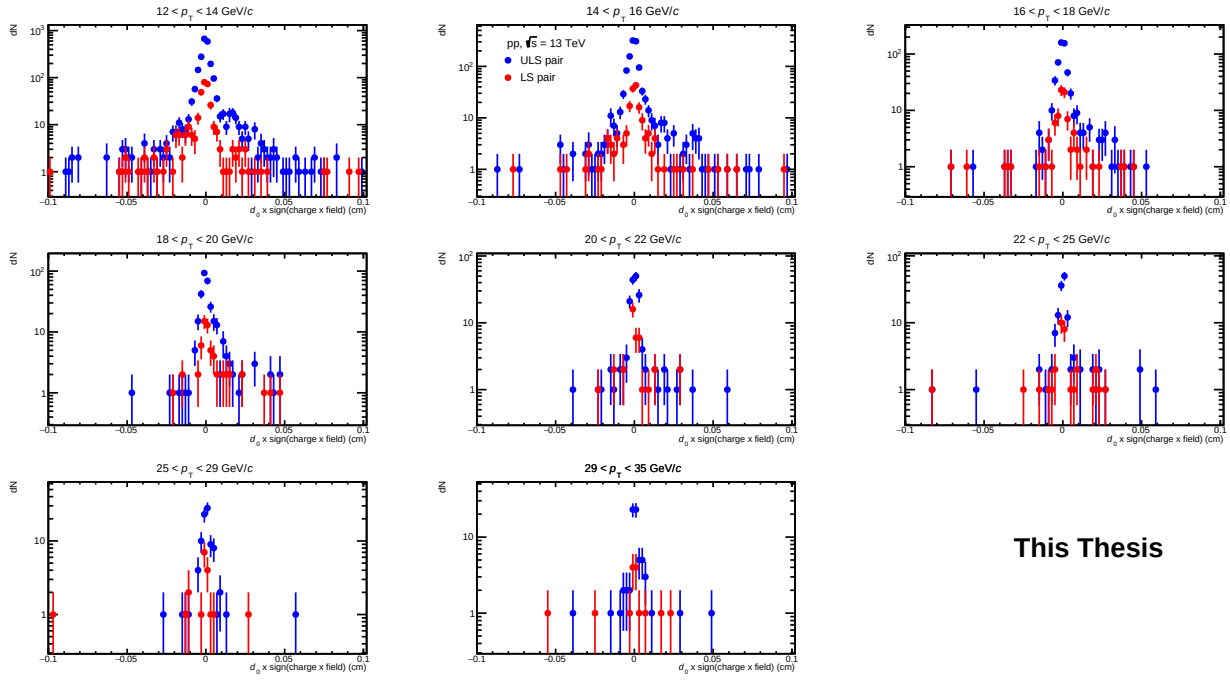

(c) EG1 trigger

Figure A.3: The d_0 distribution of the ULS electron pairs (blue) and LS electron pairs (red) within the invariant mass selection in respective p_{T} bins of MB, EG2 and EG1 triggered trigger events.

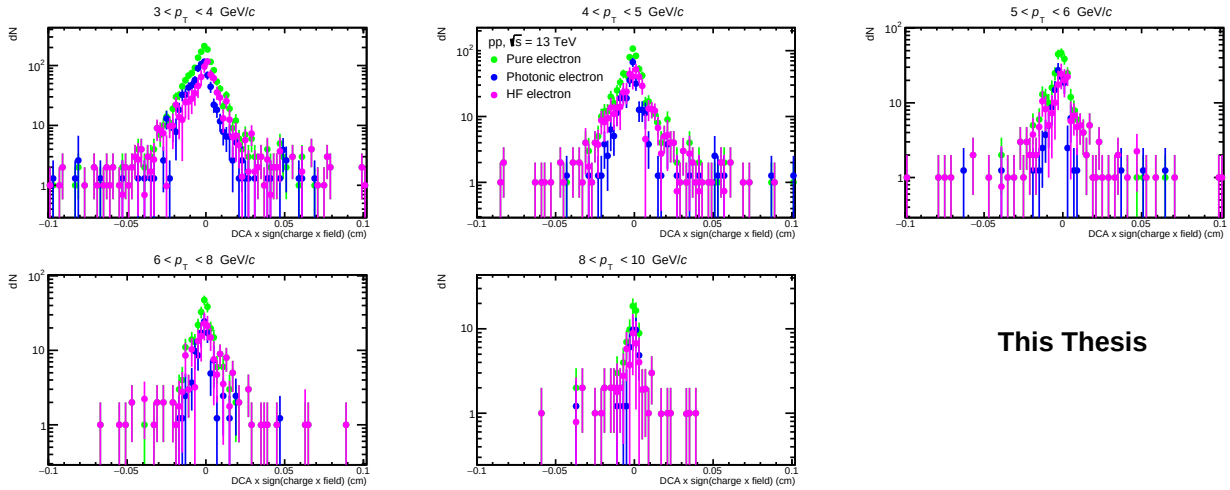

(a) MB trigger

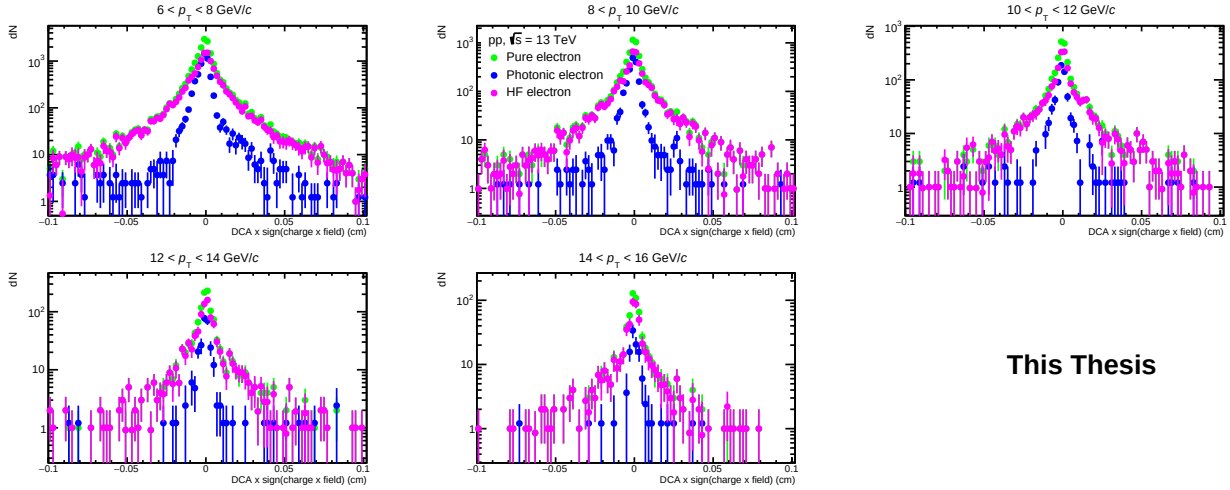

(b) EG2 trigger

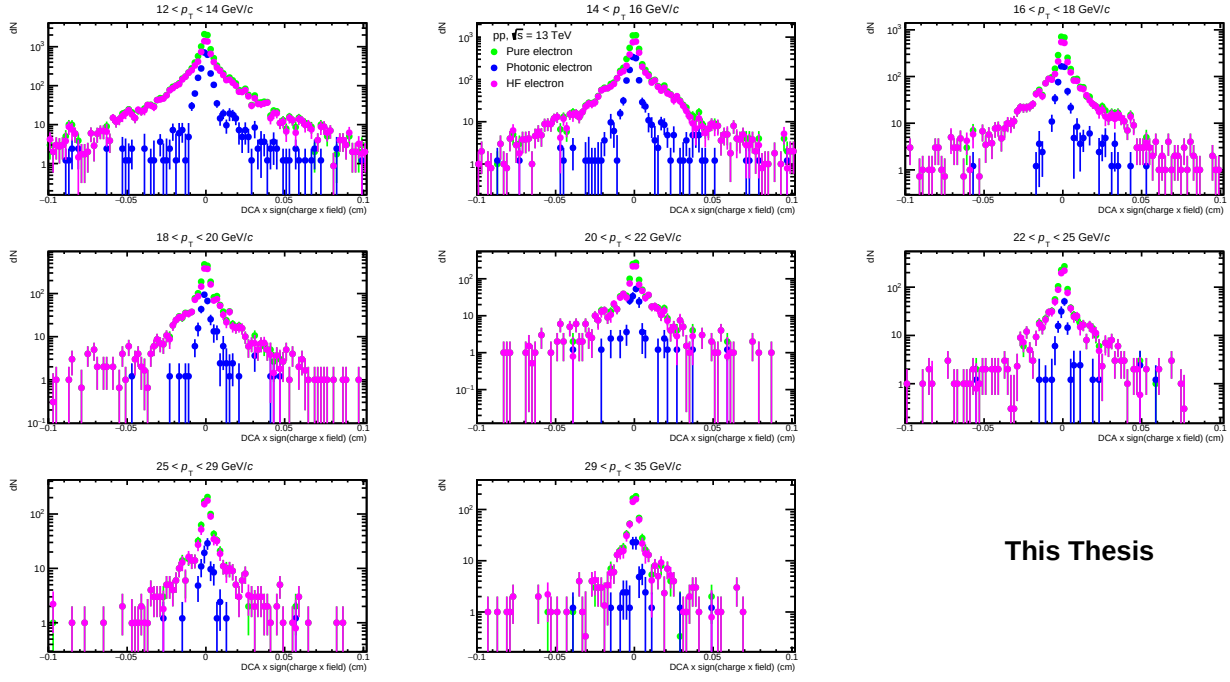

(c) EG1 trigger

Figure A.4: The d_0 distribution of pure electrons (green), photonic electrons (blue) and heavy-flavour decay electrons (magenta) in respective p_{T} bins of MB, EG2 and EG1 triggered trigger events..

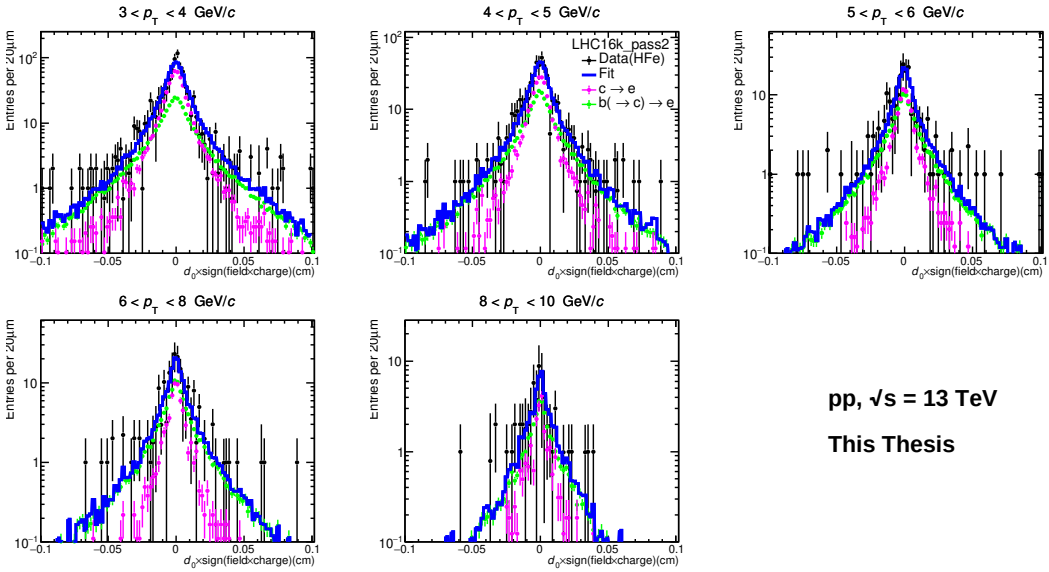

(a) MB trigger

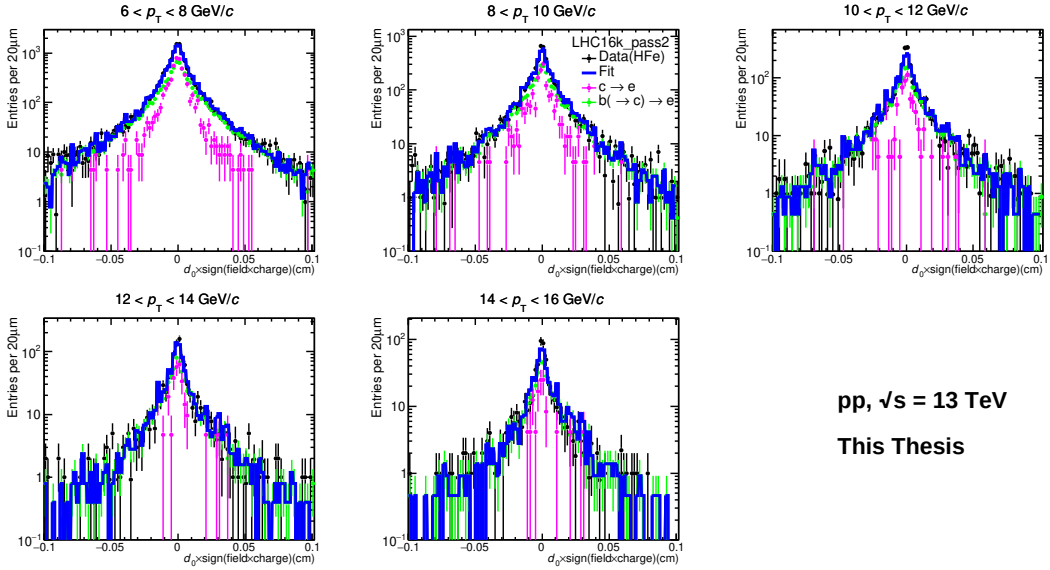

(b) EG2 trigger

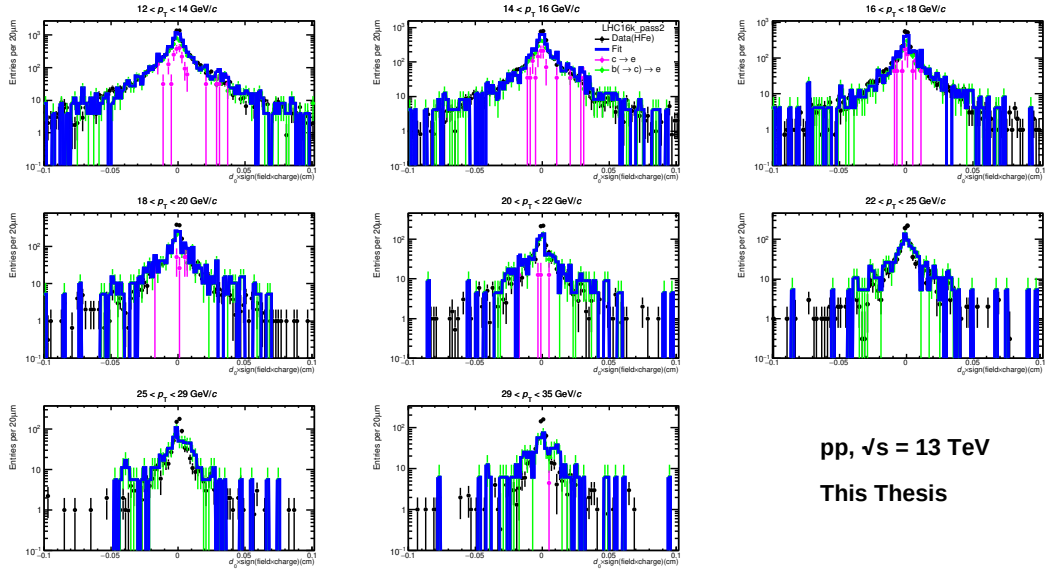

(c) EG1 trigger

Figure A.5: The HFe DCA distribution (black) fitted with charm(magenta) and beauty-decay electron (green) template with weighted log-likelihood fit option in respective p_{T} bins of EG1 trigger events.

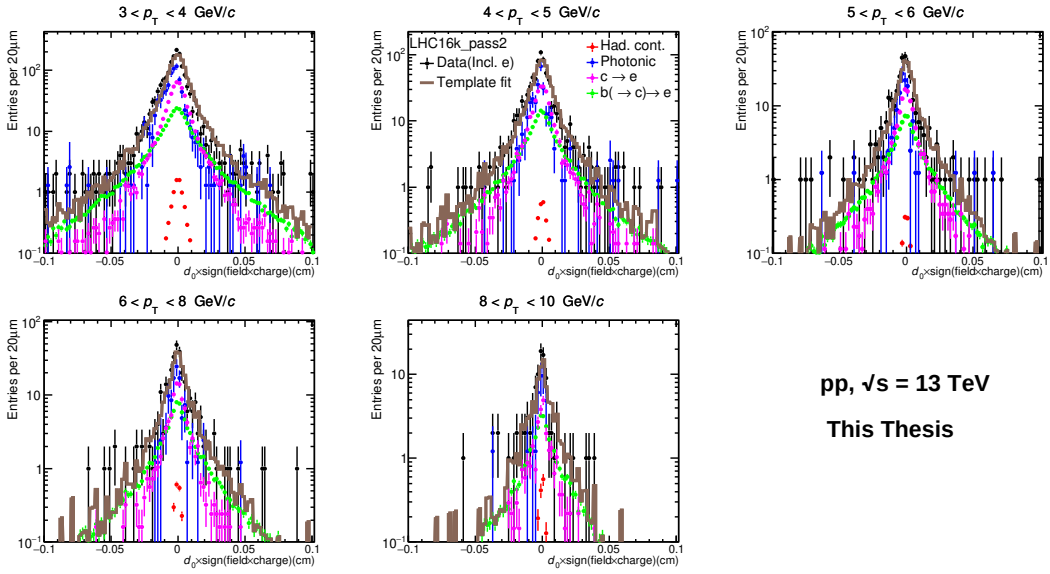

(a) MB trigger

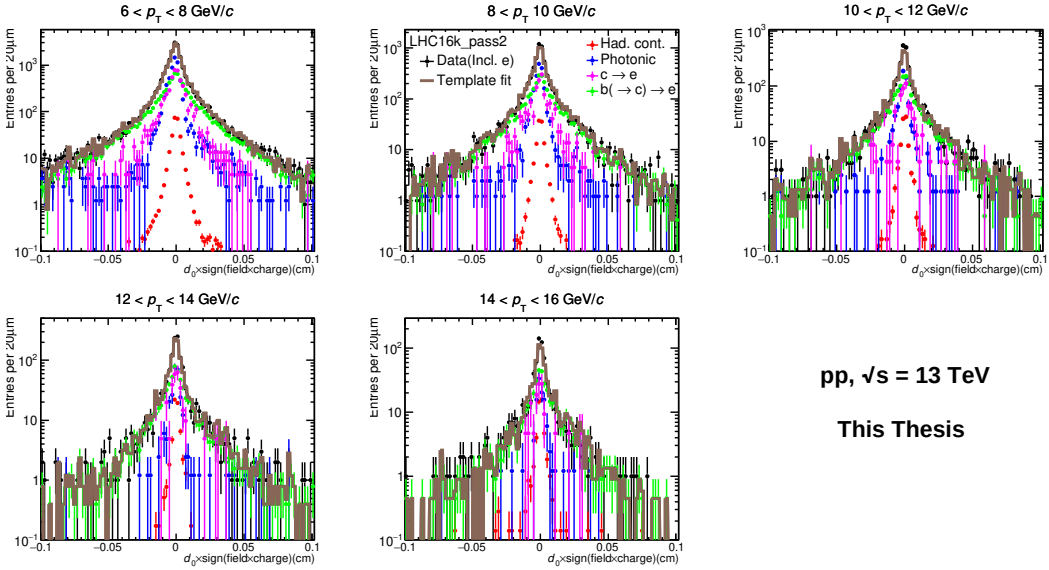

(b) EG2 trigger

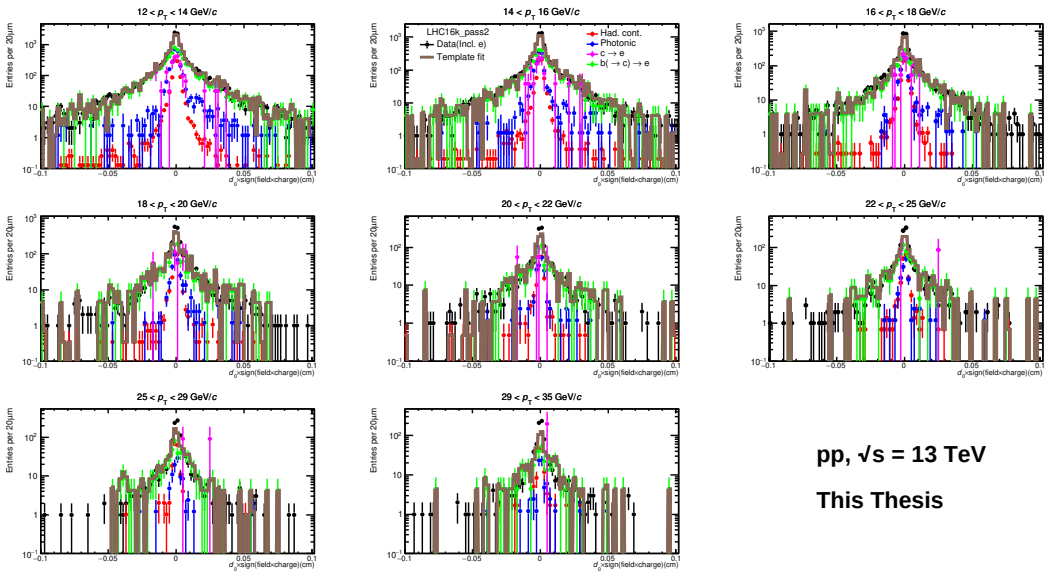

(c) EG1 trigger

Figure A.6: The inclusive electron DCA distribution (black) fitted with hadronic (red), photonic electron (blue), charm (magenta) and beauty-decay electron (green) template with log-likelihood fit option in respective p_{T} bins of MB trigger events.

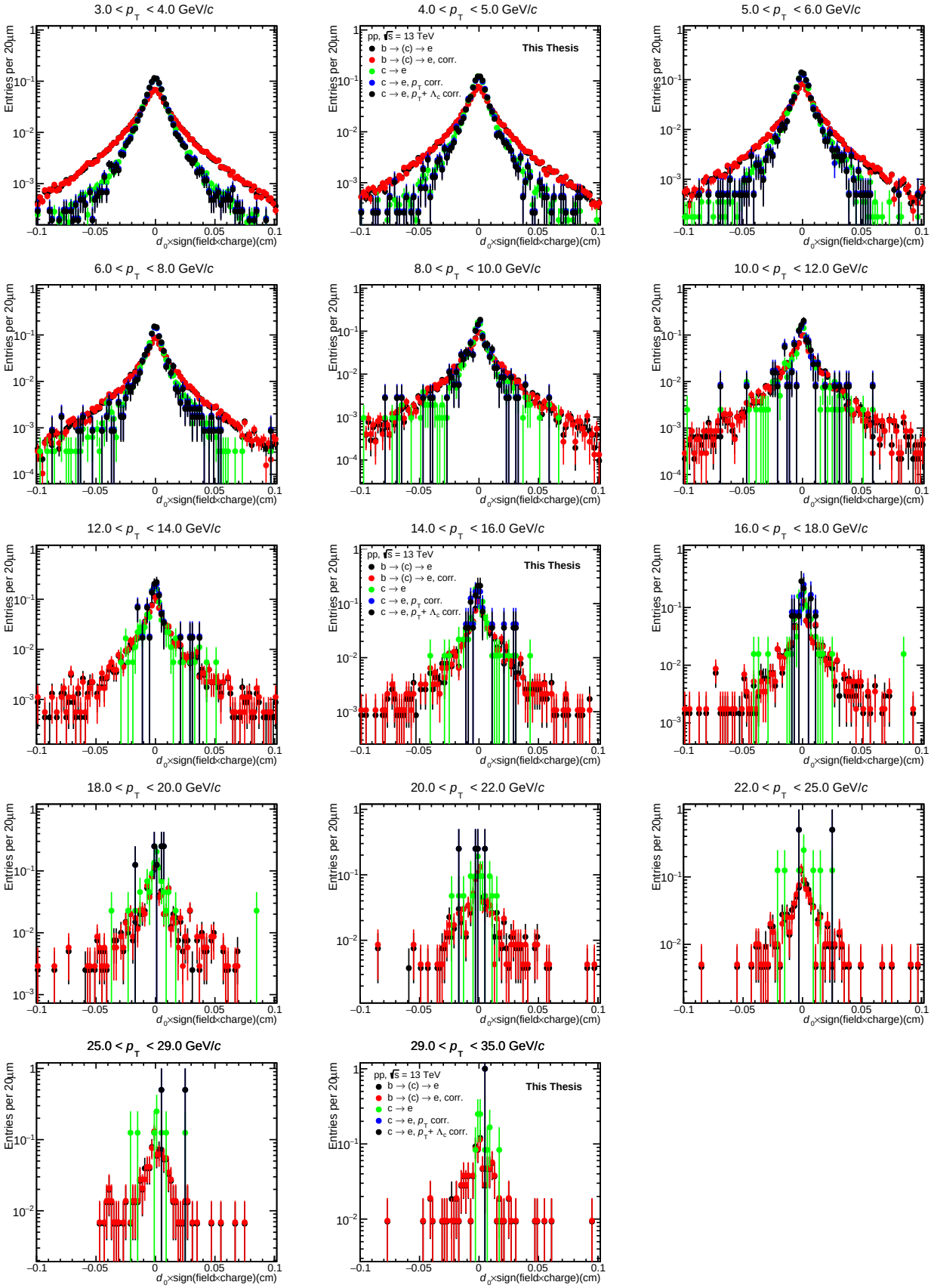

Figure A.7: The charm and beauty-decay electron templates with and without corrections.

Bibliography

[1] E. V. Shuryak, Phys. Lett. B **78**, 150 (1978).

[2] E. V. Shuryak, Phys. Rept. **61**, 71 (1980).

[3] K. A. Olive, The Quark - hadron transition in cosmology and astrophysics, Vol. 251 (1991) pp. 1194–1199.

[4] A. Aduszkiewicz et al. (NA61/SHINE), Eur. Phys. J. C **77**, 671 (2017), arXiv:1705.02467 [nucl-ex] .

[5] U. W. Heinz and M. Jacob, (2000), arXiv:nucl-th/0002042 .

[6] K. Adcox et al. (PHENIX), Nucl. Phys. A **757**, 184 (2005), arXiv:nucl-ex/0410003 .

[7] I. Arsene et al. (BRAHMS), Nucl. Phys. A **757**, 1 (2005), arXiv:nucl-ex/0410020 .

[8] B. B. Back et al. (PHOBOS), Nucl. Phys. A **757**, 28 (2005), arXiv:nucl-ex/0410022 .

[9] J. Adams et al. (STAR), Nucl. Phys. A **757**, 102 (2005), arXiv:nucl-ex/0501009 .

[10] X. Luo, Nucl. Phys. A **956**, 75 (2016), arXiv:1512.09215 [nucl-ex] .

[11] V. Toneev, PoS **CPOD07**, 057 (2007), arXiv:0709.1459 [nucl-ex] .

[12] G. Trubnikov, A. Butenko, V. Kekelidze, H. Khodzhibagiyan, S. Kostromin, V. Matveev, I. Meshkov, A. Sidorin, and A. Sorin, in 7th International Particle Accelerator Conference (2016) p. WEZA02.

[13] J. M. Heuser (CBM), EPJ Web Conf. **13**, 03001 (2011).

[14] S. Chattopadhyay, Nucl. Phys. A **931**, 267 (2014).

[15] W. Busza, K. Rajagopal, and W. van der Schee, Ann. Rev. Nucl. Part. Sci. **68**, 339 (2018), arXiv:1802.04801 [hep-ph] .

[16] V. Khachatryan et al. (CMS), JHEP **09**, 091 (2010), arXiv:1009.4122 [hep-ex] .

[17] V. Khachatryan et al. (CMS), Phys. Lett. B **765**, 193 (2017), arXiv:1606.06198 [nucl-ex] .

[18] J. Adam et al. (ALICE), Nature Phys. **13**, 535 (2017), arXiv:1606.07424 [nucl-ex] .

[19] S. Acharya et al. (ALICE), JHEP **08**, 006 (2023), arXiv:2303.13349 [nucl-ex] .

[20] X.-N. Wang and M. Gyulassy, Phys. Rev. D **44**, 3501 (1991).

[21] M. Bleicher et al., J. Phys. G **25**, 1859 (1999), arXiv:hep-ph/9909407 .

[22] V. K. Singh, D. K. Mishra, and Z. Ahammed, Phys. Rev. C **101**, 014903 (2020), arXiv:1907.02850 [hep-ph] .

[23] V. K. Singh, Mishra, and Z. Ahammed, Eur. Phys. J. A **56**, 230 (2020), arXiv:2002.10934 [nucl-th] .

[24] V. K. Singh (ALICE), "Measurement of electrons from beauty-hadron decays in pp collisions at $\sqrt{s} = 13$ TeV using TPC+EMCal," (2022).

[25] J. Adam et al. (ALICE), Phys. Lett. B **754**, 81 (2016), arXiv:1509.07491 [nucl-ex] .

[26] J. Adam et al. (ALICE), JHEP **07**, 052 (2017), arXiv:1609.03898 [nucl-ex] .

[27] S. Acharya et al. (ALICE), Phys. Rev. C **108**, 034906 (2023), arXiv:2211.13985 [nucl-ex] .

[28] "Wikimedia Commons: Standard Model of Elementary Particles," (2019).

[29] P. Gagnon (Quantum Diaries), "The Standard Model: a beautiful but flawed theory," (2014).

[30] Y. Nambu, Phys. Rev. Lett. **4**, 380 (1960).

[31] O. W. Greenberg, Phys. Rev. Lett. **13**, 598 (1964).

[32] S. Chatrchyan et al. (CMS), Phys. Lett. B **716**, 30 (2012), arXiv:1207.7235 [hep-ex] .

[33] G. Aad et al. (ATLAS), Phys. Lett. B **716**, 1 (2012), arXiv:1207.7214 [hep-ex] .

[34] G. Aad et al. (ATLAS), Phys. Rev. Lett. **131**, 251802 (2023), arXiv:2308.04775 [hep-ex] .

[35] M. E. Peskin, "Beyond the standard model," (1997), arXiv:hep-ph/9705479 .

[36] J. D. Lykken, "Beyond the Standard Model," (2010), arXiv:1005.1676 [hep-ph] .

[37] A. Pomarol, "Beyond the Standard Model," (2012), arXiv:1202.1391 [hep-ph] .

[38] G. Aad et al. (ATLAS), (2023), arXiv:2309.12986 [hep-ex] .

[39] H. D. Politzer, Phys. Rev. Lett. **30**, 1346 (1973).

[40] D. J. Gross and F. Wilczek, Phys. Rev. D **8**, 3633 (1973).

[41] E. Eichten, K. Gottfried, T. Kinoshita, J. B. Kogut, K. D. Lane, and T.-M. Yan, Phys. Rev. Lett. **34**, 369 (1975), [Erratum: Phys.Rev.Lett. 36, 1276 (1976)].

[42] F. Halzen and A. D. Martin, Quarks & Leptons: An introductory course in modern particle physics (John Wiley & Sons, 1984).

[43] M. E. Peskin and D. V. Schroeder, An Introduction to quantum field theory (Addison-Wesley, Reading, USA, 1995).

[44] M. Tanabashi et al. (Particle Data Group), Phys. Rev. D **98**, 030001 (2018).

[45] D. Cebra and STAR Collaboration, in APS Division of Nuclear Physics Meeting Abstracts, APS Meeting Abstracts, Vol. 2014 (2014) p. FJ.001.

[46] U. Heinz et al., (2015), arXiv:1501.06477 [nucl-th] .

[47] M. A. Stephanov, Prog. Theor. Phys. Suppl. **153**, 139 (2004), arXiv:hep-ph/0402115 .

[48] P. de Forcrand, PoS **LAT2009**, 010 (2009), arXiv:1005.0539 [hep-lat] .

[49] M. A. Stephanov, Phys. Rev. Lett. **102**, 032301 (2009), arXiv:0809.3450 [hep-ph] .

[50] C. Athanasiou, K. Rajagopal, and M. Stephanov, Phys. Rev. D **82**, 074008 (2010), arXiv:1006.4636 [hep-ph] .

[51] X. Luo (STAR), PoS **CPOD2014**, 019 (2015), arXiv:1503.02558 [nucl-ex] .

[52] M. L. Miller, K. Reygers, S. J. Sanders, and P. Steinberg, Ann. Rev. Nucl. Part. Sci. **57**, 205 (2007), arXiv:nucl-ex/0701025 .

[53] C. Sen, "Sketch of time evolution of an ultra-relativistic heavy-ion collision relativistic heavy-ion collisions," (2014).

[54] J. D. Bjorken, Phys. Rev. D **27**, 140 (1983).

[55] E. Iancu, A. Leonidov, and L. D. McLerran, arXiv reportNumber =:hep-ph/0011241 .

[56] J. W. Harris and B. Muller, Ann. Rev. Nucl. Part. Sci. **46**, 71 (1996), arXiv:hep-ph/9602235 .

[57] J. Adam et al. (ALICE), Phys. Rev. C **93**, 024917 (2016), arXiv:1506.08951 [nucl-ex] .

[58] Z. Fodor and S. D. Katz, JHEP **04**, 050 (2004), arXiv:hep-lat/0402006 .

[59] F. D. Steffen and M. H. Thoma, Phys. Lett. B **510**, 98 (2001), [Erratum: Phys.Lett.B 660, 604–606 (2008)], arXiv:hep-ph/0103044 .

[60] T. Peitzmann and M. H. Thoma, Phys. Rept. **364**, 175 (2002), arXiv:hep-ph/0111114 .

[61] J. Adam et al. (ALICE), Phys. Lett. B **754**, 235 (2016), arXiv:1509.07324 [nucl-ex] .

[62] A. Adare et al. (PHENIX), Phys. Rev. C **91**, 064904 (2015), arXiv:1405.3940 [nucl-ex] .

[63] R. Puri and Others, Advances in Nuclear Physics, Springer Proceedings in Physics (Springer, Singapore, 2019).

[64] S. Voloshin and Y. Zhang, Z. Phys. C **70**, 665 (1996), arXiv:hep-ph/9407282 .

[65] P. Foka and M. A. Janik, Rev. Phys. **1**, 154 (2016), arXiv:1702.07233 [hep-ex] .

[66] K. Aamodt et al. (ALICE), Phys. Rev. Lett. **105**, 252302 (2010), arXiv:1011.3914 [nucl-ex] .

[67] S. Acharya et al. (ALICE), Phys. Rev. Lett. **126**, 162001 (2021), arXiv:2005.11130 [nucl-ex] .

[68] R. Averbeck, Prog. Part. Nucl. Phys. **70**, 159 (2013), arXiv:1505.03828 [nucl-ex] .

[69] C. Loizides, J. Kamin, and D. d'Enterria, Phys. Rev. C **97**, 054910 (2018), [Erratum: Phys.Rev.C 99, 019901 (2019)], arXiv:1710.07098 [nucl-ex] .

[70] D. d'Enterria and C. Loizides, Ann. Rev. Nucl. Part. Sci. **71**, 315 (2021), arXiv:2011.14909 [hep-ph] .

[71] B. I. Abelev et al. (STAR), Phys. Rev. Lett. **98**, 192301 (2007), [Erratum: Phys.Rev.Lett. 106, 159902 (2011)], arXiv:nucl-ex/0607012 .

[72] D. d'Enterria, Landolt-Bornstein **23**, 471 (2010), arXiv:0902.2011 [nucl-ex] .

[73] J. Adams et al. (STAR), Phys. Rev. Lett. **91**, 072304 (2003), arXiv:nucl-ex/0306024 .

[74] K. Aamodt et al. (ALICE), Phys. Rev. Lett. **108**, 092301 (2012), arXiv:1110.0121 [nucl-ex] .

[75] T. Matsui and H. Satz, Phys. Lett. B **178**, 416 (1986).

[76] B. Alessandro et al. (NA50), Eur. Phys. J. C **39**, 335 (2005), arXiv:hep-ex/0412036 .

[77] A. Adare et al. (PHENIX), Phys. Rev. Lett. **98**, 232301 (2007), arXiv:nucl-ex/0611020 .

[78] B. Abelev et al. (ALICE), Phys. Rev. Lett. **109**, 072301 (2012), arXiv:1202.1383 [hep-ex] .

[79] P. Braun-Munzinger and J. Stachel, Phys. Lett. B **490**, 196 (2000), arXiv:nucl-th/0007059 .

[80] R. L. Thews, M. Schroedter, and J. Rafelski, Phys. Rev. C **63**, 054905 (2001), arXiv:hep-ph/0007323 .

[81] X. Du and R. Rapp, Nucl. Phys. A **943**, 147 (2015), arXiv:1504.00670 [hep-ph] .

[82] P. Koch, B. Muller, and J. Rafelski, Phys. Rept. **142**, 167 (1986).

[83] J. Rafelski and B. Muller, Phys. Rev. Lett. **48**, 1066 (1982), [Erratum: Phys.Rev.Lett. 56, 2334 (1986)].

[84] H. Heiselberg and A. D. Jackson, Phys. Rev. C **63**, 064904 (2001), arXiv:nucl-th/0006021 .

[85] S. Jeon and V. Koch, Phys. Rev. Lett. **85**, 2076 (2000), arXiv:hep-ph/0003168 .

[86] M. Asakawa, U. Heinz, and B. Müller, Phys. Rev. Lett. **85**, 2072 (2000).

[87] M. Cacciari, M. Greco, and P. Nason, JHEP **05**, 10.1088/1126-6708/1998/05/007, arXiv:hep-ph/9803400 .

[88] M. Cacciari, S. Frixione, N. Houdeau, M. L. Mangano, P. Nason, and G. Ridolfi, JHEP **10**, 137 (2012), arXiv:1205.6344 [hep-ph] .

[89] P. Bolzoni and G. Kramer, Nucl. Phys. B **872**, 253 (2013), [Erratum: Nucl.Phys.B 876, 334–337 (2013)], arXiv:1212.4356 [hep-ph] .

[90] B. Guiot and A. van Hameren, Phys. Rev. D **104**, 094038 (2021), arXiv:2108.06419 [hep-ph] .

[91] R. Maciula and A. Szczurek, Phys. Rev. D **87**, 094022 (2013), arXiv:1301.3033 [hep-ph] .

[92] B. B. Abelev et al. (ALICE), Phys. Lett. B **738**, 97 (2014), arXiv:1405.4144 [nucl-ex] .

[93] S. Acharya et al. (ALICE), JHEP **05**, 220 (2021), arXiv:2102.13601 [nucl-ex] .

[94] S. Acharya et al. (ALICE), (2024), arXiv:2402.16417 [hep-ex] .

[95] B. Abelev et al. (ALICE), Phys. Lett. B **721**, 13 (2013), [Erratum: Phys.Lett.B 763, 507–509 (2016)], arXiv:1208.1902 [hep-ex] .

[96] J. Park (ALICE), "Measurement of electrons from beauty-hadron decays in pp collisions at $\sqrt{s} = 13$ TeV using TPC+TOF," (2022).

[97] S. Jeon and V. Koch, Phys. Rev. Lett. **83**, 5435 (1999).

[98] J. Adams et al. (STAR), Phys. Rev. C **68**, 044905 (2003), arXiv:nucl-ex/0307007 .

[99] B. I. Abelev et al. (STAR), Phys. Rev. C **79**, 024906 (2009), arXiv:0807.3269 [nucl-ex] .

[100] D. Adamova et al. (CERES), Nucl. Phys. A **727**, 97 (2003), arXiv:nucl-ex/0305002 .

[101] C. Alt et al. (NA49), Phys. Rev. C **70**, 064903 (2004), arXiv:nucl-ex/0406013 .

[102] K. Adcox et al. (PHENIX Collaboration), Phys. Rev. Lett. **89**, 082301 (2002).

[103] K. Adcox et al. (PHENIX), Phys. Rev. C **66**, 024901 (2002), arXiv:nucl-ex/0203015 .

[104] B. Abelev et al. (ALICE), Phys. Rev. Lett. **110**, 152301 (2013), arXiv:1207.6068 [nucl-ex] .

[105] E. V. Shuryak and M. A. Stephanov, Phys. Rev. C **63**, 064903 (2001).

[106] M. A. Aziz and S. Gavin, Phys. Rev. C **70**, 034905 (2004), arXiv:nucl-th/0404058 .

[107] Y. Hatta and M. A. Stephanov, Phys. Rev. Lett. **91**, 102003 (2003), [Erratum: Phys.Rev.Lett. 91, 129901 (2003)], arXiv:hep-ph/0302002 .

[108] D. K. Mishra, P. K. Netrakanti, and P. Garg, Phys. Rev. C **95**, 054905 (2017).

[109] S. Jeon and V. Koch, "Event-by-event fluctuations," (2003), arXiv:hep-ph/0304012 [hep-ph] .

[110] C. Pruneau, S. Gavin, and S. Voloshin, Phys. Rev. C **66**, 044904 (2002), arXiv:nucl-ex/0204011 .

[111] M. Bleicher, S. Jeon, and V. Koch, Phys. Rev. C **62**, 061902 (2000), arXiv:hep-ph/0006201 .

[112] F. Karsch and K. Redlich, Phys. Lett. B **695**, 136 (2011), arXiv:1007.2581 [hep-ph] .

[113] P. Garg, D. K. Mishra, P. K. Netrakanti, B. Mohanty, A. K. Mohanty, B. K. Singh, and N. Xu, Phys. Lett. B **726**, 691 (2013), arXiv:1304.7133 [nucl-ex] .

[114] V. V. Begun, M. I. Gorenstein, M. Hauer, V. P. Konchakovski, and O. S. Zozulya, Phys. Rev. C **74**, 044903 (2006), arXiv:nucl-th/0606036 .

[115] D. K. Mishra, P. Garg, P. K. Netrakanti, and A. K. Mohanty, Phys. Rev. C **94**, 014905 (2016), arXiv:1607.01875 [hep-ph] .

[116] L. V. Bravina et al., Phys. Lett. B **434**, 379 (1998), arXiv:nucl-th/9804008 .

[117] S. A. Bass et al., Phys. Rev. Lett. **81**, 4092 (1998), arXiv:nucl-th/9711032 .

[118] S. Soff, S. A. Bass, M. Bleicher, L. Bravina, M. Gorenstein, E. Zabrodin, H. Stoecker, and W. Greiner, Phys. Lett. B **471**, 89 (1999), arXiv:nucl-th/9907026 .

[119] C. Spieles, L. Gerland, N. Hammon, M. Bleicher, S. A. Bass, H. Stoecker, W. Greiner, C. Lourenco, and R. Vogt, Eur. Phys. J. C **5**, 349 (1998), arXiv:hep-ph/9706525 .

[120] M. Bleicher, M. Belkacem, C. Ernst, H. Weber, L. Gerland, C. Spieles, S. A. Bass, H. Stoecker, and W. Greiner, Phys. Lett. B **435**, 9 (1998), arXiv:hep-ph/9803345 .

[121] J. Xu, S. Yu, F. Liu, and X. Luo, Phys. Rev. C **94**, 024901 (2016), arXiv:1606.03900 [nucl-ex] .

[122] C. Zhou, J. Xu, X. Luo, and F. Liu, Phys. Rev. C **96**, 014909 (2017), arXiv:1703.09114 [nucl-ex] .

[123] P. K. Netrakanti, X. F. Luo, D. K. Mishra, B. Mohanty, A. Mohanty, and N. Xu, Nucl. Phys. A **947**, 248 (2016), arXiv:1405.4617 [hep-ph] .

[124] G. D. Westfall, Phys. Rev. C **92**, 024902 (2015), arXiv:1412.5988 [nucl-th] .

[125] S. He and X. Luo, Phys. Lett. B **774**, 623 (2017), arXiv:1704.00423 [nucl-ex] .

[126] E. Mobs, The CERN accelerator complex in 2019. Complexe des accélérateurs du CERN en 2019, CERN-GRAPHICS-2019-002 (CERN, Geneva, 2019).

[127] The ATLAS Experiment at LHC, https://home.web.cern.ch/science/experiments/atlas.

[128] The CMS Experiment at LHC, https://home.web.cern.ch/science/experiments/cms.

[129] The ALICE Experiment at LHC, https://home.web.cern.ch/science/experiments/alice.

[130] The LHCb Experiment at LHC, https://home.web.cern.ch/science/experiments/lhcb.

[131] A. Tauro, ALICE Schematics, ALICE-PHO-SKE-2017-001 (CERN, Geneva, 2017).

[132] K. Aamodt et al. (ALICE), JINST **3**, S08002 (2008).

[133] S. Acharya et al. (ALICE), JINST **18**, P08007 (2023), arXiv:2209.04216 [physics.ins-det] .

[134] ALICE Inner Tracking System (ITS): Technical Design Report, Technical design report. ALICE (CERN, Geneva, 1999).

[135] ALICE time projection chamber: Technical Design Report, Technical design report. ALICE (CERN, Geneva, 2000).

[136] ALICE Time-Of-Flight system (TOF): Technical Design Report, Technical design report. ALICE (CERN, Geneva, 2000).

[137] F. Piuz, W. Klempt, L. Leistam, J. De Groot, and J. Schükraft (ALICE), ALICE high-momentum particle identification: Technical Design Report, Technical design report. ALICE (CERN, Geneva, 1998).

[138] P. Cortese (ALICE), ALICE transition-radiation detector: Technical Design Report, Technical design report. ALICE (CERN, Geneva, 2001).

[139] V. I. Man'ko, W. Klempt, L. Leistam, J. De Groot, and J. Schükraft (ALICE), ALICE Photon Spectrometer (PHOS): Technical Design Report, Technical design report. ALICE (CERN, Geneva, 1999).

[140] ALICE Electromagnetic Calorimeter Technical Design Report, Technical design report. ALICE (CERN, Geneva, 2008).

[141] M. Gallio, W. Klempt, L. Leistam, J. De Groot, and J. Schükraft (ALICE), ALICE Zero-Degree Calorimeter (ZDC): Technical Design Report, Technical design report. ALICE (CERN, Geneva, 1999).

[142] ALICE Photon Multiplicity Detector (PMD): Technical Design Report, Technical design report. ALICE (CERN, Geneva, 1999).

[143] ALICE forward detectors: FMD, TO and VO : Technical Design Report, Technical design report. ALICE (CERN, Geneva, 2004).

[144] R. M. Brown (CMS), Nucl. Instrum. Meth. A **572**, 26 (2007).

[145] P. Kuijer (ALICE), Nucl. Instrum. Meth. A **530**, 28 (2004).

[146] E. Botta (ALICE), "Particle identification performance at ALICE. Particle identification performance at ALICE," (2017), 6 pages, 5 figures, Proceeding of the Fifth Annual Conference on Large Hadron Collider Physics, May 15-20, 2017, Shanghai, Cina, arXiv:1709.00288 .

[147] R. Fruhwirth, Nucl. Instrum. Meth. A **262**, 444 (1987).

[148] B. B. Abelev et al. (ALICE), Int. J. Mod. Phys. A **29**, 1430044 (2014), arXiv:1402.4476 [nucl-ex] .

[149] E. F. Gauger, "Production of beauty-hadron decay electrons in Pb-Pb collisions at $\sqrt{s_{\rm NN}} = 5.02$ TeV in ALICE," (2021), presented 21 Apr 2021.

[150] M. Arslandok, E. Hellbär, M. Ivanov, R. H. Münzer, and J. Wiechula, Particles **5**, 84 (2022), arXiv:2203.10325 [physics.ins-det] .

[151] W. Blum, L. Rolandi, and W. Riegler, Particle detection with drift chambers, Particle Acceleration and Detection (2008).

[152] First results of the ALICE detector performance at 13 TeV, ALICE Public report. ALICE (CERN, Geneva, 2015).

[153] J. Allen and Others, "ALICE DCal: An Addendum to the EMCal Technical Design Report Di-Jet and Hadron-Jet correlation measurements in ALICE," (2010).

[154] F. Alessandra, in The ALICE experiment and its Electromagnetic Calorimeter EMCAL (2011 BCVSPIN Advanced Study Institute in Particle Physics and Cosmology, Hue, Vietnam, 2011).

[155] G. Conesa Balbastre, "Study of the strong interaction with high-energy photons at the LHC: Experience with the ALICE-EMCal detector operation and measurements," (2019), published: 02 Oct 2019.

[156] T. C. Awes, F. E. Obenshain, F. Plasil, S. Saini, S. P. Sorensen, and G. R. Young, Nucl. Instrum. Meth. A **311**, 130 (1992).

[157] U. Abeysekara et al. (ALICE EMCal), (2010), arXiv:1008.0413 [physics.ins-det] .

[158] C. W. Fabjan et al. (ALICE), J. Phys. G **32**, 1295 (2006).

[159] S. Acharya, Multiparticle production in proton-proton collisions at the LHC energies, Ph.D. thesis, Homi Bhabha National Institute (HBNI) (2021), presented 12 Oct 2021.

[160] O. Bourrion, N. Arbor, G. Conesa-Balbastre, C. Furget, R. Guernane, and G. Marcotte (ALICE EMCal), JINST **8**, C01013 (2013), arXiv:1210.8078 [physics.ins-det] .

[161] S. Acharya et al. (ALICE), Eur. Phys. J. C **77**, 339 (2017), arXiv:1702.00917 [hep-ex] .

[162] M. Krivda, D. Alexandre, L. S. Barnby, D. Evans, P. G. Jones, A. Jusko, R. Lietava, J. Pospíšil, and O. V. Baillie (ALICE), JINST **11**, C03051 (2016).

[163] R. Alfaro, E. Cuautle, and G. Paic (ALICE), Rejection of beam gas interactions in pp collisions and timing requirements, Internal Note. ALICE (CERN, Geneva, 2004) submitted on 24 Aug 2004.

[164] A. Andronic et al., Eur. Phys. J. C **76**, 107 (2016), arXiv:1506.03981 [nucl-ex] .

[165] F.-M. Liu and S.-X. Liu, Phys. Rev. C **89**, 034906 (2014), arXiv:1212.6587 [nucl-th] .

[166] R. Baier, D. Schiff, and B. G. Zakharov, Ann. Rev. Nucl. Part. Sci. **50**, 37 (2000), arXiv:hep-ph/0002198 .

[167] Y. L. Dokshitzer and D. E. Kharzeev, Phys. Lett. B **519**, 199 (2001), arXiv:hep-ph/0106202 .

[168] N. Armesto, C. A. Salgado, and U. A. Wiedemann, Phys. Rev. D **69**, 114003 (2004), arXiv:hep-ph/0312106 .

[169] S. Wicks, W. Horowitz, M. Djordjevic, and M. Gyulassy, Nucl. Phys. A **783**, 493 (2007), arXiv:nucl-th/0701063 .

[170] B.-W. Zhang, E. Wang, and X.-N. Wang, Phys. Rev. Lett. **93**, 072301 (2004), arXiv:nucl-th/0309040 .

[171] S. Cao et al., Phys. Rev. C **99**, 054907 (2019), arXiv:1809.07894 [nucl-th] .

[172] M. Cacciari, S. Frixione, and P. Nason, JHEP **03**, 006 (2001), arXiv:hep-ph/0102134 .

[173] J. Adam et al. (ALICE), Phys. Lett. B **771**, 467 (2017), arXiv:1609.07104 [nucl-ex] .

[174] "ALICE EMCal analysis and correction framework," (2018).

[175] "ALICE DPG Improver Task ALICE TWiki," (2019).

[176] "ALICE DPG Run Lists," (2018).

[177] "ALICE DPG Pileup in Run-2 Data Sample," (2017).

[178] S. Acharya et al. (ALICE), JHEP **08**, 006 (2023), arXiv:2303.13349 [nucl-ex] .

[179] M. Völkl, Electrons from beauty-hadron decays in central Pb-Pb collisions at $\sqrt{S_{NN}} = 2.76$ TeV, Ph.D. thesis, U. Heidelberg (main) (2016), presented 28 Oct 2016.

[180] S. Acharya et al. (ALICE), JHEP **10**, 061 (2018), arXiv:1805.04379 [nucl-ex] .

[181] S. Acharya et al. (ALICE), Phys. Lett. B **819**, 136437 (2021), arXiv:2011.06970 [nucl-ex] .

[182] S. Acharya et al. (ALICE), Phys. Rev. C **99**, 024906 (2019), arXiv:1807.11321 [nucl-ex] .

[183] A. M. Sirunyan et al. (CMS), Phys. Lett. B **813**, 136036 (2021), arXiv:2009.07065 [hep-ex] .

[184] S. Acharya et al. (ALICE), Phys. Rev. Lett. **128**, 012001 (2022), arXiv:2106.08278 [hep-ex] .

[185] S. Acharya et al. (ALICE), JHEP **12**, 086 (2023), arXiv:2308.04877 [hep-ex] .

[186] P. A. Zyla et al. (Particle Data Group), PTEP **2020**, 083C01 (2020).

[187] R. J. Barlow and C. Beeston, Comput. Phys. Commun. **77**, 219 (1993).

[188] E. Gauger and Others (ALICE), "Paper proposal: Beauty-decay electrons in pp and Pb-Pb at $\sqrt{S_{NN}} = 5.02$ TeV," (2020).

[189] ALICE 2016-2017-2018 luminosity determination for pp collisions at $\sqrt{s} = 13$ TeV, ALICE Publications (CERN, Geneva, 2021).

[190] R. Aaij et al. (LHCb), Phys. Rev. D **100**, 031102 (2019), arXiv:1902.06794 [hep-ex] .

[191] S. Acharya et al. (ALICE), Phys. Lett. B **804**, 135377 (2020), arXiv:1910.09110 [nucl-ex] .

[192] B. Abelev et al. (ALICE), Phys. Rev. D **86**, 112007 (2012), arXiv:1205.5423 [hep-ex] .

[193] B. B. Abelev et al. (ALICE), Phys. Rev. D **91**, 012001 (2015), arXiv:1405.4117 [nucl-ex] .

[194] A. F. A. R. e. a. Andronic, A., Eur. Phys. J. C **76**, 107 (2016).